Ozone in a Jack Pine Forest in the Athabasca Oil Sands Region

Xuanyi Zhang

A Thesis submitted to the Faculty of Graduate Studies

in Partial Fulfillment of the Requirements

for the Degree of Master of Science

Graduate program in Earth and Space Science

York University

Toronto, Ontario

October 2020

Abstract

The concentration of tropospheric ozone is modified by vertical mixing from the stratosphere, photochemical reactions, and surface deposition. Photochemical reaction is the primary source of ozone, with the ozone formation reaction depending on the concentration of precursors such as volatile organic compounds (VOCs) and nitrogen oxides (NO_x). Anthropogenic emissions from oil sand extraction increase VOC concentration relative to background conditions and may have an impact on ozone concentrations. Ozone precursors react with ultraviolet (UV) radiation, which leads to an increase of the tropospheric ozone mixing ratio. Determination of the causes of ozone formation and destruction in a region affected by anthropogenic emissions thus require careful study to determine their relative impacts. This study focusses on ozone concentration analysis within and above a Jack Pine forest canopy in Northern Alberta. The York Athabasca Jack Pine (YAJP) instrumented tower is located in a forest region surrounded by oil sand production facilities. It is 45 km north of Fort McMurry. Ozone concentration was measured above and within the forest canopy, as well as ultraviolet and photosynthetically active radiation (UV and PAR), and meteorological variables. A tethered-Balloon system, which measured the ozone profile from the ground up to 300 meters was installed in a clearing about 100 meters southeast of the tower location. These measurements are compared to the results of a 1D canopy model, and the GEM-MACH 3D model running at 2.5 km resolution, to identify the factors of ozone mixing ratio and to identify how anthropogenic emissions affect ozone concentration in the forest. The result show that pollution from surrounding oil facilities can enhance the ozone mixing ratio in

the forest, and the enhancement usually happens with high temperature and air stagnation. The measurement also found that ozone mixing ratio increased with height within the forest canopy. Wind speed is negatively correlated to the ozone mixing ratio. The low wind speed (less than 3 m/s) can enhance the ozone mixing ratio, due to ozone accumulation. The high wind speed (more than 3 m/s) can dilute the ozone to decrease the ozone mixing ratio.

Dedication

I would like to dedicate this thesis to the memory of my late grandmother.

Acknowledgement

Many people have made invaluable contributions to my master's thesis, both directly and indirectly. Foremost, I would like to express my deep gratitude to my advisor, Professor Mark Gordon, for the continuous support of my master's research and study. This thesis wouldn't finish without his enlightening guidance. This year, the COVID-19 pandemic changed our lives to work from home, but Professor Gordon still has done his best to help me edit, find data and provide me suggestions for my thesis.

I would also like to thank my thesis committees Professor Jim Whiteway, Professor Yongsheng Chen, and Professor Rob McLaren, for providing me advice on thesis correction based on their fields.

Thanks to Timothy Jiang for helping me with data collection; and to Sepehr Fathi for assisting me on GEM-MACH data extraction, thanks to Mohammad Koushafar and Stefan Miller for their support and kindness. It is a pleasure to meet these gorgeous people in the Air Pollution Lab.

Last and but not least, I would like to thank my parents and my friends for supporting me throughout my life.

Table of Content

List of Tables

List of Figures

1. Introduction

Oil sands are a tremendous resource in Canada (CAPP, 2018). The oil sands region covers an area of approximately 142,000 km^2 (Stringham, 2011). In 2017, approximately 63% of Canada's crude oil production was from oil sands (CAPP, 2018). Canada's largest oil sands deposit areas can be found in Alberta; they include the Athabasca Peace River and Cold Lake deposits (CAPP, 2018). The Alberta oil sands are comprised of 10-12% bitumen, 3-5% water and 75-80% inorganic material (CAPP, 2018). Oil recovery depends on surface mining and *in situ* drilling. Surface mining is for shallower oil sand extraction, and *in situ* extraction is for deeper extraction (Charpentier, Bergerson & MacLean, 2009). In Alberta, about 60% of heavy bitumen recovery depends on the *in situ* drilling extraction (Stringham, 2011). The increasing oil sands production accounts for one of the primary anthropogenic greenhouse gas emission sources and leads to the increased environmental concern for the nearby forest ecosystem (Li et al., 2017). For example, the increased VOC and NO mixing ratios from oil extraction lead to an increase of secondary pollutant ozone mixing ratio.

Ozone is a reactive oxidant gas, and about 90% of ozone can be found in the stratosphere (Seinfeld & Pandis, 2016). Stratospheric ozone can absorb UV light to reduce the amount of UV that gets to the ground. Because the ozone depletion happens in the stratosphere, more UV radiation gets through to the tropopause compared to no ozone depletion in the stratosphere. This causes an increase of UV radiation in the troposphere (Manning & Tiedemann, 1995). Ozone is a photochemical pollutant (Logan, 1985). High surface UV radiation contributes to high ozone mixing ratios, and previous studies found ozone in the troposphere can absorb UV radiation (R 1.1) but the ozone mixing ratio and UV radiation

in the Northern Hemisphere is usually higher than the Southern Hemisphere, which may lead to a positive feedback (Olltmans et al., 2006; Mckenzie, 2003; Logan, 1985). R 1.1 and R 1.2 represents how ozone is formed in the troposphere, where UV radiation is essential to react with chemicals such as NO_2 to form oxygen atoms, and then to combine with O_2 to form O_3.Therefore, UV analysis becomes important to analyze ozone mixing ratios associated with NO_X emissions from the surrounding crude oil producers. In addition, in the troposphere, UV radiation comes from aloft, which leads to oxygen atom formation increasing with altitude, and causes ozone mixing ratio to increase with height in the lower troposphere.

$$NO_2 \xrightarrow{h\nu} NO + O(^3p) \quad \lambda < 420nm, \tag{R 1.1}$$

$$O(^3P) + O_2 + M \longrightarrow O_3 + M, \tag{R 1.2}$$

$$O_3 + NO \rightarrow NO_2 + O_2, \tag{R 1.3}$$

In the troposphere, ozone not only affects climate, but it is also harmful to human health due to its strong oxidant property (Stathopoulou et al., 2008). From recent research, ozone pollution is responsible for 0.7 million deaths per year (Ainsworth, et al., 2012). High ozone mixing ratio can affect the forest ecosystem. It is toxic to plants, limits plants photosynthesis (Lamaud et al., 2002), reduces tree species biomass, and suppresses vegetation growth (Chappelka & Samuelson, 1998).

This study analyzes how oil sands extraction modifies the ozone mixing ratio in the surrounding forest. Thus, a boreal forest area was chosen which is surrounded by Syncrude, Suncor, Canadian Natural Source limited (CNRL) and some smaller facilities. The

processes of oil sands operations include surface mining to turn surface oil sands into crude oil, well injection to pump deeper bitumen onto the surface, extraction of bitumen from oil sands with the water-based process and the upgrade of bitumen into hydrocarbon streams (Natural Resource Canada, 2016). Each step of oil extraction can produce air pollutants. There are five major air pollutants directly produced by the oil extraction (Allison & Mandler, 2018; Aggarwal, 2018). These include carbon monoxide (CO), nitrogen oxides (NO_x, which includes NO and NO_2), sulfur oxides (SO_x), ammonia (NH_3), particulate matter (PM) and volatile organic compounds (VOCs). With wind direction variation, when the forest is downwind of the nearby oil facilities, the air pollutions emitted from these oil facilities are finally detected in the forest. In the troposphere, ozone mixing ratio is modified by vertical mixing from the stratosphere, photochemical reaction, and earth surface deposition (Lamaud et al., 2002). The photochemical reaction is the most important way to produce ozone in the lower troposphere. In Alberta, primary air pollutants, such as VOCs and NO_x, react with UV radiation to produce a high amount of ozone (see details in section 1.1), and the increased ozone mixing ratio will affect plant growth in the forest.

1.1 Chemistry of Tropospheric Ozone

Before the 20th century, scientists thought that most of the ozone in the troposphere was transferred from the stratosphere, and very little was from photochemical reactions (Newell, 1963). However, in 1978, Fishman and Crutzen suggested that the main reason for tropospheric ozone is photochemical reactions. Oil combustion and extraction discharge large amounts of NO_x and VOCs. In the troposphere, the photochemical reactions are indicated in R1.1 – R1.3, where M represents the third body, which is used to take excess

energy. In the troposphere, M can be bulk constituents of air, and M is mainly O_2 and N_2 (Holloway &Wayne, 2010 PP57-59).

In addition, VOCs are important for the photooxidation of NO in the troposphere (Finlayson-Pitts & Pitts, 1993). With VOCs, the reactions are (National Research Council, 1991)

$$RH + OH + O_2 \xrightarrow{M} RO_2 + H2O, \quad \text{(R 1.4)}$$

$$RO_2 + NO + O_2 \rightarrow R'CHO + HO_2 + NO_2, \quad \text{(R 1.5)}$$

$$HO_2 + NO \longrightarrow OH + NO_2, \quad \text{(R 1.6)}$$

where RH represents hydrocarbons, RO_2 represents peroxy radical $R'CHO$ represents aldehydes. Comparing R 1.3 to R 1.5, with addition of VOCs, RO_2 can oxidize NO in the troposphere, which leads to the ozone accumulation and results in ozone pollution. In addition, ozone is the precursor of the hydroxyl radical (OH) and NO_3, and during the daytime, ozone can undergo photolysis with shorter wavelength radiation by

$$O_3 + h\nu \rightarrow O_2 + O(^1D) \quad \lambda < 320nm, \quad \text{(R 1.7)}$$

$$O(^1D) + H_2O \rightarrow 2OH. \quad \text{(R 1.8)}$$

During the nighttime, ozone can be removed by

$$O_3 + NO_2 \rightarrow NO_3 + O_2. \quad \text{(R 1.9)}$$

1.2 Related Works

1.2.1 Ozone in the oil sands region

Aggarwal et al. (2017) used airborne lidar to measure ozone mixing ratio in the Alberta oil sands region. The lidar was set up in the aircraft to measure the ozone mixing ratio profile from the ground up to 1800 m. They found the ozone mixing ratio within the oil sands emission area was lower or equal to the background of ozone mixing ratio. The reason for this deficient ozone mixing ratio is that NO_x is the primary pollutant in the combustion area and about 90% of NO_x is NO. Considering the dominate exchange reaction of NO, NO_2 and O_3 (R 1.3), with the high NO mixing ratio, ozone decreases, which indicates that the ozone mixing ratio deficit is related to the NO titration.

Aggarwal et al. (2017) compared these results with ozone measurements in an industrial region in Texas and found the ozone mixing ratio is much higher than the background ozone mixing ratio at the location in Texas. By comparing the meteorological conditions of these two locations, they noticed that the daily highest air temperature at the measurement locations was usually less than 20 ^oC during their measurement time, but Houston has a daytime temperature higher than 30 ^oC. The higher temperature causes a higher oxidation reaction rate and eventually causes a higher ozone mixing ratio. However, the ozone enhancement mixing ratio is much higher than the background ozone mixing ratio in the forest fire emissions region, which indicates that the forest fire releases ozone precursors to enhance the ozone mixing ratio. Also, the analysis of a layer of high aerosol mixing ratio suggested that vertical mixing occurred in the pollutant region, where the polluted air mixed with clean air and led to the lack of ozone in the downwind area. Therefore,

Aggarwal et al. (2017) concluded the ozone mixing ratio enhancement conditions include high air temperature (greater than 20^{o}C), air stagnation, and release of air pollutants without vertical mixing.

1.2.2 Global Ozone mixing ratio variation

Logan (1985) analyzed the seasonal ozone variation based on two types of ozonesonde measurements; one is the Brewer Mast bubbler and another one is the electrochemical mixing ratio cell, which is the same as the one used in this thesis. The measurements include near-surface ozone mixing ratio and ozone profiles. Analyses of global ozone mixing ratio include the United States, Canada, Japan, Brazil, Europe, Tasmania, and the Pacific Islands. This study found that ozone mixing ratio increase in the troposphere was associated with the ozone deposition. The maximum ozone mixing ratio can be found in the United States and Europe during the summertime, which results from human activities, such as fuel combustion and agricultural burning. The increased NO_x, CO, and RH leads to increasing ozone mixing ratio. Logan (1985) found the highest ozone mixing ratio in the United States and Europe occurred in the densely populated areas and industries areas. In Canada, the maximum ozone mixing ratio usually happened in spring, and the minimum can be found in the late summer to fall, which can be explained by the ozone exchange between the stratosphere and troposphere. The combustion of vegetation increases the NO_x, RH and CO mixing ratios, which leads to the ozone mixing ratio increases, and the result showed the same as Aggarwal et al. (2018) that forest fires in Alberta increased the ozone mixing ratio in that area.

1.2.3 The interaction between ozone and NO_x in a forest

Finco et al. (2018) analyzed ozone deposition in a deciduous forest based on measurements from the understory up to above the canopy. Above the soil-atmosphere interface level, O_3, NO, and NO_2 flux measurements were based on the eddy covariance method. Soil ozone and NO_x flux measurements were based on an automated measuring system using soil chambers. This study analyzed the diurnal cycle of ozone and NO_x mixing ratio and flux (Figure 1.1 & Figure 1.2) to determine their interaction. In Figure 1.1a, ozone mixing ratio increases with height from the ground to just above the canopy and slightly decreases with height from the canopy to above the canopy (32 m to 41 m) in the daytime. The maximum ozone mixing ratio usually happened in the early afternoon, and the minimum occurred between 4:00 and 5:00 am. In Figure 1.1b, the diurnal cycle of ozone fluxes indicates ozone deposition in the forest. The ozone deposition increased with height, and at the canopy level (24 m), ozone fluxes were much higher compared to the above canopy layers.

During the daytime, stomatal deposition is the main ozone removal process. In addition, high stomatal conductance leads to high stomatal uptake of ozone. Following Ducker et al. (2018), the peak of stomatal conductance occurs when the ambient air is warm and humid. Stomatal closure occurs in the nighttime, and then the non-stomatal deposition process becomes the main ozone deposition process (Pilegaard, 2001). The dominant chemical loss process is NO reaction with O_3 (R 1.3) due to the rapid ozone removal below the canopy (Kaplan et al., 1988) and the monodirectional flux of NO and NO_2 Finco et al., 2018).

The overall change of nitrogen oxide mixing ratio decreased with height in the morning, and the peak of the NO mixing ratio at each level was around 6:00 am (Figure 1.2b). NO

mixing ratio directly above the soil (0.15 m) was higher than the upper levels within the canopy. However, NO mixing ratios were negligible in the afternoon for all other levels except the 0.15 m level. Soil is the main NO production source, and the dominant source of NO from the soil is related to biomass rather than chemical reactions.

At the crown level, the O_3 mixing ratio was higher compared to both lower levels within the canopy and upper levels above the canopy. This is because above the canopy NO_2 is decomposed by the UV light to form NO and oxygen. Higher levels of NO produced by photochemical reaction (R1.1) are transferred downward to the forest canopy and soil emitted NO transferred upward to the canopy. Therefore, NO can be accumulated at the canopy, and this leads to the high canopy level NO flux during the daytime.

Finco et al. (2018) found that during the summertime, stomatal deposition made up about 80% of the ozone removal by the forest, and 18.2% was removed by the nitrification reaction with ozone. Therefore, NO which is emitted from biogenic processes in the soil reacts with O_3 and this NO reaction causes O_3 loss from nitrification reaction, and from above canopy down to the surface, ozone can also be deposited from stomatal uptake, which explains the high O_3 deposition near the soil-atmosphere interface compared to upper levels in the forest.

Finco et al (2018) described how NO and NO_2 affect ozone mixing ratio in a boreal forest. The result from Finco et al (2018) shown in Figure 1.1a and Figure 1.2a will be used to compare with our measurements to see how the NO and NO_2 mixing ratio affect the ozone mixing ratio in the YAJP forest.

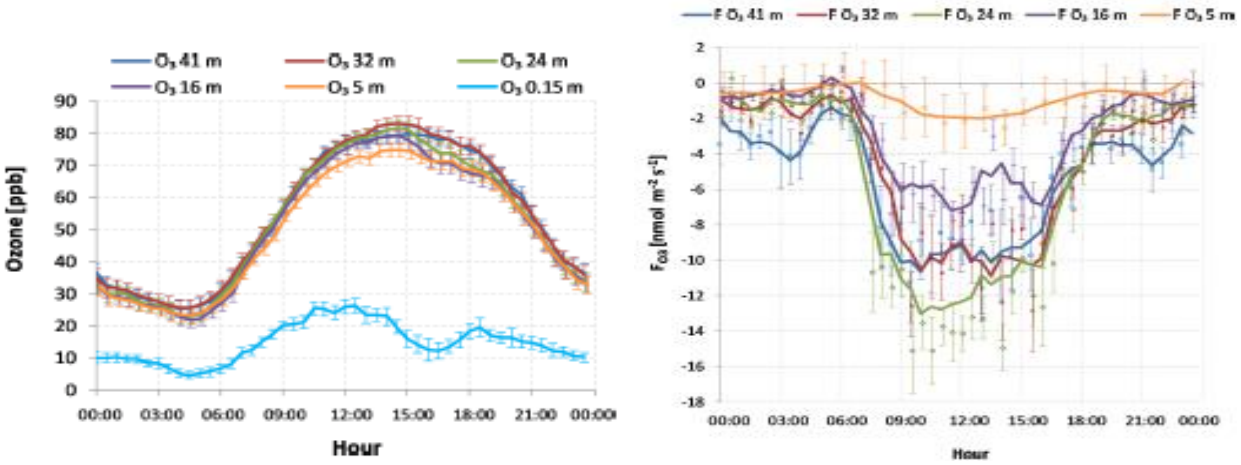

(a) (b)

Figure 1.1 (a) The diurnal cycle of ozone mixing ratio from 0.15 m to 41 m (Finco et al., 2018); (b) the diurnal cycle of ozone flux from 5 m to 41 m (Finco et al., 2018).

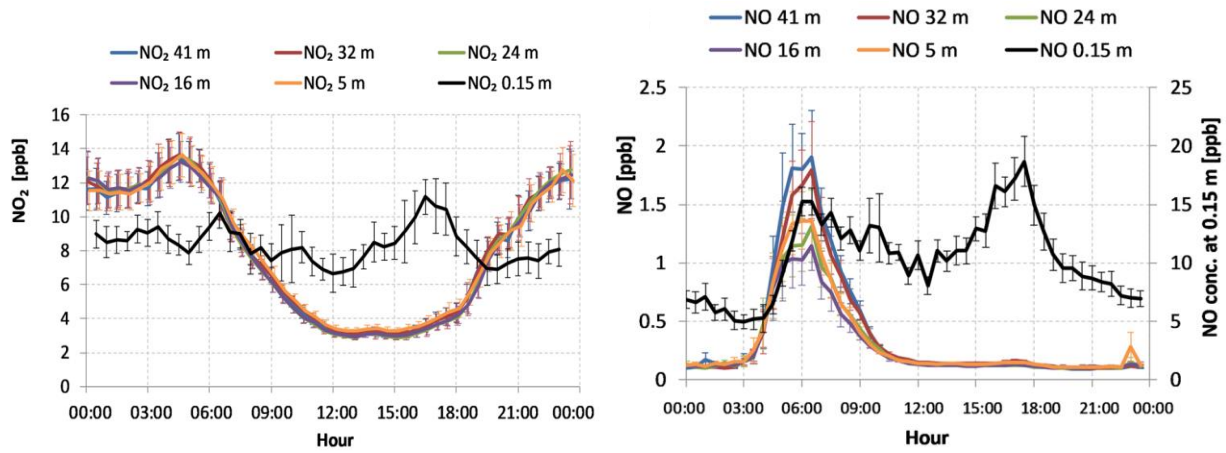

(a) (b)

Figure 1.2 (a) The diurnal cycle of NO_2 mixing ratio from 0.15 m to 41 m (Finco et al., 2018); (b) the diurnal cycle of NO mixing ratio from 0.15 m to 41 m (Finco et al., 2018).

1.2.4 Ozone variation in the boreal forest

Chen et al. (2018) compared the ozone mixing ratio with meteorological conditions in a boreal forest in Finland to analyze the surface ozone depletion. The forest canopy was about 10-12 m high. They analyzed 20 years of ozone mixing ratio and found that the ozone mixing ratio had a significant diurnal cycle in spring and summer. In autumn, the ozone diurnal cycle didn't change throughout the day compared to the spring and summer. However, in the wintertime, no evident ozone diurnal cycle can be observed. In the boreal forest, ozone concentration increases with height, which can be explained by ozone deposition from stomatal uptake and nitrification reactions.

The diurnal cycle of the ozone mixing ratio in the summertime (Figure 1.3) indicated that on the ground, the ozone mixing ratio started to decrease every day at about 8:00 pm and reached the minimum around 4:00 am. The decrease of the ozone mixing ratio happened on the ground first and then reached higher levels. Above a height of 50 m, the minimum ozone mixing ratio occurred at around 8:00 am, this is because of the lack of UV radiation in the nighttime and leads to ozone deposition. The maximum ozone mixing ratio happened at around a height of 60 m, which is about 50 m higher than the canopy, which demonstrated that ozone loss in the forest is due to the ozone deposition.

Chen et al. (2018) compared their ozone measurements with meteorological conditions and found that when the relative humidity is above 70%, this can enhance the ozone deposition rate. In addition, ozone mixing ratio can alternate based on temperature, wind speed and UV radiation, where UV radiation is the main reason of ozone mixing ratio variation in the troposphere.

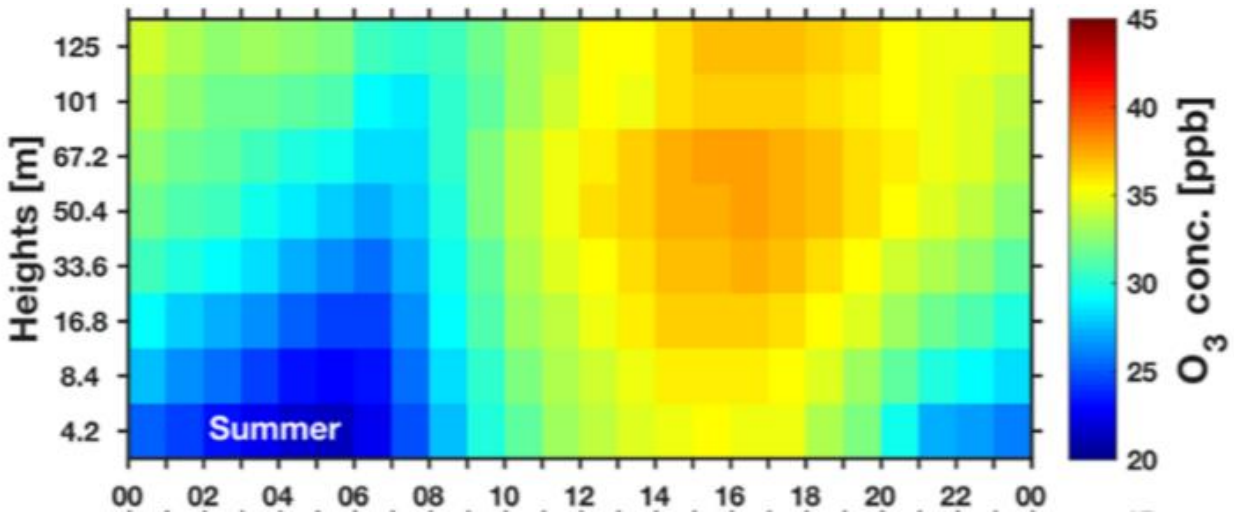

Figure 1.3 The diurnal cycle of ozone mixing ratio with height variation in the summertime (Chen et al., 2018).

1.2.5 1-D canopy model

Makar et al. (1999) created a one-dimensional canopy model to study photochemical processes. The model has 1001 levels in the vertical direction, and each level has 1 m spacing. The model uses 30-minute interval input data. It includes 268 chemical reactions associated with 79 output species. In the 1-D canopy model, the rate of change of each chemical species mixing ratio at each model level is calculated due to their emissions, chemical reactions and diffusion at each layer.

The 1-D canopy was used to analyze the biogenic emissions in a deciduous forest and how the emissions affect the formations of oxidants. The model simulated data were compared with the local measurement data to find out how precise the model is. The results showed that the simulated ozone mixing ratio matched the measured ozone mixing ratio during the first day of simulation, until the second day around noon when there was a deviation and

the simulated ozone mixing ratio was much lower than the measured ozone mixing ratio. The results suggested that high isoprene leads to low NO_x mixing ratio, which can enhance the local ozone mixing. Therefore, the 1-D canopy model underestimated the ozone mixing ratio compared to the measurement.

Stroud et al. (2005) improved the 1-D canopy model for use in a Pine forest in Duke, North Carolina. This study used the model to calculate the escape efficiency, which is the ratio of emissions above the canopy relative to within the canopy. They concluded that escape efficiency is a function of the canopy top fluxes and can be affected by the forest type. The isoprene escape efficiency calculated in Stroud et al. (2005) is 0.9, compared to the escape efficiency of 0.6 calculated by Makar (1999).

Stroud et al. (2005) used the improved 1-D canopy model to simulate the ozone, NO and NO_2 mixing ratio vertical variation from the ground up to the canopy top (Figure 1.4). They found that in the vertical direction, the modeled ozone mixing ratio has similar variation as the measurement. Although the measured average ozone mixing ratio at each vertical section is lower than the modelled ozone mixing ratio, it is still within the error range. The modelled NO_X didn't have any vertical variation, which is the same as the measurement. The net change of ozone in Figure 1.5 indicates ozone accumulates on the canopy top. Stroud et al (2005) also conclude that on the ground the ozone loss was controlled by β-caryophyllene and α, β- pinene but on the canopy top these chemicals were not significant to the ozone loss. In addition, with VOCs included in the reaction, VOCs react with NO to form NO_2. The chemical reaction (R1.5) becomes important for the ozone production from the ground up to the canopy top. Other chemicals also increase the ozone production rates

by reacting with NO, including methyl peroxy radical (CH_3O_2), isoprene peroxy radical ($ISOPO_2$), and terpene peroxy radical (TRO_2).

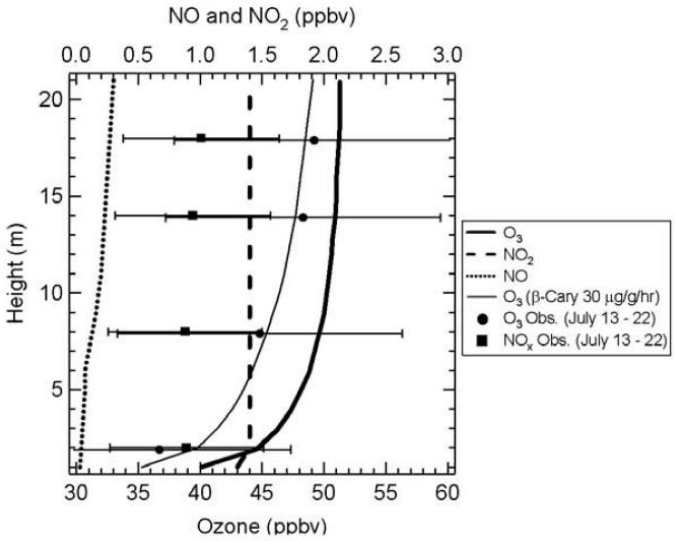

Figure 1.4 The comparison between the measured and simulated NO_x and O_3 mixing ratio (Stroud et al., 2005).

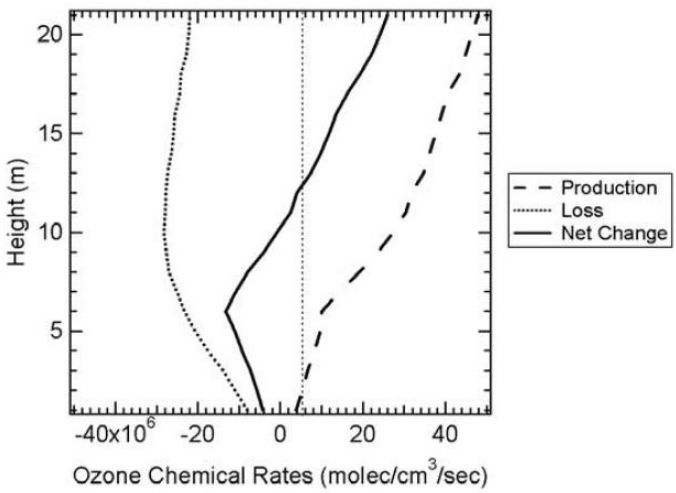

Figure 1.5 The ozone production, loss and net change vertical variation simulated by the canopy model (Stroud et al., 2005).

Gordon et al. (2014) used the 1-D canopy model to simulate VOCs (include isoprene, monoterpene, MACR+MVK and sesquiterpenes) in the Borden forest in Ontario to determine their deposition and emission rate in the forest. They found that the average error of VOCs simulation was about 6%, with ±50% NO mixing ratio difference. The model overpredicted the MACR-MVK mixing ratio in the afternoon because its doesn't include the deposition for the simulation. Isoprene is sensitive to the light in the forest. From canopy top down to the surface, the light penetration becomes weak and leads to an attenuation of isoprene from the canopy top down to the surface. Therefore, by changing the light conditions, ozone mixing ratio and transport lifetime with ±50% difference, the simulated isoprene varies from -17% to 53%. The monoterpene is less affected by these conditions from the 1-D canopy, which changes from -12 to 15%. The overall result suggests a good agreement between the modeled and measured isoprene (r^2 = 51%). however, the correlation between measurement and modelling for monoterpenes, MACR+MVK and sesquiterpenes are 27%, 26% and 11% respectively.

The model was also redesigned to be used for a boreal forest in Alberta (Gordon, 2013) to simulate VOCs. The initial run of the model in the boreal forest in Alberta showed an overestimation of isoprene and monoterpene. However, by reducing the base emission rate, the simulated mixing ratio of these two chemicals became underestimated compared to the measurement. In order to reduce the error between the simulation and measurement of VOCs in this boreal forest, the distribution for different tree species was added for the simulation. In addition, Gordon (2013) reproduced the isoprene emission rate factor as $545\ \mu g\ m^{-2}h^{-1}$ and monoterpene emission factor as $157\ \mu g\ m^{-2}h^{-1}$. The results showed a good agreement between the simulation and measurement data in isoprene, monoterpene

and MACR+MVK. The 1-D canopy model used for this thesis was based on the one used in Gordon (2013) for the boreal forest in Alberta.

1.2.6 GEM-MACH model

The Global Environmental Multiscale Modelling Air quality and Chemistry (GEM-Mach) model is an air quality model developed by Environment and Climate Change Canada (ECCC, 2020). It is an in-line model to integrated meteorology and chemistry, which was used to simulate the air pollution that affects human health such as ozone, PM2.5 and PM10.

The GEM-MACH model was used to find out how the canopy and vertical diffusion affect ozone from the surface up to the boundary layer. Makar, et al. (2016) found that using the ozone simulation model without adding canopy effects leads to the overprediction of ozone mixing ratio, which indicates the importance of the forest canopy to the ozone mixing ratio. The reason that the ozone mixing ratio decreased under the forest canopy includes ozone deposition, and the attenuation of light intensity under the canopy, which can slow down the transportation of chemicals emitted from the surface.

Makar et al. (2016) added the canopy effect into the GEM-MACH model based on Beer's law for light attenuation parameterization and the near-field diffusivity from Raupach (1989) for vertical diffusivity parameterization. The Eulerian variance (σ_w^2) was modified to the stable condition, neutral condition and unstable condition with changing the above canopy to the surface σ_w ratio. The result showed that after including the canopy influence into the GEM-MACH model, the ozone bias was decreased around 60% (depending on the

GEM-MACH model version), This results in the simulated surface ozone mixing ratio being much closer to the observation regions in North America.

The GEM-MACH model used in this thesis is a regional model with 2.5 km resolution. The air quality forecast region includes Alberta and Saskatchewan for every 24 hours simulation (Fathi, 2017). The processes of gas-phase chemistry mechanism in the GEM-MACH model simulate 42 chemical species, and deposition is included in the simulation (Anselmo et al., 2010). The emission process included primary source type and gas-phase species emission (Fathi, 2017). The location of our study site is included in the GEM-MACH model simulation domain. The data extraction location of GEM-MACH model used for this thesis is at the tethered-balloon system set up clearing (section 2.1). Both YAJP tower and tethered-balloon system are within the 2.5 km grid cell of GEM-MACH model simulation. Therefore, the GEM-MACH model simulation will be used to compare with our measurement and for deposition analysis.

1.3 Objective

The studies in section 1.2.1 indicated how the ozone mixing ratio relates to the pollutants directly emitted from fuel combustion. This jack-pine boreal forest location is surrounded by oil facilities, and the tower is located in the forest to sample both polluted and clean air, depending on wind direction. When the forest is downwind of the oil facilities, the polluted air can be detected in the forest and may have an effect on the ozone mixing ratio in the forest. This study will use data collected from the tower in the forest, a Tethered-Balloon system, and surrounding metrological stations operated by Wood Buffalo Environmental Association (WBEA, 2020) to analyze how the surrounding oil facilities affect the ozone

mixing ratio in the Jack Pine forest. The purpose of this study is to use the seasonal variation, diurnal variation, and vertical variation of ozone above and within the canopy to find out how ozone mixing ratio and deposition changes in the forest. The 1-D canopy model will be used to simulate ozone mixing ratio, which will be compared with measurements.

2. Method

2.1 Study Sites description

The study site is characterized by a homogeneous jack pine forest with flat topography. This selected forest area is far from cities, and the nearest town (Fort McKay) is about 11 km to the Northwest of the study site, with a population of only 700. The nearest highway is approximately 650 m south of the study site. The traffic on this highway is light with usually 1 or 2 trucks per minute. Thus, the effect from the town and the highway can be assumed to be negligible for this study. The study site is surrounded by oil processing and extraction facilities. The pollution detected in the forest was mainly from the surrounding oil facility plumes. The surrounding oil facilities include the Suncor facility, which is approximately 13.5 km southwest of the study site; the Syncrude facility, which is approximately 18 km southwest of the study site; the Shell Albian facility, which is approximately 13.5 km north of the study site; and the CNRL facility, which is approximately 31.2 km northwest of the study site The York Athabasca Jack Pine (YAJP) tower was first installed in July 2017 and was modified in June 2018 by adding 2B ozone monitors (see section 2.4 for details) for long-term continuous measurement. The YAJP tower is about 40 km north of Fort McMurray, Alberta (Figure 2.1). A clearing was selected about 100 meters southeast of the tower location, with an area of about 20 m by 30 m. The Tethered-Balloon system (see section 2.9 for details) was launched from the clearing between June 9 and June 16, 2018 to measure ozone variation with height.

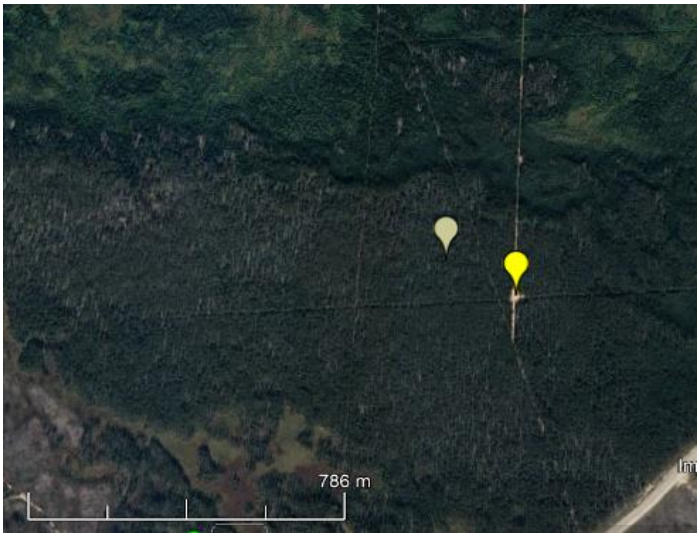

(a)

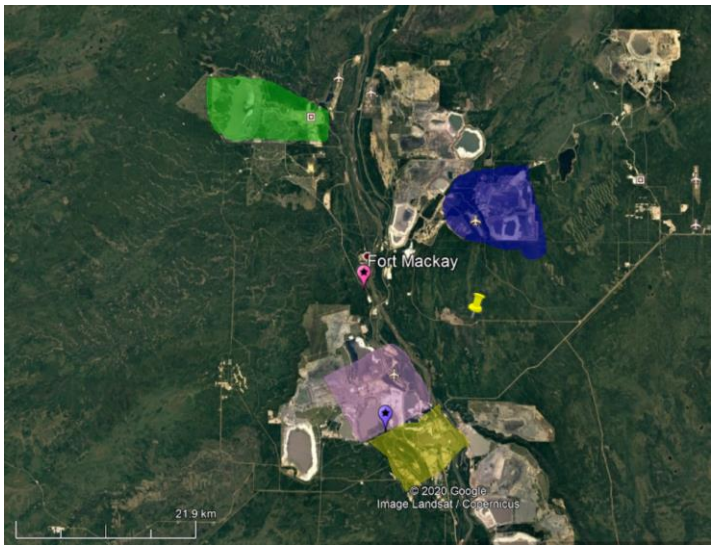

(b)

Figure 2.1 (a) The study area in Alberta. The grey spot indicates the tower site and yellow spot indicates the clearing used for the tethered-balloon measurement system. (b) The surrounding areas of the measurement sites. The yellow spot indicates the experimental field, the pink spot indicates the Fort McKay South Station, the purple spot indicates the Buffalo viewpoints station, the yellow polygon is the Suncor processing facility, the pink polygon is the Syncrude processing facility, the blue polygon is the Shell Albian processing facility, and the green polygon is the CNRL processing facility.

2.2 Study site selection

This study site was selected in 2017. To find a forest area where both clean and polluted air can be sampled, Jiang (2019) developed a stochastic back-trajectory model based on data collected from the Wood Buffalo Environmental Association (WBEA) monitoring stations to calculate the probabilities of the polluted air in each oil facility region. “polluted air” was defined as wind from the polluted area, and “clean air” as wind from the area with no oil facilities. The results showed that during the summertime, the WBEA monitoring station JP104 (WBEA, 2019) has 70% to 80% of polluted air (Jiang, 2019). JP104 is located in an area in the forest where both clean and polluted air can be sampled (considering the wind direction and surrounding oil facilities, Jiang, 2019), Based on this analysis and other considerations such as road access, the YAJP tower was set about 680 m to the North of the JP104 station in the forest.

2.3 Fort McKay South Station and Buffalo viewpoint Station

Fort McKay South Station and Buffalo viewpoint are operated by the WBEA. Fort McKay South Station is located in a Jack Pine forest, which is a similar environment, and about 13.5 km on the Northwest of the YAJP tower (Figure 2.1). It is one of the nearest monitoring stations which has NO_X measurement. Buffalo viewpoint is another WBEA monitoring station located between Suncor and Syncrude (Figure 2.1) and about 17 km Southwest of the YAJP tower. Because there was no NO_X measurement in the YAJP tower, the NO_X measurement from Fort McKay South Station, Buffalo viewpoint, and the GEM-MACH model will be used to do a NO_X sensitivity test to find out which NO_X measurement location can be used to compare with our ozone measurement for further analysis.

2.4 YAJP Tower

The YAJP tower (Figure 2.2) was first installed in the forest in July 2017. The tower is 31.4 meters high, and the canopy is about 19 meters high. During the 2018 summer intensive field campaign (June 9 to June 17), instruments mounted on the tower (Figure 2.3) included two sonic anemometers (ATI, Boulder, CO) at heights of 30.4 m and 6.3 m, two Dusttrak particle counters (TSI, Shoreview, MN) at heights of 22.9 m and 1 m, and three LI-190 light sensors (LICOR, Lincoln, NE) at a height of 30.4 m, 9 m and 1 m. A CUV5 UV light sensor (Omini, Dundee, Angus) was located next to the 1 m light sensor (LI-190). A LI-7500A CO_2/H_2O gas analyzer (LI-COR, Lincoln, NE) was mounted at a height of 30.4 m. Three 2B ozone monitors were mounted on the tower and were used for long-term ozone measurements: one located next to the 1m TSI, one located below the 6.3 m anemometer, and one mounted on the pulley system, which allows for measurement at variable heights (up to 22.9 m). One Thermo Scientific^{TM} 49i ozone analyzer, one Thermo Scientific^{TM} Model 43i SO_2 Analyzer, and an ultra-high sensitivity aerosol spectrometer (UHSAS; Droplet Measurement Technologies, Longmont, CO) were located on the ground. A Teflon tube was used to sample the air at a height of 2 m for 49i and 43i ozone and SO_2 analyzers. The 49i ozone analyzer was used as a standard measurement to compare with and correct the ground 2B measurement. The UHSAS sampled through a conductive rubber tube from a height of 30.4 m to avoid particle losses on the tube walls due to the electrostatic attraction of particles. Aerosol measurements from the UHSAS was compared with aerosol measurements from the TSI, as discussed in Jiang (2019).

During the 2017 and 2018 summer intensive field campaigns, all instruments were powered by a generator, which was placed about 100 meters northeast of the tower (corresponding to a wind direction of 50^{o}). According to the wind direction analysis in summer 2018 (from June to August) only 1.74 % of wind was from the northeast, During 2017 field study, only 1.77% of wind was from the northeast (Jiang, 2019), so we would not expect the generator plume to affect the instrument measurements. The analysis of ozone from wind direction of 40^{o} to 60^{o} is removed from the analysis during 2017 and 2018 field studies. The generator can provide about 12 hours of operation time with full filled tank of gas. We stayed on site to run the generator about 8 hours and fill the tank before leaving every day, therefore, the generator typically ran the instruments from 9:00 am to 5:00 am the next day, with no data in the early morning from 5:00 – 9:00 am. After the field campaigns, the instruments were powered by batteries and the batteries were charged by solar panels. The data from all devices are remotely transmitted to a computer at York University.

Figure 2.2 The YAJP tower and surrounding forest. The photo was taken by Mike Solohub (2018 August).

In the 2017 field study, a pulley system was set up on the tower. An ozone analyzer was attached to the rope to measure the ozone at various heights between the ground and up to a height of 30 m. The data were collected for periods of 5-minute intervals at 5-meter height intervals. The UV sensor was attached to the pulley system on the top of the 2B ozone analyzer to collect UV radiation data.

After the 2018 field experiment, two ozone monitors at 22.9 m and 2 m, one anemometer, one CUV5 and three light sensors were left on the tower for long-term monitoring. In August 2018, all instruments shut down due to the lack of power, and in November, the instruments were restarted, and the ozone instruments changed to a longer sampling duration from 5-minute period to 30-minute duration. Between November 2018 to March

2019, due to the lack of sunlight in the YAJP forest, the battery charged by the solar panel only provided the power for the tower operation. All the instruments mounted on the tower were in the energy save mode and stopped collecting data. In March 2019, the instruments started running again to collect data. The detail of those instruments' operation time from 2017 to 2018 is shown in , where the gray colour indicates that instruments were operational, and the white colour indicates no data at this time.

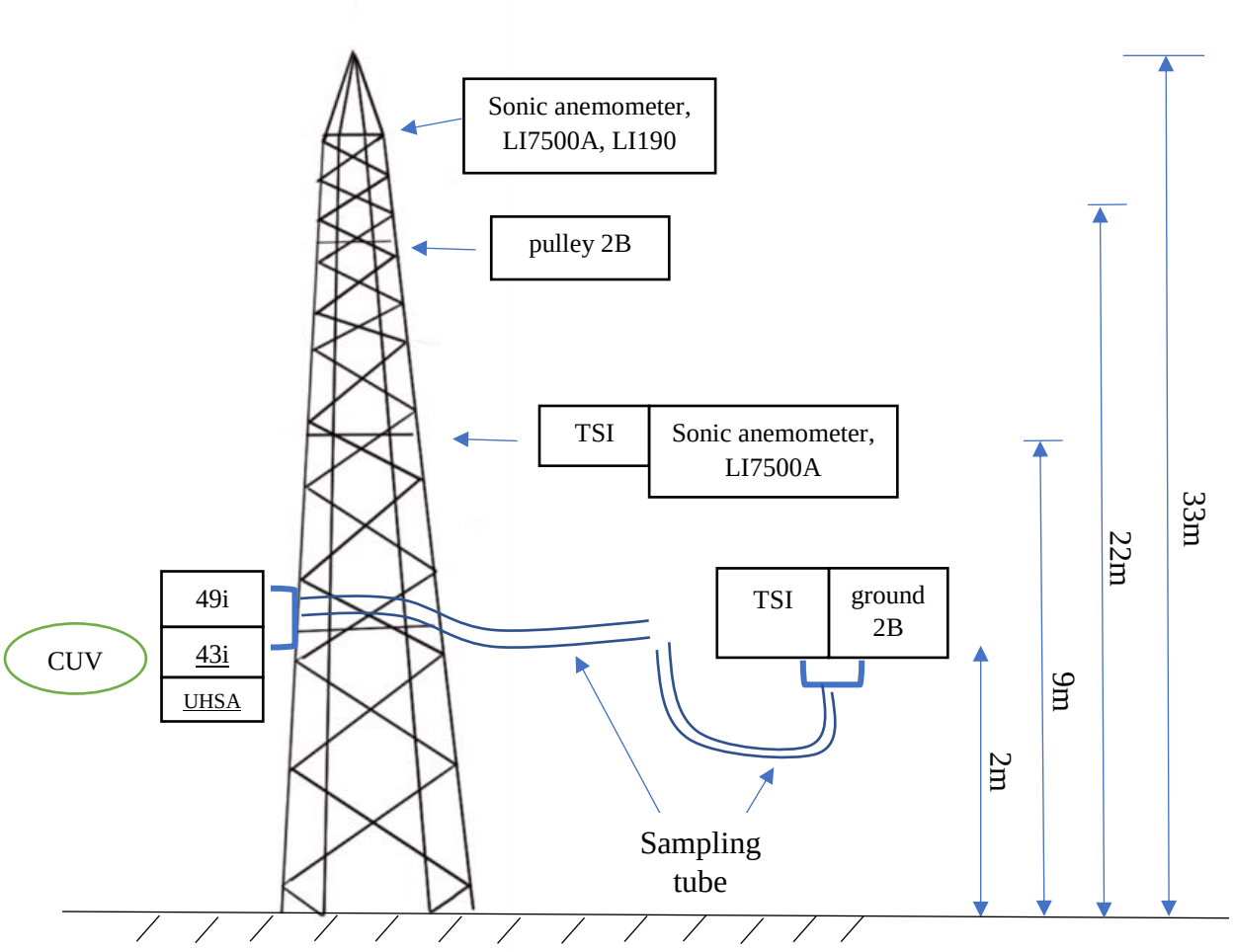

Figure 2.3 A sketch of YAJP tower and instrument mounted levels

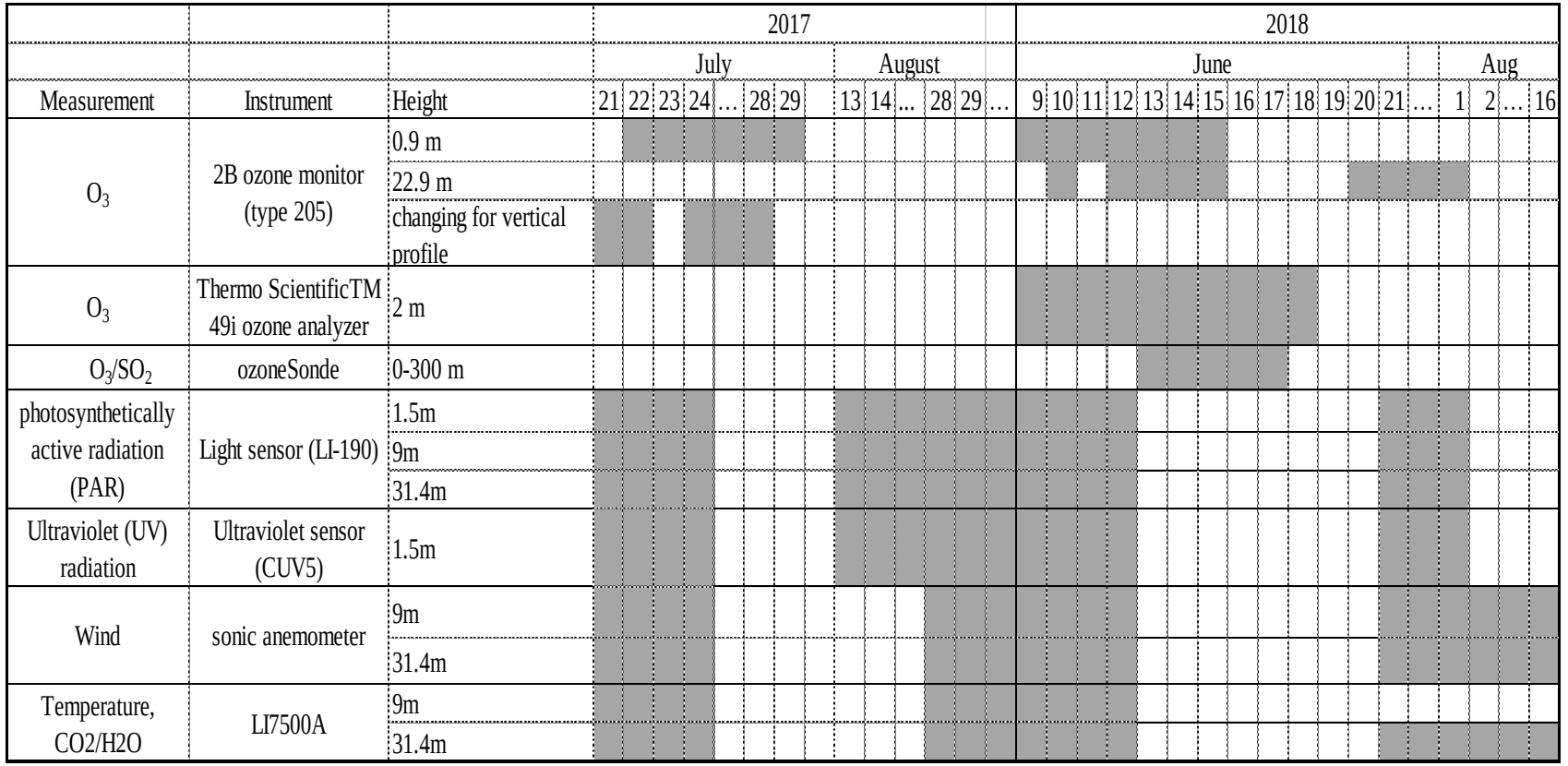

Figure 2.4 The timeline of each instrument operation time. The gray color box represents instruments is operating during. this time.

2.4.1 *2B Ozone Analyzer*

The 2B Technologies Dual Beam Ozone Monitor (2B Technologies. Inc., 2017) is an atmospheric ozone instrument with a range from 0 ppb to 250 ppm. The accuracy/uncertainty is ±2% with 0.1 ppb resolution. Because atmospheric ozone mixing ratio can be affected by the UV absorption, the measurement by ozone monitors is based on the light absorption passing through two cells (Figure 2.5). Cell 1 measures ozone-scrubbed air (I_0), where cell 2 measures ozone-unscrubbed air (I). The valve switches between cells every 2 seconds.

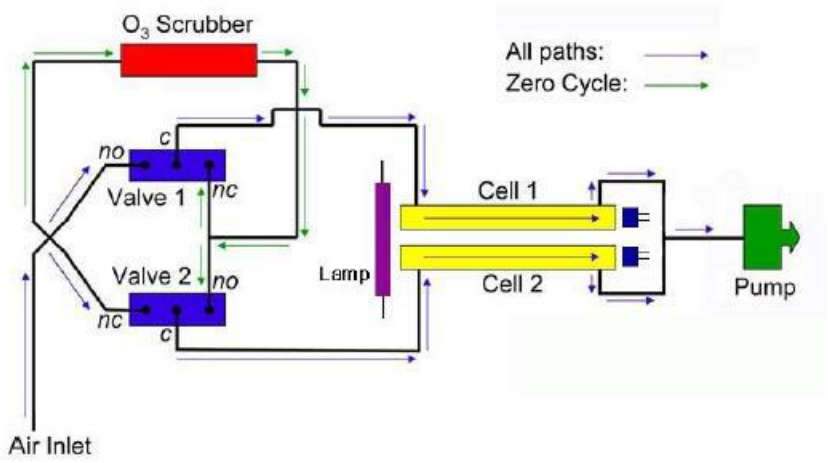

Figure 2.5 (2B Technologies Inc., 2017). The Schematic diagram of the dual-beam ozone monitor designed by 2B Technologies, Inc.

2.4.2 *Thermo Scientific Model 49i*

The Thermo Scientific model 49i measures ozone ranging from 0 ppb to 1000 ppb with ±5% uncertainty (Kim et al., 2018) and a 20-second response time. It is a dual cell photometer. The air intake is separated into two cells; one is for sample air; the other is for

reference air, which is passed through an ozone scrubber. This model uses Beer's law to calculate ozone mixing ratio absorption of UV radiation at 254 nm (Thermo Fisher Scientific In, 2011)

$$\frac{I}{I_0} = \exp(-klc) \tag{2.1}$$

The 49i was calibrated by the Environment and Climate Change Canada (ECCC) before it was used in the 2018 field campaign. During the 2018 field study, the 2B ozone analyzer and the 49i sampled from the same height of 2-m high. The 49i was used to correct the ground 2B analyzer in this thesis. In 2017, the ground 2B analyzer was the same analyzer used in 2018, which also corrected by the 49i.

2.4.3 *Thermo Scientific model 43i*

Atmospheric Sulphur dioxide (SO_2) is mainly produced by human activities, especially industrial combustion (Katz, 1949). Without human activities, the SO_2 mixing ratio is negligible in the forest. Our study site is far from the city, and the nearby highway has light traffic every day. Because of the lack of other major sources, we assume that the elevated SO_2 is due to industry smokestack plumes. Thus, comparing the SO_2 mixing ratio with wind direction can be used to determine what direction the polluted air comes from. This could help us to compare the ozone mixing ratio within the polluted air sector with non-polluted air sector and find out how the pollution from surrounding oil facilities affect ozone mixing ratio in the forest.

The SO_2 mixing ratio was measured by the Thermo Scientific^{TM} model 43i SO_2 analyzer during the 2018 field campaign. It has a high sensitivity with an 80 second response time

and was calibrated by ECCC before being used in the site. The 43i uses pulsed fluorescence spectroscopy technology based on UV light to measure SO_2 mixing ratio up to 100 ppm (Beecken, Mellqvist & Salo, 2014). The SO_2 mixing ratio was measured at the same height as the 49i measurement at 2 m.

2.4.4 *Sonic anemometers*

Two sonic anemometers were mounted on the YAJP tower (Figure 2.3) to measure the wind speed. The sonic anemometer used in this study was designed by Applied Technologies, Inc., which has rapid response to wind speed and temperature and can be used for eddy covariance method. The sampling frequency was programmed as 20 Hz in 2017 (Jiang, 2017) but switched to 10 Hz in 2018 for easier analysis and to save the power for long term monitoring.

The wind speed measured by the sonic anemometer is in three components (u, v, w) using three pairs of transducers. Each component wind speed measurement depends on the speed of sound (v_s) travel time between each pair of transducers, which can be calculated as

$$\vec{V} = \frac{d}{2}\left(\frac{1}{t_1} - \frac{1}{t_2}\right), \tag{2.2}$$

where t_1 and t_2 are the travel time from one transducer end to another end.

The wind direction was determined from the u and v components of the wind speed by converting from cartesian to polar coordinates accounting for a measured -27^o angle of the anemometers relative to true north. The comparison between wind direction and SO_2 mixing ratio can determine the direction of the pollution source. Considering the generator was set up close to the study site during the field campaign, which is about 50 degrees from

the YAJP tower, the analysis will discard the data with wind direction from 40 degrees to 60 degrees following Jiang (2019).

The LI-7500A is an open-path CO_2/H_2O gas analyzer, which measures the *in situ* CO_2 mixing ratio and H_2O vapour The LI-7500A only needs 30 W to warm up and 8-15 W power to operate (Burba & Anderson, 2010). Because the YAJP tower was powered by the solar panels after the 2018 field study, the low power requirement of LI-7500A helped us for long term continuous measurement. A thermistor was attached to the LI-7500A for temperature measurement.

2.4.5 *Light Sensors*

The UV radiation used in this study was measured by the CUV 5 UV radiometer, which was designed by the KIPP & Zonen company. UV radiation can be separated into UVC (100-280 nm), UVA (280-315 nm) and UVB (315-400 nm) based on the wavelength. Because nearly 100% of UVC can be absorbed from the stratosphere, only UVA and UVB can reach the ground. Therefore, the wavelength ranges of UV radiation measured by the CUV 5 is from 280 nm to 400 nm. The CUV 5 has 1 s response time and can measure the UV intensity up to 400 W/m^2.

Light sensors (LI-190) were used to measure photosynthetically active radiation (PAR) from 400 nm to 700 nm, which were designed by LI-COR, Inc. The LI-190 has response time of less than 1 μs with 0.005 μA s m^2/μmol sensitivity. The radiation with wavelength from 400 nm to 700 nm is the visible light on the surface that affects most plant photosynthesis (Bilodeau, 2019). In addition, the 1-D canopy model also used the PAR value to calculate the isoprene emission rate as isoprene is usually found in the deciduous

forest and is affected by the photosynthetic electron transport rate. In the 1-D canopy model, isoprene reacts with ozone to reduce simulated ozone mixing ratio. The PAR value is used to calculate cloud cover for the 1-D canopy model, which was calculated as the fraction of measured PAR relative to a selected sunny day. If the calculated fraction was less than 0, it was set to 0; and if above 1, it was set to 1, where 0 is the full cloud cover, and 1 is no cloud cover. The details of the 1-D canopy model will be explained in section 2.5.

2.4.6 *Polluted air determination*

SO_2 measurement from the 43i during the field study was used to determine the source of the pollution measured in the YAJP forest. The peak SO_2 was measured on June 13 at 9:00 am. In addition, both June 13 and June 14 had high SO_2 levels detected in the YAJP forest. We used a Gaussian plume model (Eq. 2.4) to simulate the hourly SO_2 mixing ratio for these two days to compare with the hourly measured SO_2 mixing ratio using wind direction to determine which local smokestack affected the pollutant in the YAJP forest.

$$C(x,y,z) = \frac{Q}{\bar{u}2\pi\sigma_y\sigma_z} * exp\left(\frac{-y^2}{2{\sigma_y}^2}\right) * \left[exp\left(\frac{-(z-H)^2}{2{\sigma_Z}^2}\right) + exp\left(\frac{-(z+H)^2}{2{\sigma_Z}^2}\right)\right] \quad (2.3)$$

We assume the plume is well mixed vertically through a constant boundary-layer of height z_H. Therefore, only lateral dispersion is considered (Figure 2.6). In the lateral direction, the distribution profile is

$$f(0,y,0) = \frac{1}{\sqrt{2\pi}\sigma_y} * \exp\left(\frac{-y^2}{2{\sigma_y}^2}\right), \quad (2.4)$$

where σ_y is the lateral dispersion parameter, y is the distance from the tower to the plume centreline. The y distance can be calculated as

$$y = d_{pt} sin(\theta_{pt} - (\theta - 180^o)), \quad (2.5)$$

Where d_{pt} is the distance from the plume stack to the YAJP tower, θ_{pt} represent the direction of the plume stack to the YAJP tower, which was measured from Google Earth, and θ represents the wind direction at a height of 29 m, which was extracted from the JP104 weather station. σ_y was calculated based on the Pasquill-Gifford stability classes (De Visscher, 2014), which include the wind direction, incoming solar radiation and cloud fraction to separate the atmosphere stability in to 6 class (A-F). This thesis used Briggs (1973) equations to calculate the dispersion parameter at each stability class (Appendix A).

Therefore, the SO_2 mixing ratio at the YAJP tower can be simulated as

$$C(x, y) = \frac{Q}{\bar{u} z_H \sqrt{2\pi} \sigma_y} \exp\left(\frac{-y^2}{2{\sigma_y}^2}\right). \quad (2.6)$$

The ratio of emission rate of SO_2 and boundary-layer height (Q/z_H) from the smokestack is assumed constant, and the Gaussian plume model used for this thesis is only to determine where the plume is from to determine wind direction for the polluted air in the YAJP tower. Thus, the value of Q/z_H doesn't the affect the result. The emission from source plume (Q) calculated as

$$Q = C_{max} \bar{u} z_H \sqrt{2\pi} \sigma_y, \quad (2.7)$$

where C_{max} is the maximum SO_2 mixing ratio detected at the YAJP tower and $\bar{u}$ is the average wind speed.

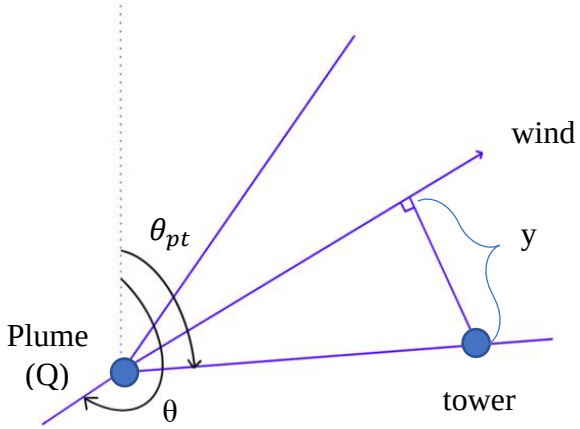

Figure 2.6 The lateral direction of plume dispersion from the smokestack to the YAJP tower.

2.5 Tethered-Balloon System

The Vaisala Tethered-Balloon system (Vaisala DigiCORA) was used for short-term ozone profile measurements (Figure 2.7). The system consists of one tethersonde (TTS111), two ozonesondes with Arduino data loggers, a balloon, a winch, the tetherline and the ground station. The balloon was filled with helium to approximately 90% capacity to account for the pressure decrease and balloon expansion with increasing height. The Vaisala Tethersonde TTS111 is a lightweight, high-resolution pressure, temperature, wind speed and wind direction (PTU) measurement instrument (Moroni et al., 2015). The safety deflate box was attached to the balloon to make sure that if the tetherline was broken, the balloon would deflate at a set altitude. The ground station includes the antenna, transmitter and data collection computer. The antenna amplified signals from the tethersonde. Amplified signals were sent to the transmitter and then transferred to the computer.

The ascent/descent rate of the balloon was controlled by the winch on the ground, and the vertical speed was set at about 0.5 m/s. The measurement requires fast ascending and

descending rates due to variation in the wind direction. The faster the balloon moves, the less variation of weather conditions at the same height, which indicates an instant profile over a short time frame. Because the project focusses on the lower tropospheric ozone mixing ratio profile, and due to aircraft flight restrictions, the measurement with the Tethered-Balloon system was limited to a height of 300 meters.

2.5.1 Ozonesonde

The EN-SCI electrochemical concentration cells (ECCs) Ozonesonde consists of the air sample system and wet-chemical ozone sensor (Figure 2.8, ECCC, 2018). The air sample system includes the Teflon sample tube and a pump motor. A high mixing ratio of ozone was required to saturate the sample tube before the measurement. The ozonesonde pump was powered by the interface card, and the interface card used 2 Alkaline 9-volt batteries for power. The interface card measured the current from the ozonesonde (Figure 2.8). The batteries can power the ozonesonde for approximately 1 hour. A program was designed and uploaded to the Arduino board to set up the timestamp and data collection from the interface card before every flight. The Arduino data logger used in the ozonesondes was designed by using one Arduino UNO board, one Deek-Robot data logging board, and two interface cards (Figure 2.5). The ozonesonde and interface cards were provided by ECCC. The initial design of data collection was to use iMet sondes to transmit data from the ozonesonde to the ground station. However, there was an incompatibility between our ozonesonde and iMet system, so we decided to design an Arduino data logger to collect data from the ozonesonde during the fight. The Arduino board was powered by 1 Alkaline 9-volt battery during the fight. All data were downloaded after the flight, and the data were

represented as XDATA, which is a hexadecimal string, including the instrument type and number, pump temperature, pump current, battery voltage and the cell current.

Figure 2.7 The Tethered-Balloon measurement system. This Figure includes the balloon, tethersonde and ozonesonde. The height difference between ozonesonde and tethersonde is about 15 cm. The ground station, antenna and winch are in the white shed.

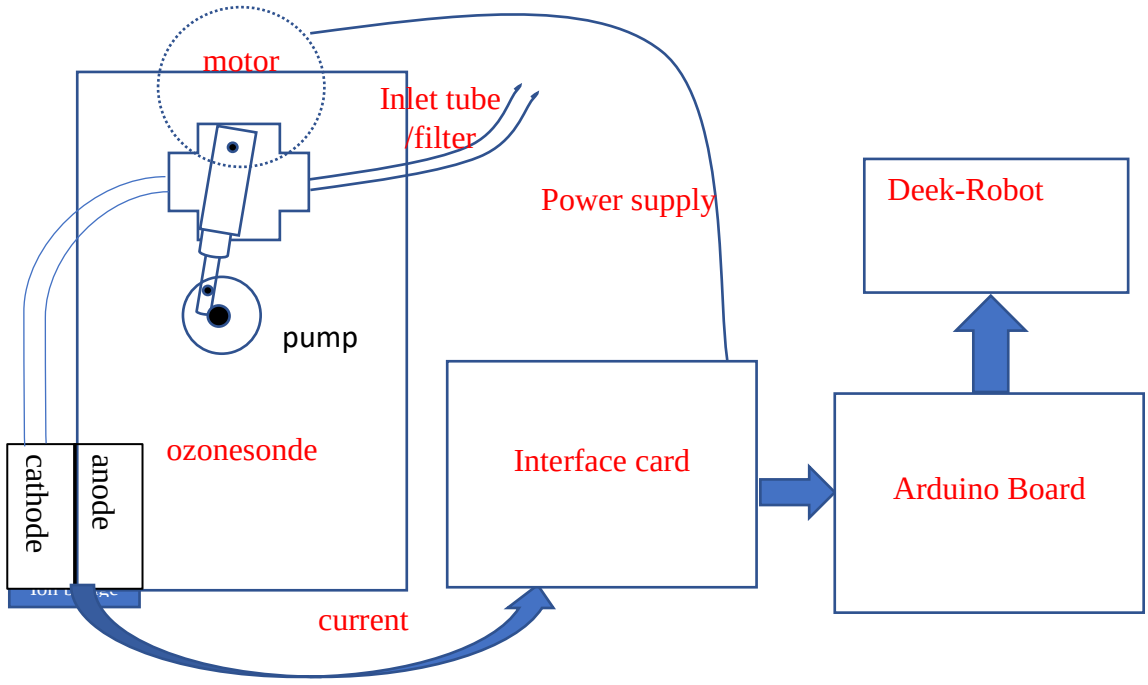

Figure 2.8 A schematic of the setup of one ozonesonde.

The ozone sensor is formed by two half-cells: cathode and anode chambers. Each cell uses different mixing ratios of KI solution, where the cathode used 3 ml 1% KI, and anode used 1.5 ml 10% KI. Once the cathode and anode have been connected, the difference between the two solution mixing ratios decrease immediately, due to diffusion of iodide through the connection. When pumping ambient air into the bottom of the cathode chamber, ozone will react with iodide to form iodine. The iodine reacts through the external circuit (shown as current in Figure 2.8) from the anode to the cathode by passing through the ion bridge (between the cathode and anode in Figure 2.8) to form iodide again, which can recharge the battery (R 2.2 & R 2.3; ECCC, 2018; Morris et al., 2010). The reaction through the internal circuit with ozone is

$$O_3 + 2I^- + H_2O \rightarrow O_2 + 2OH^- + I_2. \qquad \text{(R 2.1)}$$

The reaction through the external circuit (shown as current in Figure 2.8) is (Morris et al., 2010)

$$3I^- \rightarrow I_3^- + 2e^-, \quad \text{(R 2.2)}$$

$$I_2 + 2e^- \rightarrow 2I^-, \quad \text{(R 2.3)}$$

where (R 2.2) is the reaction with an anode solution, and (R 2.3) is the reaction with a cathode solution.

Considering that the forest was surrounded by oil facilities, and the pollution from smokestacks can produce high SO_2 mixing ratio, the cathode chamber of ozonesonde may have the reaction (R 2.4), which can replace R 2.2 to provide the electron.

$$SO_2 + 2H_2O \rightarrow SO_4^{2-} + 4H^+ + 2e^- \quad \text{(R 2.4)}$$

The reaction (R 2.4) and cathode chamber reaction (R 2.3) happened together can suppress the signal of cell current measurement, so the measured output becomes ($X_{O_3} - X_{SO_2}$). Therefore, it is crucial to remove SO_2 when using the ozonesonde. For the measurement, an SO_2 filter tube was attached to the inlet tube (Figure 2.8). The SO_2 filter tube was filled by small pieces of paper coated with the $KMnO_4$ solution. As shown in Morris et al. (2010), $KMnO_4$ can remove nearly 100% of SO_2, and the shredded paper can increase the contact area.

According to reaction R 2.1, the oxygen atom changes from ozone to oxygen, which requires 2 electrons. Measured cell current is recorded with Arduino data logger every 1-3 seconds. The flow rate was measured before each flight. The formula used to calculate the ozone mixing ratio is

$$X_{O_3} = \frac{i_f RT \times 10^9}{2e \times N_A F_f \times P}, \quad (2.8)$$

where i_f is the current measured from the ozonesonde with an SO_2 filter. The unit of i_f is Amperes; R is the gas constant with value 8.3145 J $mol^{-1}K^{-1}$; F_f is flow rate from the ozonesonde with an SO_2 filter (units m^3/s); P is pressure [Pa] at the measurement level; T is the temperature [K]; e is the elementary charge.

In order to calculate the SO_2 mixing ratio, two ozonesondes were required to fly with the balloon side by side. One of the ozonesonde with an unfiltered Teflon sample tube (without a filter) can measure the difference of SO_2 and O_3 mixing ratio (X_{O_3}-X_{SO_2}); and the other used the SO_2 filter tube to measure only the ozone mixing ratio (X_{O_3}).

Because the SO_2 mixing ratio suppresses the cell current, the SO_2 mixing ratio can be calculated as the filter tube measurement subtracted by the unfiltered tube measurement:

$$X_{SO_2} = \left(\frac{i_f}{F_f} - \frac{i_0}{F_0}\right) \times \frac{RT \times 10^9}{2e \times N_A \times P}, \quad (2.9)$$

where i_0 and F_0 are measured from the ozonesonde with an unfiltered tube. i_f and i_0 are currents in Amperes, F_f and F_0 are flow rates in m^3/s.

2.5.2 Ozonesonde preparation and SO_2 filter test

The ozonesonde preparation includes initial preparation and final preparation. The ozone bench tester provided by ECCC can be used to produce ozone-free air, adjustable ozone concentration and high ozone concentration to flush the ozonesonde for preparation. The initial preparation and final preparation for the ozonesondes need to be done before launching these ozonesondes to the tethered-Balloon system to do the measurement. The

ozone bench tester provided by ECCC can be used to produce ozone-free air, adjustable ozone mixing ratio and high ozone mixing ratio to flush the ozonesonde for preparation. The initial preparation was done on the first day of the field campaign (June 8, 2018), which was required to remove the internal contaminants of the ozonesonde (the inlet tube and cells) and activate the sensing cell (ECCC, 2018). The ozone-free air was sampled by the ozonesonde for 10 minutes to get the background cell current (Morris et al., 2010), which is around 100 mA. Thirty minutes of high ozone mixing ratio was used for flushing the internal surfaces of the ozonesonde to remove the contaminants. It was then run sampling ozone-free air for 5 minutes. To activate the sensing cell, cathode and anode solution was added and the ozonesonde was run under the low ozone mixing ratio air (0-550 ppbv, Morris, et al., 2010) to test the cell response to ozone.

The final preparation was done in the evening before each flight. Cells were recharged by replacing cathode and anode solution before the preparation, and then background cell current was measured with the ozone-free air. A decay test was used to test the ozonesonde response to ozone to calculate the maximum 1-minute point cell current. When the measured 1-minute point current was less than 5 minutes average decay current, the ozonesonde was ready for the flight. The ozone-free air cell current (background ozone mixing ratio) was subtracted from the measured cell current during the flight to calculate the real ozone mixing ratio.

The SO_2 filter test includes two parts, one uses the open tube to draw air from the ozone bench tester, and another uses the SO_2 filter. The filter test follows Morris et al. (2010) by using the same ozonesonde and pump with the same ozone mixing ratio level for both open

tube and SO_2 filter tube to test that the SO_2 filter doesn't affect the ozone mixing ratio. The test used ozone-free air for 5 minutes in the beginning and then three moderated ozone levels (~1 µA, ~2.3 µA, ~4 µA) for more than 2 minutes each until the reading became constant. The measurement from the ozone bench tester is internal current (i). The result showed that the current sampled by the sonde with the SO_2 filter was about 0.1 µA lower than the current sampled by the sonde without a filter. This is within the uncertainty range and indicated that the SO_2 filter doesn't affect the ozone mixing ratio. In addition, based on Morris et al. (2010) the $KMNO_4$ filter paper removes nearly 100% SO_2. There were three SO_2 filters that were used in the field. One filter was used per flight day and then stored in the desiccant to dry for the following two days.

Flow rate (F_f & F_0) was determined for each sonde using a Gilibrator, which generate a bubble in a flow tube and measures the moving speed of the bubble. The flow rate is calculated as the average of 10 measurements (Appendix B).

2.6 Ozone modelling

A 1-D canopy model described in Makar et al. (1999) was used to simulate ozone mixing ratio for this field location. In the 1-D canopy model, the rate of change of each chemical species mixing ratio at each model level was calculated due to their emissions (E), chemical reactions (f) and diffusion (Eq. 2.11). The 1-D canopy model only has a vertical dimension. In equation 2.11, subscript m represents different chemical species, subscript n represents the vertical layer, and K is the eddy diffusivity.

$$\frac{\partial C_{mn}}{\partial t} = E_{mn} + f_{mn} + \frac{\partial}{\partial z}\left(K(z_n)\frac{\partial C_{mn}}{\partial z}\right) \quad (2.10)$$

The dispersion model reformulates the Lagrangian dispersion model from Raupach (1989) for the Eulerian dispersion simulation to have more general usage for a canopy. The original Lagrangian dispersion principle separated the analysis into near-field and far-field. The near field theory indicates the region where chemical travel time (t) is less than the Lagrangian time scale (T_L) and far-field indicates the area where chemical travel time is longer than the Lagrangian time scale. Thus, the mixing ratio at time t and each vertical level (z) can be described as

$$C(z,t) = C(z_0,t_0)P(z,t|z_0,t_0) \tag{2.11}$$

where $C\ (z_0, t_0)$ is the mixing ratio at one model level and $P\ (z, t|z_0, t_0)$ is the single-particle transition conditional probability density with height (z-z_0) and time (t-t_0) changes. The probability can be calculated as (Raupach, 1989)

$$P(z,t|0,0) = \frac{1}{\sigma_z(t)\sqrt{2\pi}}\exp\left(\frac{-z^2}{2\sigma_z^2(t)}\right), \tag{2.12}$$

where $\sigma_z^2(t)$ is the vertical particle position variance. For homogeneous turbulence, it can be calculated as

$$\sigma_z^2(t) = 2\sigma_w^2 T_L^2\left(\frac{t}{T_L} - 1 + \exp\left(-\frac{t}{T_L}\right)\right). \tag{2.13}$$

where σ_w^2 is the Eulerian variance of the vertical velocity. In far-field dispersion, the diffusion coefficient (K) is equal to $\sigma_w^2 T_L^2$. Following Raupach (1989), an expression was derived by calculating the ratio of far-field rate to the correct rate of change as

$$R = \frac{[1-\exp\left(-\frac{t}{T_L}\right)](t-T_L)^{3/2}}{[t-T_L+T_L\exp\left(-\frac{t}{T_L}\right)]^{3/2}}, \quad t > T_L. \tag{2.14}$$

Thus, the mixing ratio rate of change due to diffusion can be calculated as

$$\frac{\partial C}{\partial t} = -\frac{\partial}{\partial z}\left(R\sigma_w^2 T_L \frac{\partial C}{\partial z}\right). \quad (2.15)$$

The input data used for the model include temperatures (T) in Kelvin, pressure (P) in hPa, ozone mixing ratios (X_{O_3}) in ppb, solar weight in fractions (W_{Sol}), water content (S_{H_2O}) in mmol/m^3, NO mixing ratio (X_{NO}) in ppb, leaf area index (LAI), diffusion coefficient in m^2/s and initial chemical species mixing ratio. Some of the chemical species (inactive VOCs) initial mixing ratio was extracted from the 1D canopy model ran in Fort McKay by Gordon (2013), which includes methane (CH4), ethane (C2H6), propane (C3H8), C4-C5 alkanes (C4AK), C6-C8 alkanes (C7AK), ethene (C2H4), terminal-bond alkenes (PRPE), internally bonded alkenes (BUTE), toluene (TOLU), xylenes (DARO), trisubstituted aromatics (TARO). Other input VOCs were set as 1 ppbv in the model. Temperature, pressure, water content and PAR value are only required at 1 height level. Therefore, these data used the above-canopy level measurements and calculated 30-minute averages. Missing points were linearly interpolated. The solar weight input also required 1 level with A 30-minute average. It is used to define the cloud fraction (Section 2.3.5). The LAI value is based on measurements from the Cumulative Environmental Management Association (CEMA, Bourque & Hassan, 2010). The LAI is height varying model, and in the 1-D canopy model, the LAI input was set as 1.84 for the modelling period. The canopy height in this model was set as 19 m, which matches the estimated YAJP forest canopy height. The actinic flux was downloaded from National Center for Atmospheric Research (NCAR, n.d.) and was reduced by a factor of 0.55 to match the observed PAR measurements.

However, this correction only decreased the modelled daily maximum ozone mixing ratio by less than 5% compared to model results using the NCAR values.

For this study, the 1-D canopy model code used the version which was edited from Gordon (2013). The model input data of temperature, NO mixing ratio and Eulerian variance of the vertical velocity were required at 50 levels with 1 m spacing for every 30 minutes. The temperature was set as constant for all 50 levels equal to the measurement at a height of 30 m. The measured ozone mixing ratio was used to initiate the model, which only affects the first day of simulation. Therefore, the first two days of simulation are not used in this thesis modelling analysis to allow for mode spin-up. NO mixing ratio was extracted from the GEM-MACH model at the surface, around 20 m and around 900 m. Linear interpolation was used to estimate NO mixing ratio from the ground up to 50 meters for the model input. The diffusion coefficient (*K* value) was required for 1001 levels for every 30 minutes and was extracted from the GEM-MACH model at the surface, around 20m, around 900m and around 1880 m in 1-hour intervals. Linear interpolation was required for every hour from 1 to 1001 m, and each half hour point *K* value was calculated as an average of the 2 nearest hourly *K* values.

3. Result and Discussion

3.1 Clean/Polluted air determination

The Gaussian plume model was used to determine where the polluted air comes from. There are four main oil facilities with smokestacks surrounding by the forest. By setting these smokestacks as the primary source of pollution, the simulated SO_2 mixing ratio from the Gaussian plume model is shown in Figure 3.1. Comparing the simulated SO_2 with the measured SO_2 mixing ratio, the pollution detected from the YAJP tower appears to be usually from Suncor, which is about 195^o to the YAJP tower. Comparing the wind direction with the simulated SO_2 from Suncor, the wind direction of polluted air detected in the YAJP area was set in the range from 165^o to 225^o. The generator was set up close to the study site during the field campaign, which is about 50 degrees from the YAJP tower (Jiang, 2019).

The long-term ozone mixing ratio and meteorological data were used for the comparison and 1-D canopy input in this thesis. During the 2018 field study, some technical issues occurred which caused the lack of meteorological data until June 19, and there was no ozone data due to the low power mode of the tower after August 1 ( ). Therefore, the overlapping period of these data (June 20 to July 31) was chosen for long term ozone analysis. Wind direction from June 20 to July 31 is shown in Figure 3.2. Most winds are from North, South, and Southwest, and oil facilities are mainly in these directions (Figure 2.1). Forest wind sector primarily comes from the Southeast (Figure 3.2) only a small fraction of winds were from the Southeast, and the wind from Southeast was weaker than the wind from the direction of the oil facilities.

The comparison between ground ozone and SO_2 measured from the 49i and 43i, respectively, during the field study is shown in Figure 3.3. The ozone mixing ratio variation followed the temperature variation at the beginning. However, from June 13 to June 14, the maximum temperature stayed almost the same, the daily maximum ozone mixing ratio decreased a little on June 13. The temperature kept increasing on June 14, when the SO_2 appeared, the maximum ozone was even lower than the day before. On June 17, the SO_2 appeared again, but with the increasing temperature, there was no evidence to show if the SO_2 mixing ratio either enhanced or suppressed the ozone mixing ratio.

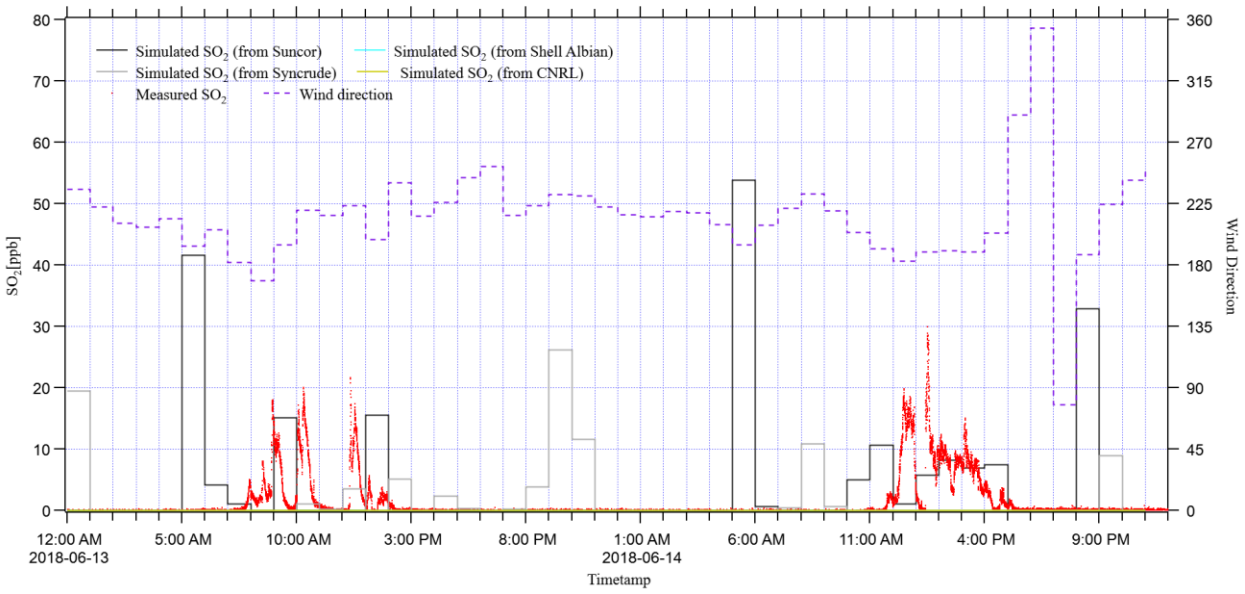

Figure 3.1 The Gaussian plume model of SO_2 mixing ratio in the YAJP forest compared with the measured SO_2 and wind direction. The Gaussian plume model was made based on surrounding oil facilities which include Suncor, Syncrude, Shell Albian, and CNRL.

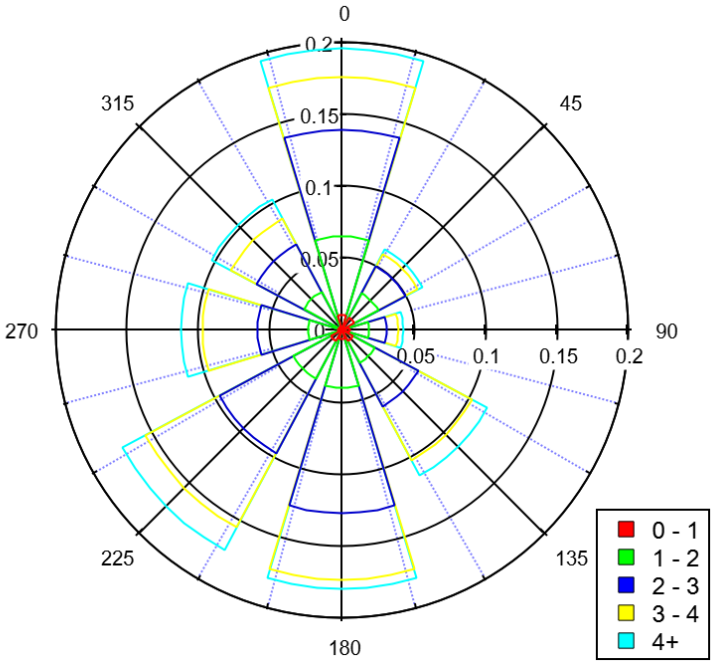

Figure 3.2 Wind direction and wind speed from June 20 to July 31 based on the sonic anemometer measurement.

Wilson, Levy, & Wimmer (1972) demonstrated that on the surface, the SO_2 can cause ozone depletion by the reaction

$$SO_2 + O_3 \rightarrow SO_3 + O_2, \qquad \text{(R 3.1)}$$

which also affirmed by Roberts (2018) that SO_2 is negatively correlated to the ozone concentration. The ozone mixing ratio on June 13 and June 14 is different from what we forecasted that with high SO_2 mixing ratio, more VOC could be expected which would enhance the ozone concentration. This may be because the measurement of ozone and SO_2 are on the surface (Figure 3.3), and the VOC concentration from surrounding oil facilities were less on the surface than we expect. Wilson, Levy, & Wimmer (1972) also mentioned that when SO_2, NO_2 and O_3 appears simultaneously, the SO_2 can react with NO_2 from

$$SO_2 + NO_2 \rightarrow SO_3NO, \qquad \text{(R 3.2)}$$

With less NO_2, ozone will finally increase, but after SO_2 disappears, ozone will increase because of increasing NO_2 concentration based on R1.1 & R1.2.

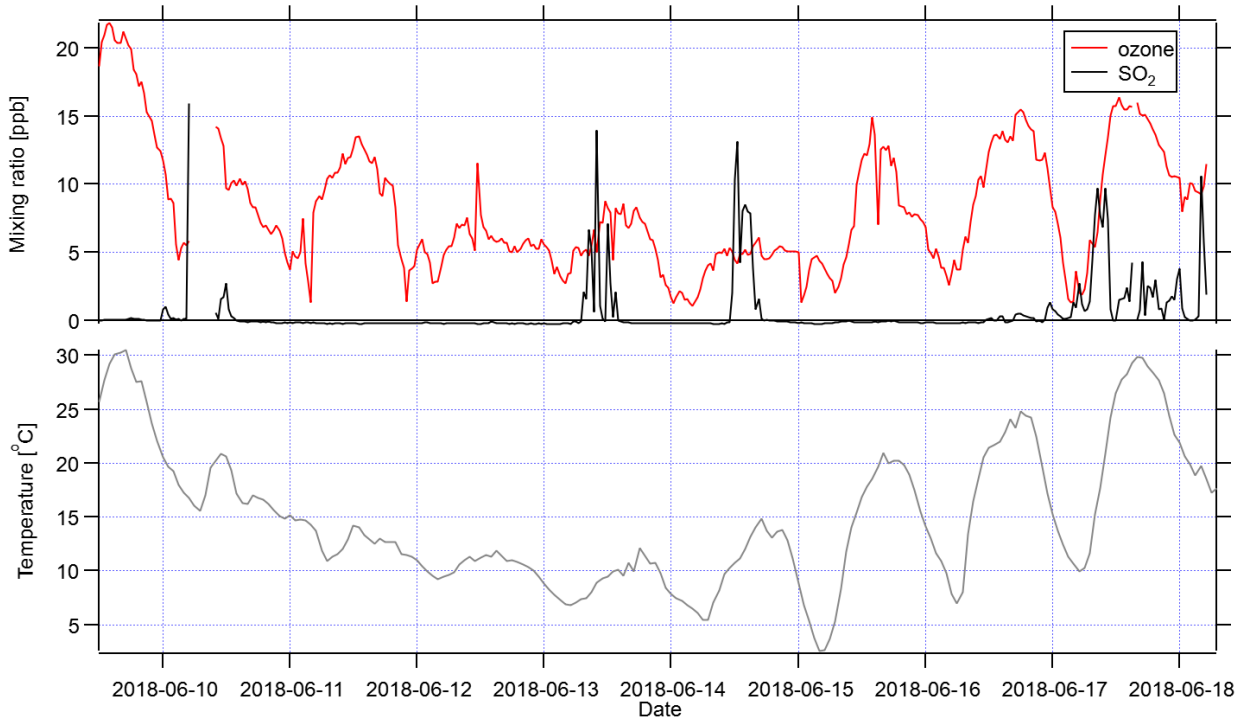

Figure 3.3 The comparison between ozone and SO_2 mixing ratio during the field study (30-minute average). 30-minute average temperature also shown in the graph.

Figure 3.4 shows the comparison of the ozone mixing ratio within the forest wind sector, the ozone mixing ratio within the industrial wind sector and the ozone mixing ratio within other wind sectors from June 20 to July 31. The measurement was taken from the pulley 2B ozone analyzer, which is above the canopy (22 m). The diurnal cycle of these three wind sectors ozone mixing ratios were plotted in Figure 3.5-3.7. From this comparison, the polluted ozone defined as ozone mixing ratio when the wind from the polluted area; the unpolluted ozone defined as ozone mixing ratio when the wind from other directions. The

result showed that the polluted ozone mixing ratio was a little bit higher than the unpolluted ozone in the afternoon from 4:00 pm to 10:00 pm. In addition, the unpolluted ozone didn't have a typical diurnal cycle, and the distributions of the ozone mixing ratio in these three wind sectors in Figure 3.8 indicated that unpolluted wind sector has less measurement data. Based on the Gaussian plume model, the pollution detected in the YAJP forest is mainly from Suncor. Therefore, to find the difference between the wind from Suncor and all other wind sectors, the wind that is not from Suncor set as non-polluted air (forest wind sector and other wind sectors), and the wind from Suncor set as polluted air to avoid the bias of less measurement data. By comparing the polluted and unpolluted ozone diurnal cycle (Figure 3.7), we found that the pollution from surrounded oil facilities can enhance the ozone mixing ratio from 4:00 pm to 4:00 am, and the average enhance was about 6 ppb (20%), however, from 6:00 am to 11:00 am and from 12:00 pm to 4:00 pm, the polluted air has lower ozone mixing ratio than the unpolluted air. Our study's result does not agree with Aggarwal et al. (2018) result in Alberta oil sand region in 2013. In Aggarwal et al. (2018), the overall trend has no evidence to show the plume can enhance the ozone mixing ratio in the downwind forest area. Some observations in other locations such as in Houston or Baton Rouge suggested that the industrial plume can enhance ozone mixing ratio about 2 to 3 times higher (Henderson et al., 2010), and in Malaysia, the ozone mixing ratio is higher in the downwind area within a plume (Abdullah et al., 2017). This is because the plume produces VOCs, which can transfer in the downwind area and lead to ozone accumulate in the downwind area. Our result agreed that the plume can enhance ozone mixing ratio in the afternoon, which is highly related to the temperature. Aggarwal et al. (2010) also concluded that the main reason their measurement didn't show the ozone

enhancement with industrial plume compared to the Houston's measurement is the temperature, when the temperature is over 20^{o}C, the industrial plume can enhance ozone mixing ratio. Therefore, in Figure 3.10, the comparison between the daily average ozone mixing ratio and daily maximum temperature were required to find out the condition of plume enhancement related to the temperature. The result indicated there were some enhancement when the temperature was over 20 ^{o}C, and wind speed was lower than 3 m/s such as from June 21 to June 23, from June 29 to June 30 and from July 26 to July 28, and the enhancement of ozone mixing ratio was about 15% (about 4 ppb), except on June 26, June 30 and July 12.

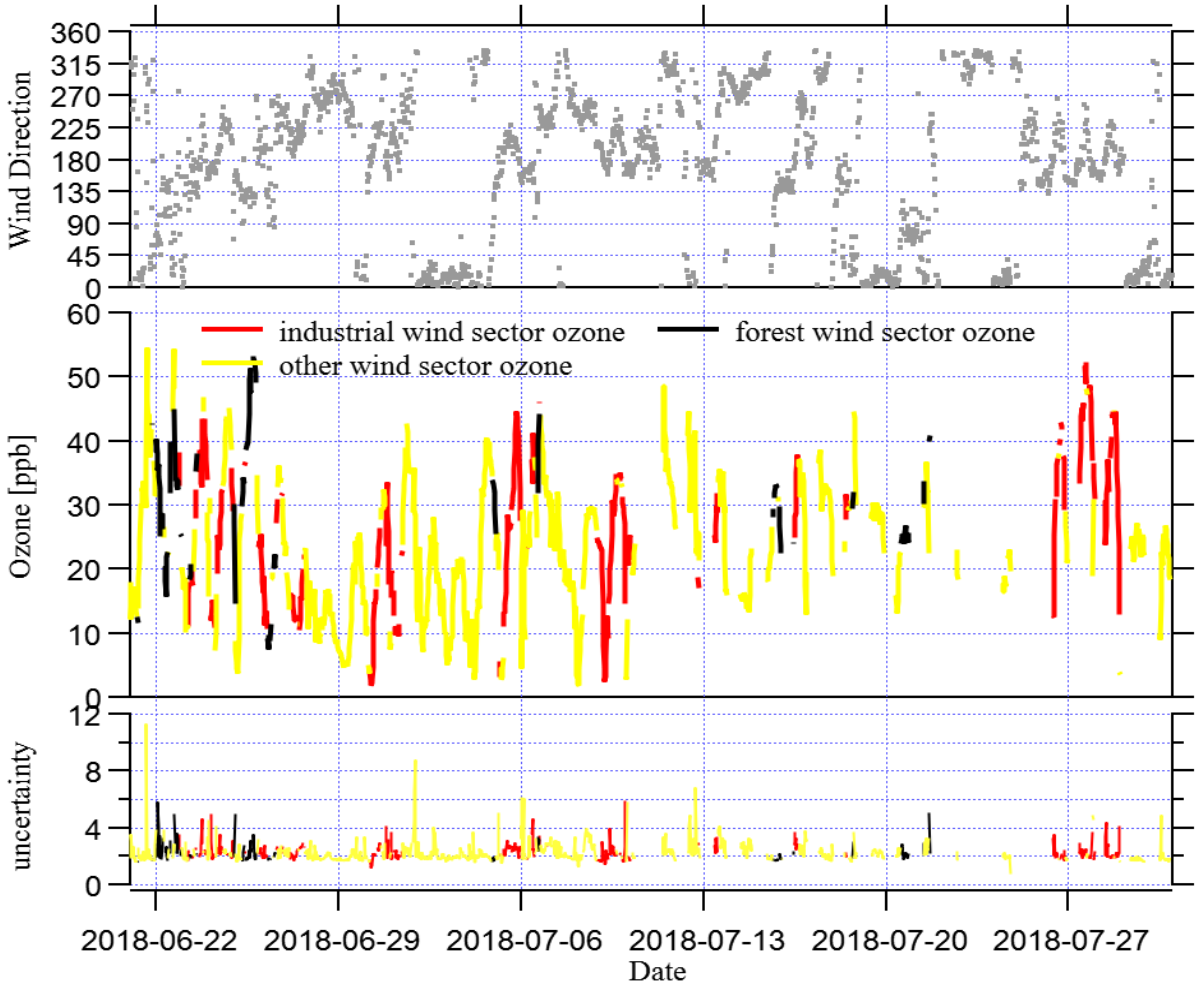

Figure 3.4. The comparison between the 30-min measurement background ozone and polluted area ozone, the uncertainty was calculated based on the standard deviation within 30-min measurement interval.

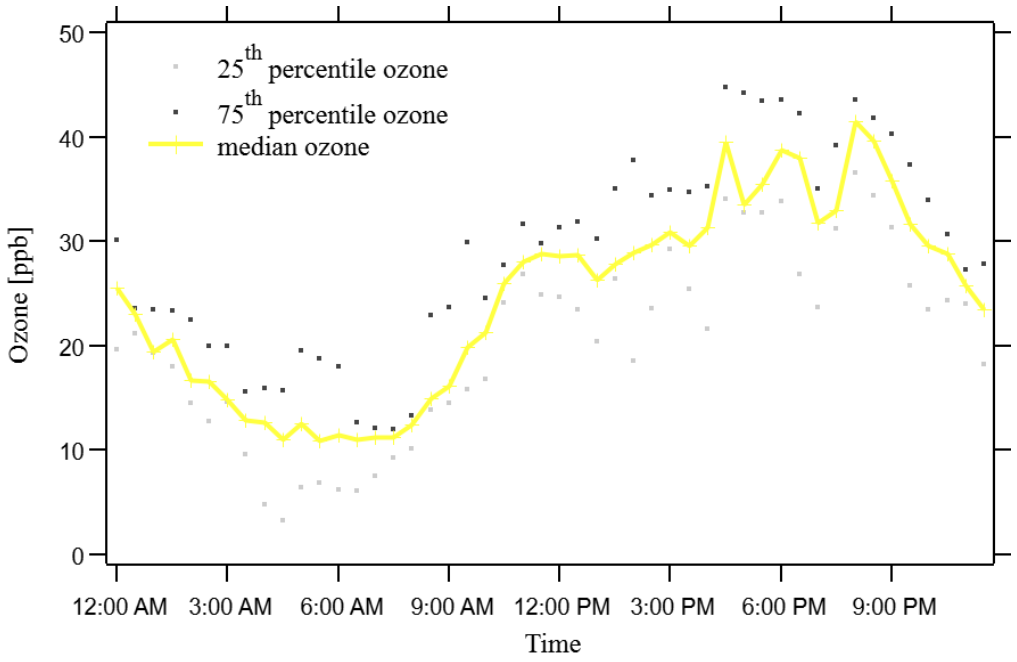

Figure 3.5 The industrial wind sector Ozone diurnal cycle based on July measurement.

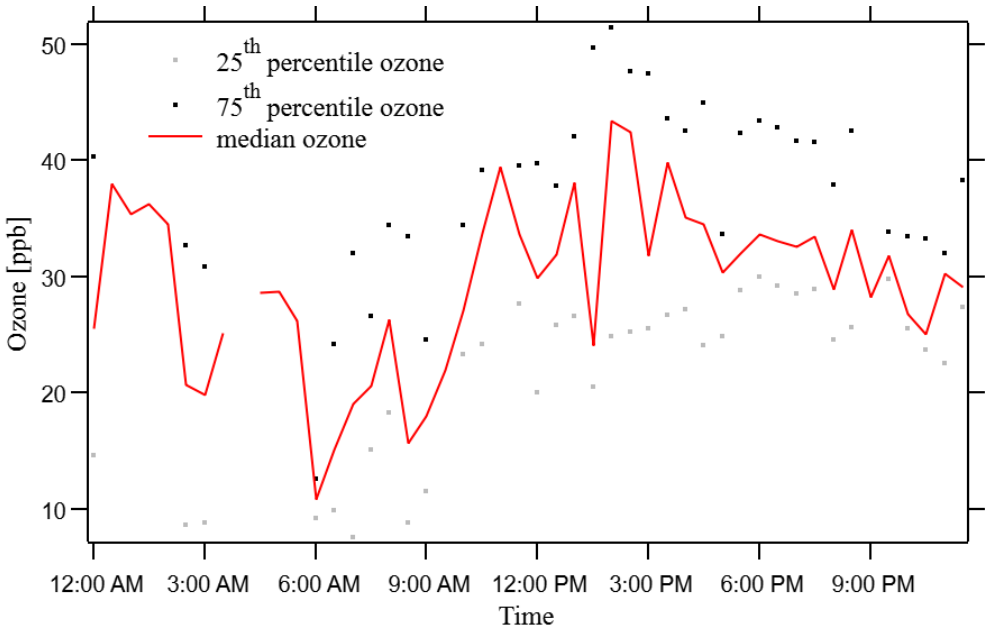

Figure 3.6 The forest wind sector Ozone diurnal cycle based on July measurement.

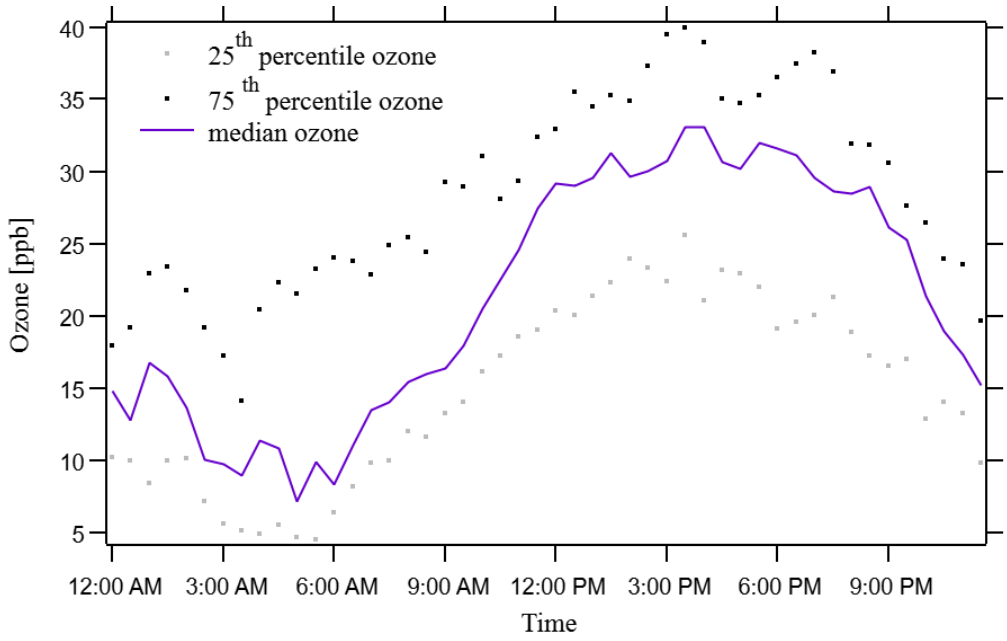

Figure 3.7 All other wind sectors ozone diurnal cycle based on July measurement.

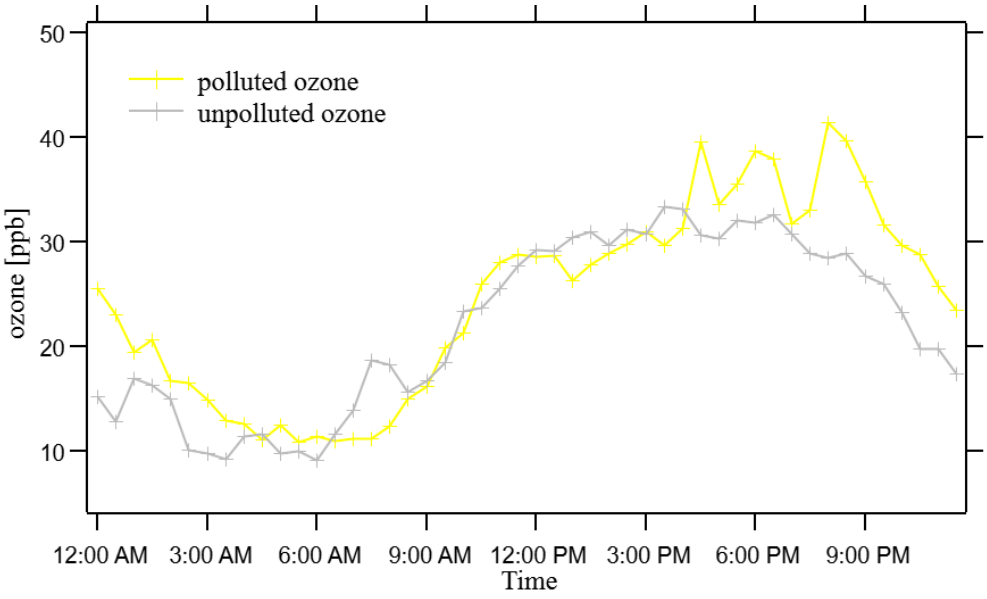

Figure 3.8 The comparison of polluted and unpolluted wind sector ozone diurnal cycle.

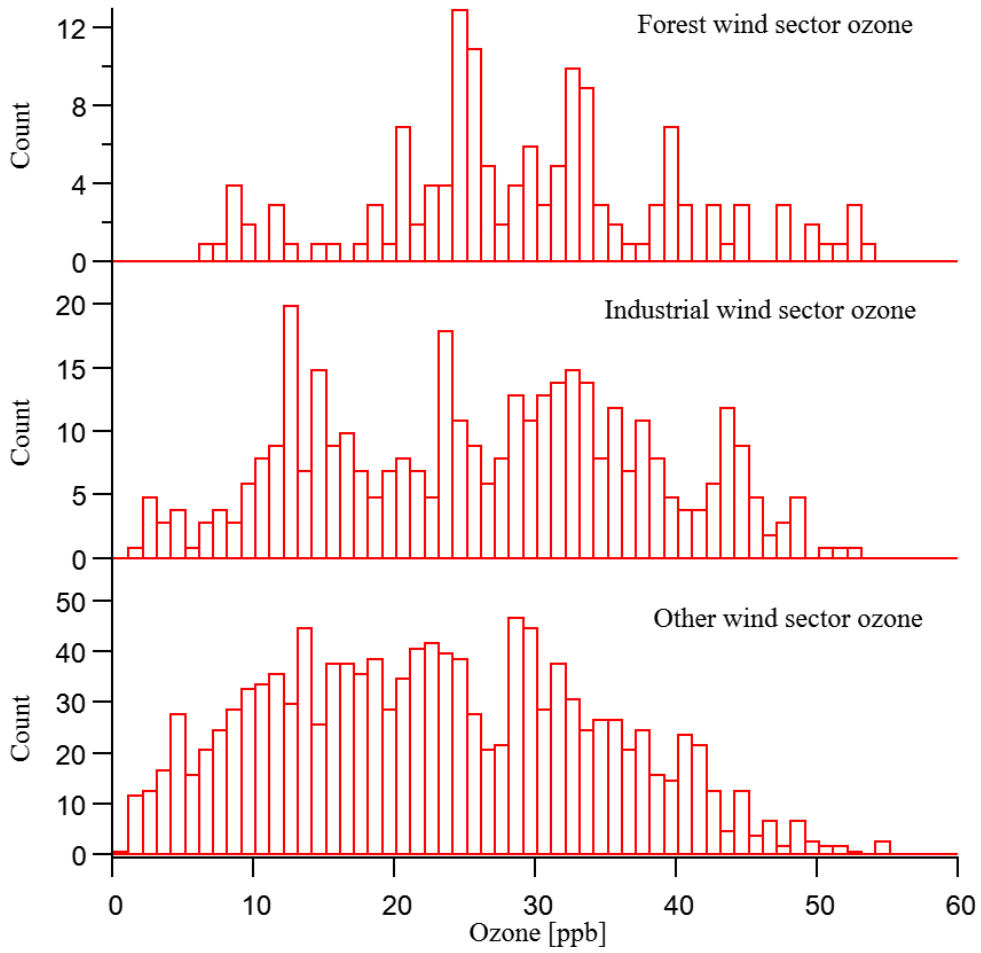

Figure 3.9 The distribution of ozone mixing ratio in industrial wind sector, forest wind sector, and other wind sectors.

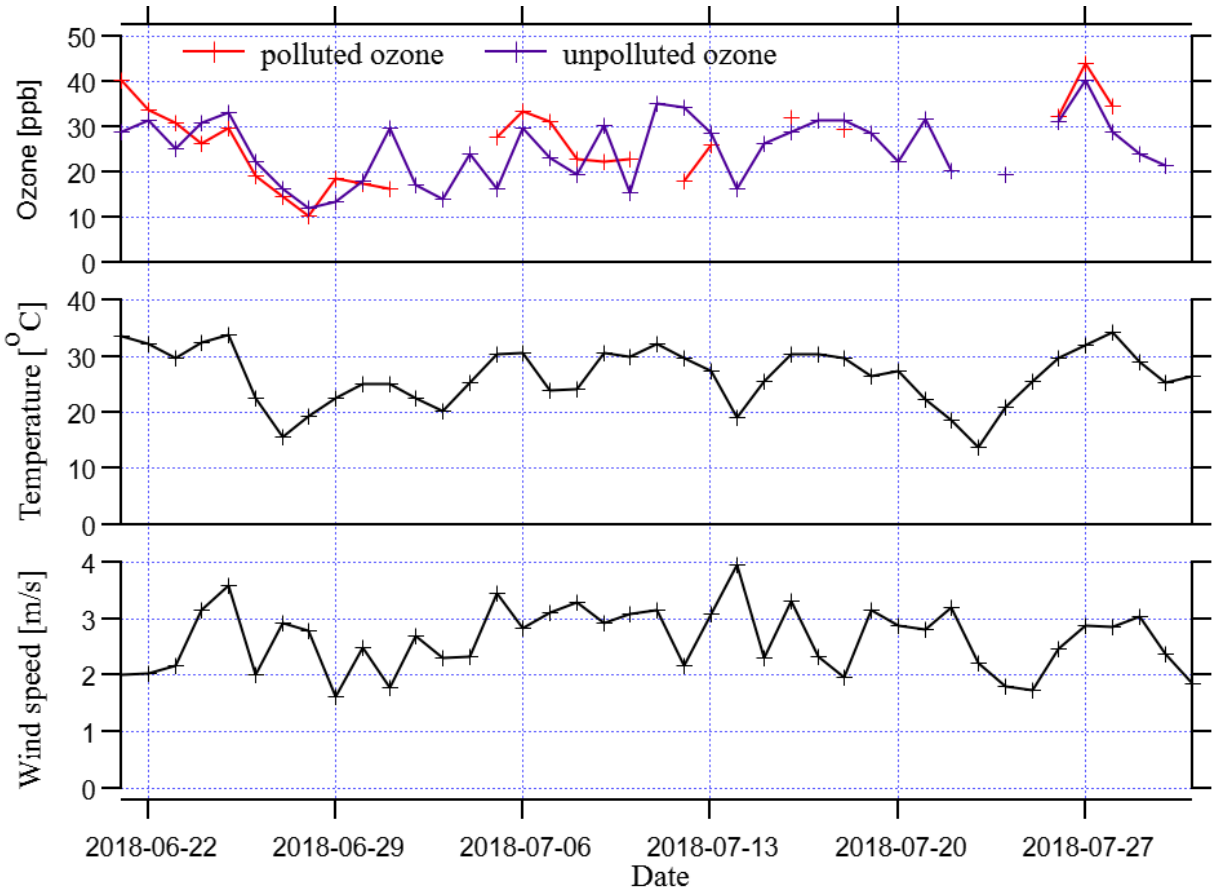

Figure 3.10 The comparison of daily average ozone mixing ratio and daily maximum temperature.

3.2 NO_x sensitivity test

The NO_x sensitivity test is used to test how sensitive the model is to the location of NO_x input mixing ratio measurement from either Buffalo viewpoint, Fort McKay South Station or the GEM- MACH model. By comparing the ozone mixing ratio from 2B measurement at 22 m level with Buffalo viewpoint ozone measurement (WBEA), Fort McKay South Station measurement (WBEA) and GEM-MACH simulated ozone mixing ratio at 22 m. The result indicated that from June 20 to July 31, 2018, the correlation (r) between Buffalo viewpoint and our measured ozone mixing ratio was approximately $r = 79\%$, however, the

ozone mixing ratio in Buffalo viewpoint were about 2 ppb higher than our measurement in 2018. The correlation between Fort McKay South Station and our measurement was about 69%. The lowest correlation (r) was between the GEM-MACH simulated ozone mixing ratio and our measurement, which was about 57%. Figure 11 shown the ozone mixing ratio of these four measurements (or simulation) for 1 week from June 22, 2018 to June 29, 2018. During this period, the Buffalo viewpoint ozone measurement and our measurement has the similar variation and values. However, the Fort McKay South Station ozone measurement only has the similar variation and values to our measurement in the morning. In the afternoon, the Fort McKay South Station ozone measurement was much lower than our measurement. The GEM-MACH ozone simulation overpredicted ozone mixing ratio by more than 50% during the comparison period. The NO and NO_2 measurements from selected WBEA stations and GEM-MACH simulations are shown in Figure 3.11. There was a spike in NO and NO_2 mixing ratio on June 24 and June 25 from GEM-MACH simulation. A spike of NO mixing ratio on June 25 from Fort McKay South station also shown in Figure 3.11. There were no obvious NO and NO_2 spike from Buffalo viewpoint, and the NO mixing ratio were lower than 10 ppb.

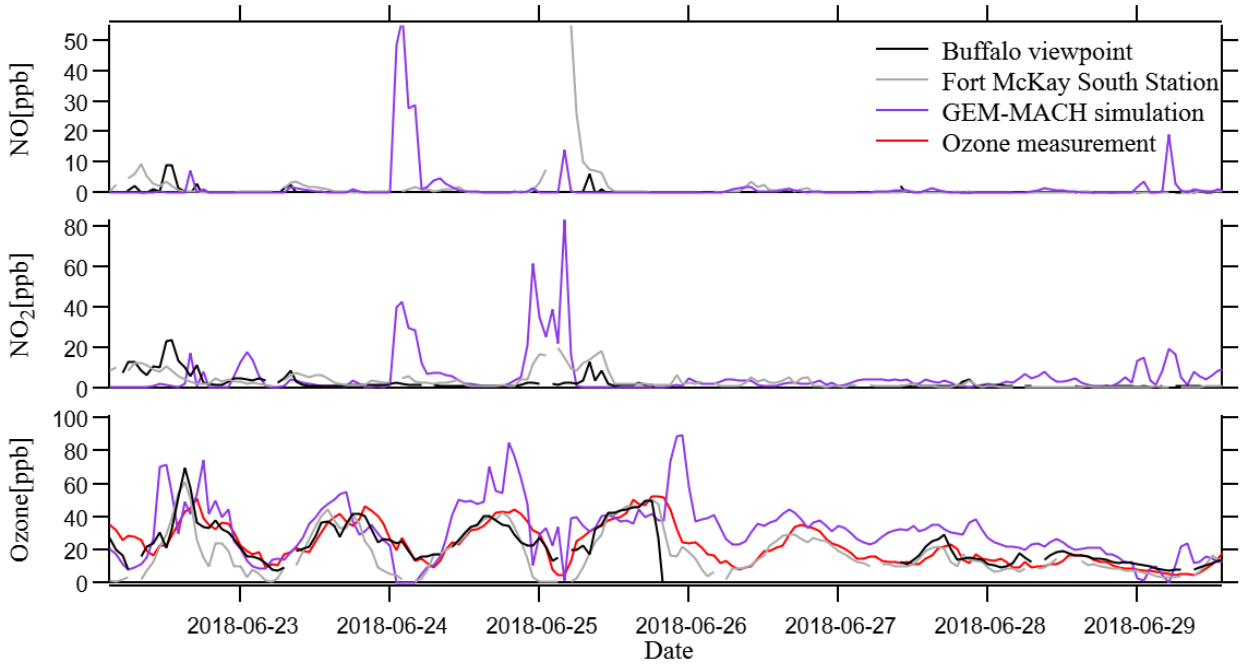

Figure 3.11 The measured ozone in the YAJP forest compared with ozone measurement (or simulation) from Buffalo viewpoint (WBEA), Fort McKay South Station (WBEA) and GEM-MACH model simulation to determine model sensitivity to NO_x measurement location (or simulation).

3.3 Ozone mixing ratio with meteorological variation

Ozone mixing ratio is highly related to the air temperature (Figure 3.12a), and there is a positive relationship between temperature and lower tropospheric ozone mixing ratio, with a correlation coefficient (r) value around 80.1%. By doing regression tests, the temperature is significant (*P-value* < 0.05) to the lower tropospheric ozone mixing ratio, which means this correlation also happens in large population. At the same altitude, higher ozone mixing ratio is usually associated with higher temperature and lower pressure level. This is because, the temperature is associated with UV radiation. High temperature usually happened in the early afternoon, and more UV radiation gets to the ground to increase

oxygen atom formation from NO_2 decomposition reaction (R1.1) and leads to a higher ozone mixing ratio. In addition, the higher temperature can accelerate the ozone precursors formation, and lead to more ozone formation. In the afternoon, the solar radiation reaches a maximum and reacts with high ozone precursors (Stathopoulou et al., 2008), which may also affect ozone production rates. The regression test between the ozone mixing ratio and daily maximum UV radiation indicated that the daily maximum UV radiation is significant to the ozone mixing ratio and the correlation coefficient is 34.2% (Figure 3.12b).

Chan (2009) analyzed the meteorological conditions' effect on ozone mixing ratio in Canada from 1997 to 2006 and found that lower wind speed is usually associated with a higher ozone mixing ratio, which is similar to what is seen at the YAJP site (Figure 3.13a). In our study, the daily maximum temperature was separated into 4 categories to determined how the wind speed affects the ozone mixing ratio. The result indicated that the ozone mixing ratio is negatively correlated to the wind speed. When the temperature was lower than 20 ^{o}C, the correlation coefficient between the ozone mixing ratio and wind speed is -97.1%. When the temperature was between 20 ^{o}C and 25 ^{o}C, the correlation coefficient is -42.3%. For temperatures from 25 ^{o}C to 30 ^{o}C, the correlation coefficient is -62%, and when the temperature was over 30 ^{o}C, the correlation coefficient dropped to -17.6%. The result indicated the ozone mixing ratio is related to the wind speed when the temperature is lower than 30^{o}C. Figure 3.13b shows the correlation between ozone and wind speed separated into 4 categories related to the relative humidity. The high correlation coefficient between daily maximum ozone mixing ratio and daily average wind speed is when the relative humidity lower than 30% (r = -86.7%), and the moderated correlation coefficient is when relative humidity was higher than 50% (r = -48.1%). When Relative humidity was between

30% and 50%, the correlation coefficient was as low as -24%. The lower wind speed and relative humidity causing high ozone mixing ratio can be explained by the air stagnation, where air pollution cannot be cleared and causes ozone accumulation.

According to ozone photochemical reactions (R1.1 – 1.3), ozone mixing ratio is not only affected by the UV radiation but also related to the NO and NO_2 mixing ratio. Figure 3.14 is the comparison of daily maximum UV radiation, daily average NO mixing ratio and NO_2 mixing ratio. Wind direction plotted from June 20 to July 31 based on the sonic anemometer indicates that the wind is usually from the southwest, and the from the NO_x sensitivity test, the Buffalo viewpoint station ozone measurement was the closest to the 2B measurement from YAJP tower. Thus, the NO and NO_2 mixing ratio downloaded from the Buffalo viewpoint station as 5-min average were used to this comparison. The result shown in Figure 3.14 indicates that high NO mixing ratio is associated with high NO_2 mixing ratio, with high daily average NO and NO_2 mixing ratio, both the reaction of ozone production and removal are accelerated. The result indicates that in the daytime, the ozone production reaction is the primary reaction (R 1.1 & R 1.2) and during the nighttime, ozone removal reaction (R 1.3) becomes the primary reaction.

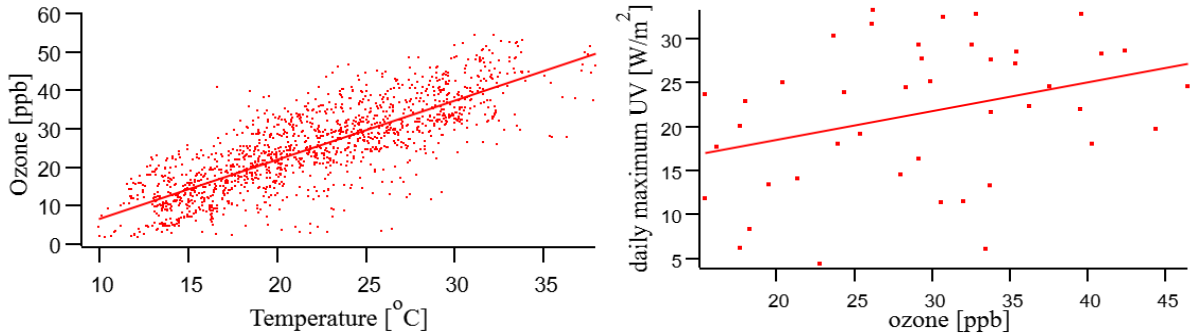

(a) (b)

Figure 3.12 The correlation between (a) 30-minute average ozone mixing ratio and temperature; (b) daily maximum UV radiation and ozone mixing ratio.

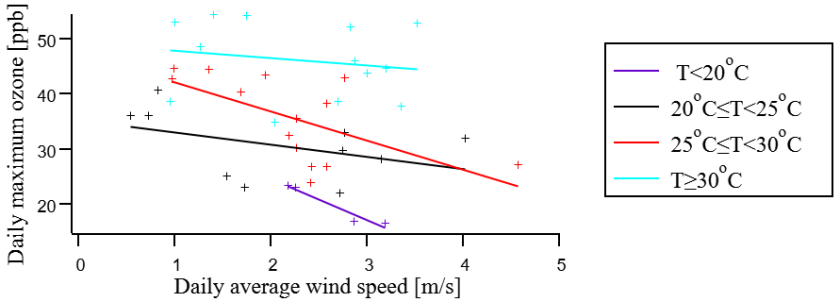

(a)

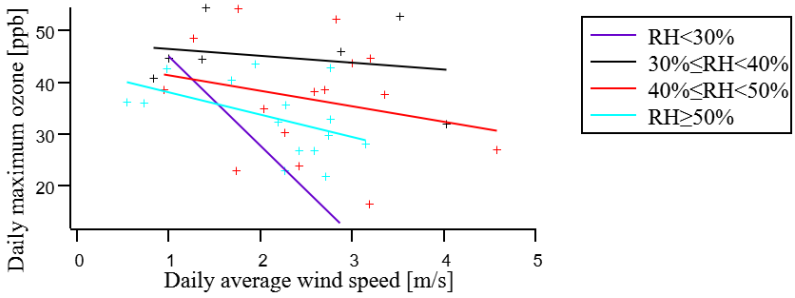

(b)

Figure 3.13 Daily maximum ozone mixing ratio and daily average wind speed separated into four categories related to (a) daily maximum temperature and (b) daily average relative humidity.

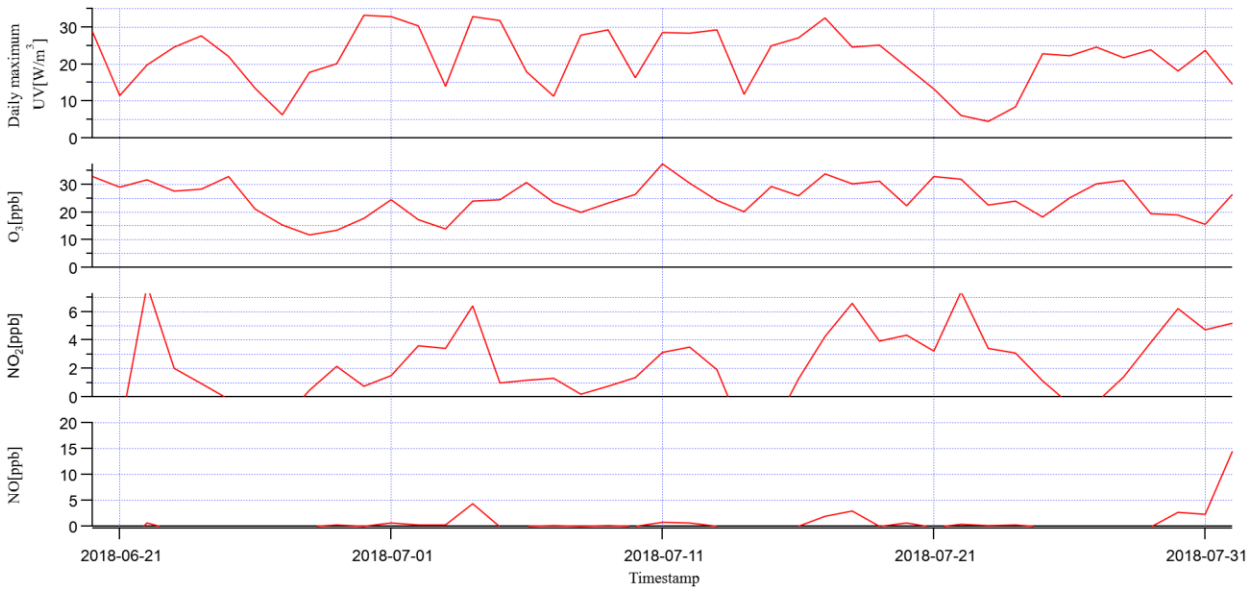

Figure 3.14 A comparison of daily maximum UV radiation, daily maximum O_3 mixing ratio, daily average NO_2 mixing ratio and daily average NO mixing ratio.

3.4 Diurnal Cycle

The ozone diurnal cycle was calculated based on the 2B ozone monitor measured above the canopy on the YAJP tower (Figure 3.5-3.7). The daily lowest ozone mixing ratio usually happened near 5:00 or 6:00 am, after that the mixing ratio went up until 3:00 to 5:00 pm to reach the maximum and then went down until the next day. The diurnal cycle demonstrates that a high ozone mixing ratio occurred in the afternoon when high photolysis is likely. The lowest ozone mixing ratio occurred at midnight, when less or no photochemical reaction happened and low BVOCs mixing ratios were emitted from the forest. By comparing three wind-sector ozone diurnal cycle, the industrial (Figure 3.5) and other wind sectors (Figure 3.7) are shown to have a greater variation from nighttime to daytime compared to the forest wind sector ozone diurnal cycle. The low variation forest wind sector ozone diurnal cycle (Figure 3.6) can be explained by less anthropogenic emissions. As mentioned in Xu et al.

(2020), with less anthropogenic emissions (such as population, industrial, transportation), the surface ozone mixing ratio mainly depends on vertical transportation from the stratosphere or free troposphere.

The diurnal cycle of NO mixing ratio (Figure 3.15) showed that the peak NO mixing ratio was around 9:00 am. NO is the primary pollutant. After 9:00 am, the intensity of solar radiation increased, which leads to the photochemical reaction (R 1.1) becoming rightward. More NO_2 is formed, and finally increases the ozone formation to let the ozone mixing ratio reach the highest concentration at around 5:00 pm. During the nighttime, there is no solar radiation and the photochemical reaction is stopped. Ozone breaks down with NO to form NO_2 (R 1.9), which explains the nighttime peak of the NO_2 mixing ratio in Figure 3.16.

The NO_x diurnal cycle (Figure 3.17) was calculated as the sum of NO_2 and NO mixing ratio. The highest NO_x mixing ratio was observed in the morning (around 8:00 am), and the lowest NO_x mixing ratio was in the afternoon (around 5:00 pm). After that there was an increase of NO_x mixing ratio until next day in the morning. The detected NO_x mixing ratio in the forest is mainly from the combustion from nearby oil facilities, and Pancholi et al., (2018) mentioned the high NO_x mixing ratio happened in the evening and early morning may because of the low air mixing in the nighttime with low atmospheric boundary layer occurred. In addition, NO_x mixing ratio from the WBEA Buffalo viewpoint station and ozone mixing ratio measured from the YAJP forest are negatively correlated with -73.7% correlation coefficient.

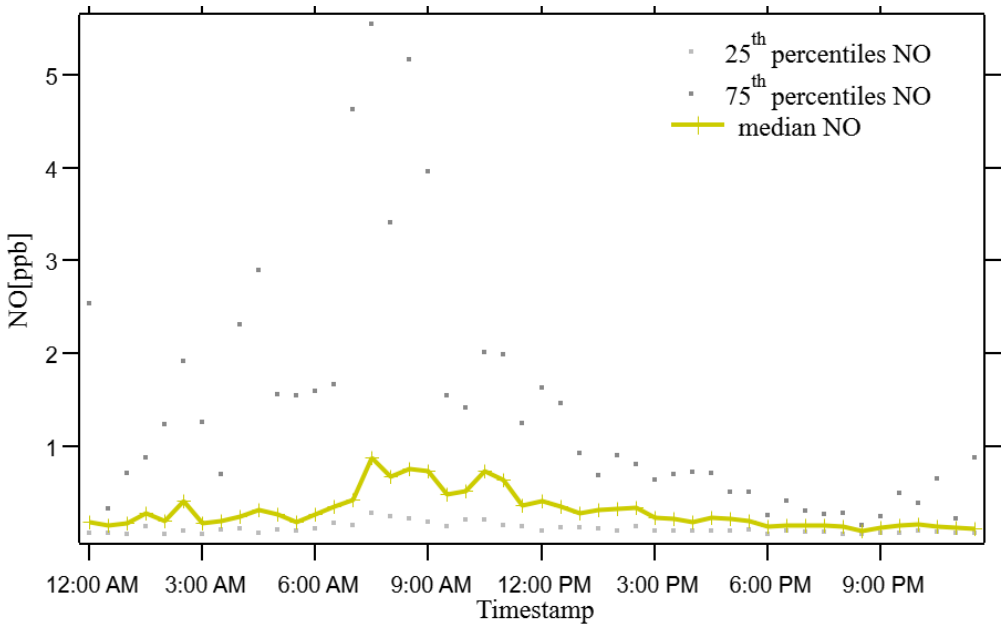

Figure 3.15 The diurnal cycle of NO mixing ratio based on July measurement at the Buffalo viewpoint Station (WBEA).

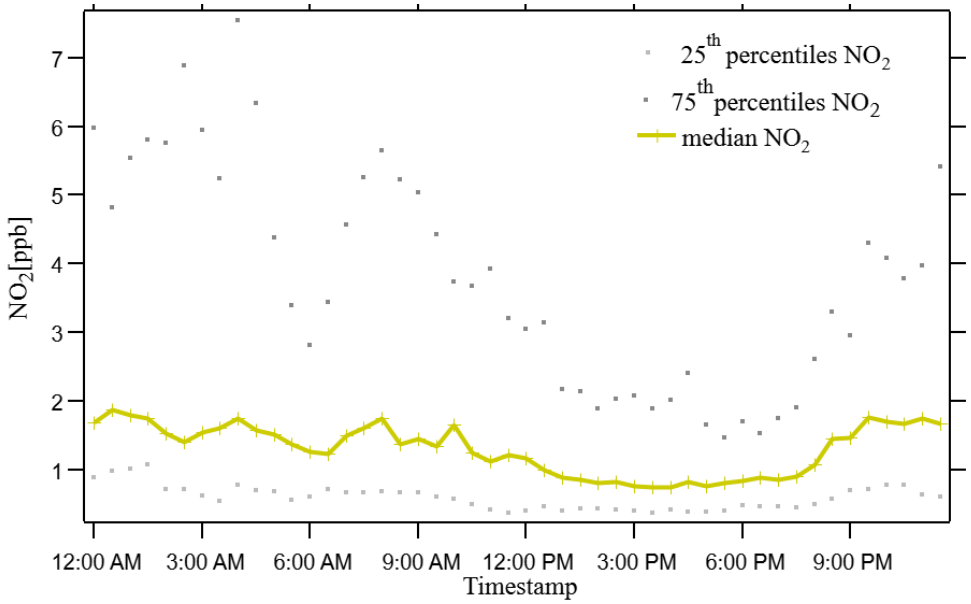

Figure 3.16 The diurnal cycle of NO_2 mixing ratio based on July measurement at the Buffalo viewpoint Station (WBEA).

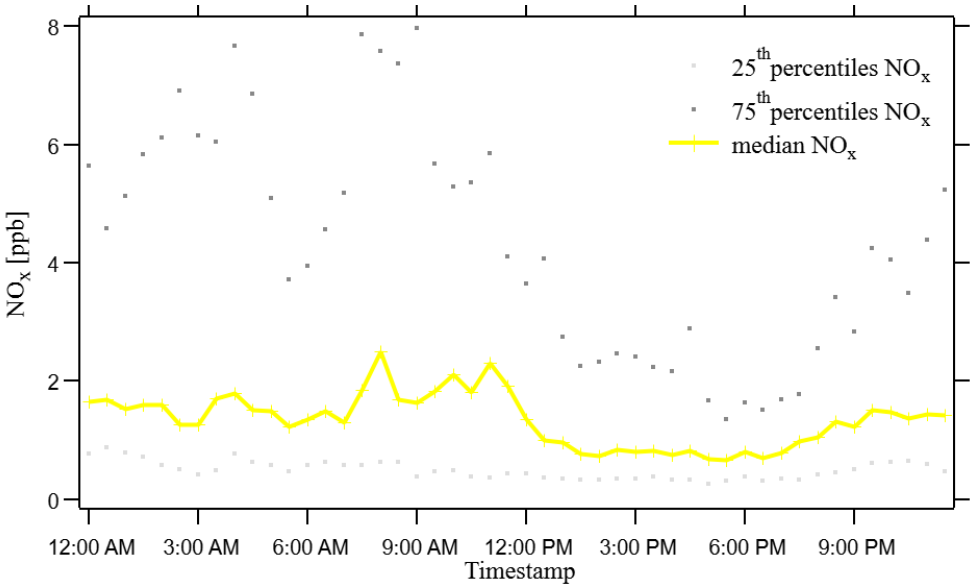

Figure 3.17 The diurnal cycle of NO_x mixing ratio based on July measurement at the Buffalo viewpoint Station (WBEA). The yellow line represents the median points of every 30 minutes measurements.

The diurnal cycle of ground ozone mixing ratio in 2017 and ground ozone mixing ratio in 2018 is shown in Figure 3.18. Both years' measurements were taken in that year's field study from the same 2B analyzer. The ozone mixing ratio in 2018 was lower than the measurement in 2017 in the YAJP forest. In the nighttime (from 11:00 pm to 4:00 am), the 2018 ozone mixing ratio was about 3 ppb lower than in 2017, but in the afternoon (from 3:00 pm to 11:00 pm), the difference between these two years' measurements was about 10 ppb. Both years reached the minimum at the same time (4:00 am) and both have the same recovery rate from 4:00 am to 11:00 am. However, after reaching the maximum, the ozone mixing ratio started decreasing in 2018 one hour earlier than in 2017. The daily maximum temperature in 2017 and 2018 in Fort McMurray was downloaded from Environment and Climate Change Canada website (2019), and the result shows that the average environmental temperature in 2018 field studies was about 16.9 ^{o}C, which is about 10 ^{o}C

lower than in 2017 field study. It is possible that the temperature difference caused the ground ozone mixing ratio in 2017 to be much higher than in 2018. However, temperature cannot directly affect ozone mixing ratio, the high temperature in 2017 may associated with high UV radiation at the ground level, less cloud cover, lower wind speed or lower NO_x emissions to cause more ozone formation and accumulation.

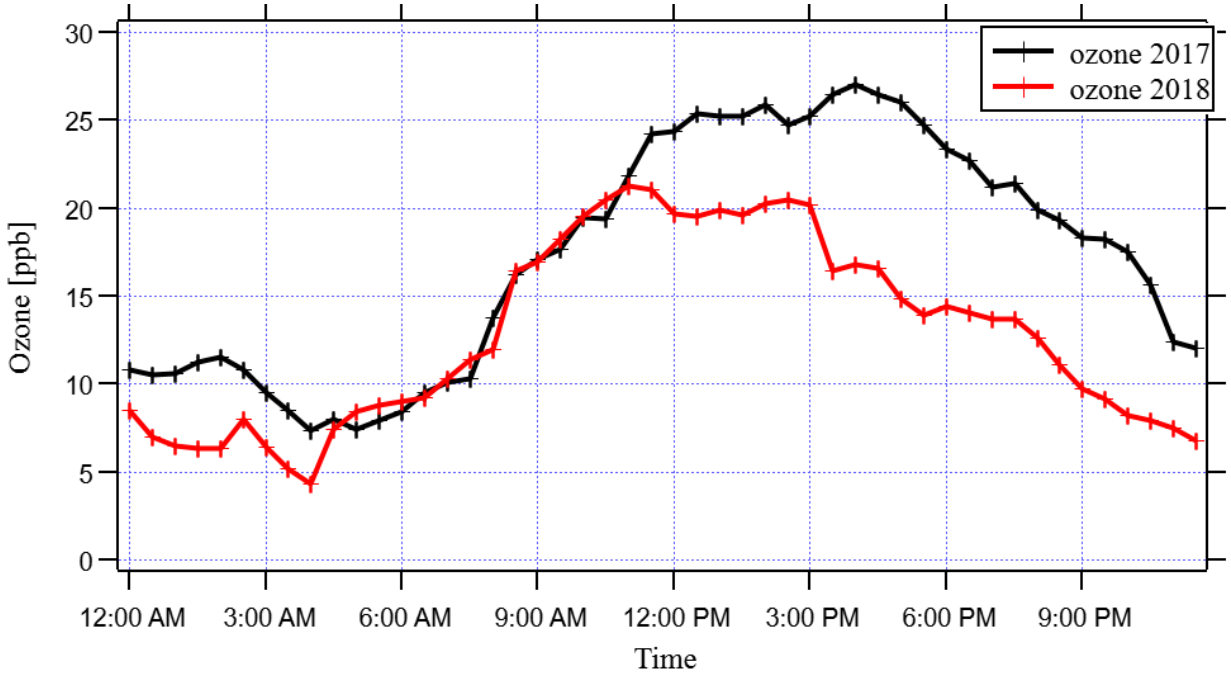

Figure 3.18 The comparison between ozone diurnal cycle measured in 2017 field study and 2018 field study at ground level.

3.5 Ozone vertical profiles

In the 2017 field study, the vertical variation of ozone and UV radiation were measured within the canopy in the YAJP forest by using the pulley system (Figure 2.3). At the same level, the higher UV radiation is usually associated with the higher ozone mixing ratio. The results are showing in Figure 3.19-3.23, The black lines represent the profile when the pulley system went upward, the red lines represents the profile when the pulley system

went downward. The overall trend of ozone was increasing with height when the UV radiation was also increasing with height, which is the same as Chen et al. (2017) analysis. The decrease of ozone mixing ratio from the canopy down to the ground can be explained by the ozone deposition from the stomatal uptake or chemical reactions (Chen et al., 2017; Finco et al., 2018). On each day, there was a peak of ozone mixing ratio within the canopy at a height of 4 m (figure 3.19-3.23). Finco et. al (2018) found that the ozone mixing ratio in the middle of the forest is about 2.5% higher than the ozone mixing ratio right above the canopy. In the afternoon, with UV radiation increasing, there was a slight increase of ozone mixing ratio. The result demonstrates the relationship of UV radiation to the ozone vertical variation based on the ozone photochemical reaction (R1.1).

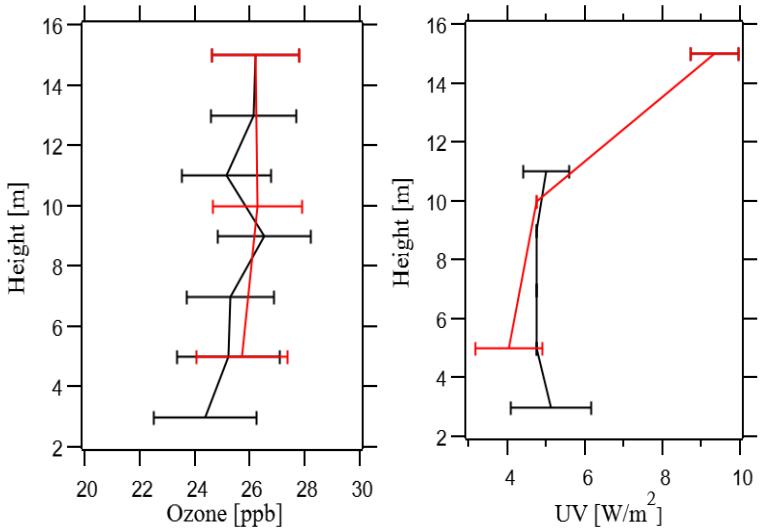

Figure 3.19 The comparison between Ozone vertical variation and UV radiation vertical variation within the YAJP forest (measured using the pulley system) on July 22, 2017 around 6:00 pm. The error bars are the standard deviations within 15 minutes measurement period.

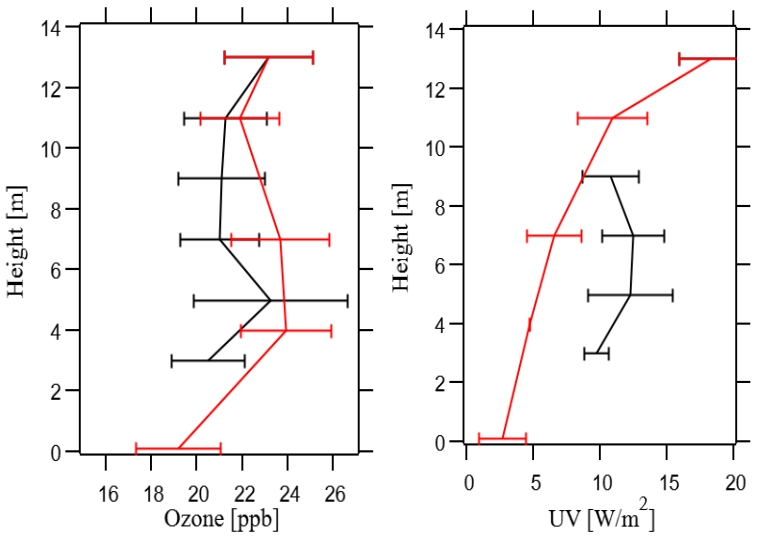

Figure 3.20 As Figure 3.19, for July 24, 2017 around 5:00 pm. The error bars are the standard deviations within 15 minutes measurement period.

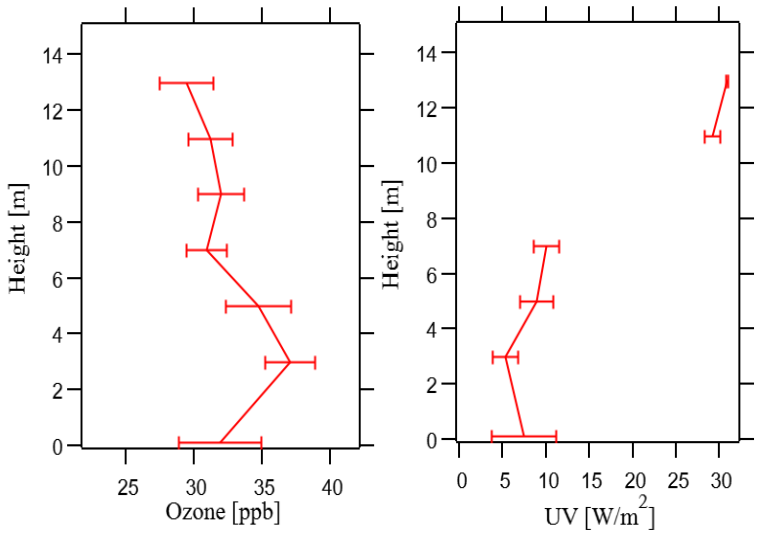

Figure 3.21 As Figure 3.19, for July 25, 2017 around 3:00 pm. The error bars are the standard deviations within 15 minutes measurement period.

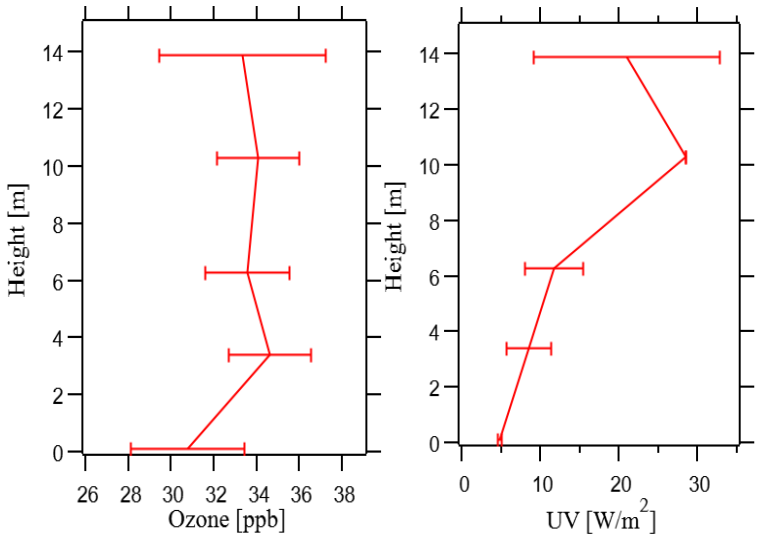

Figure 3.22 As Figure 3.19, for July 26, 2017 from 3:30 pm to 6:00 pm. The error bars are the standard deviations within 30 minutes measurement period.

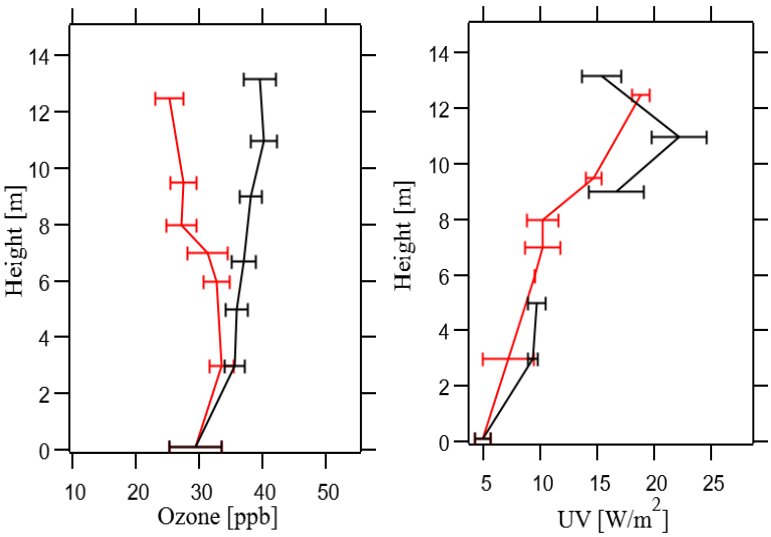

Figure 3.23 As Figure 3.19, for July 27, 2017 around 12:00 pm. The error bars are the standard deviations within 15 minutes measurement period

The ozone vertical profile measured by the Tethered-Balloon system in 2018 on three measurement days is shown in Figure 3.24-3.26. The measurement was up to a height of 300 m, each level shown in figures was taking average for 25 m intervals, and the error bar at each is the standard deviation. The results indicate that ozone mixing ratio increases with altitude by about 2 ppb from the ground up to 300 m. The positive ozone gradient can be explained by the ozone deposition. Air stagnation usually happened with low wind speed. Comparing the three days of ozone mixing ratios to the wind speeds, we found that for all these three days, lower wind speed associated with ozone accumulating in the forest, which cause an increase in ozone mixing ratio. However, when the wind speed is higher than 3 m/s, the increase of wind speed can dilute ozone in the clearing and decrease the ozone mixing ratio.

SO_2 is mainly released from the stack emission (Knabe, 1976). In the YAJP forest area, the detected SO_2 mixing ratio represents when there is a plume from surrounded oil facilities. Comparing O_3 mixing ratio vertical variation with SO_2 vertical variation, can determine how the pollution affect ozone gradients. On June 15 (Figure 3.25), from 75 m up to 300 m, the SO_2 mixing ratio varies around zero, while the O_3 mixing ratio vertical gradient was around 0.04 ppb/10 m; at 2:30 pm, the ozone mixing ratio is relatively high compare to the ozone aloft, this can be explained by an increase in SO_2 mixing ratio near a height of 50 75 m which causes and ozone mixing ratio increase (1.2 ppb/10 m), and then, from 75 m to 125 m, the SO_2 mixing ratio dropped down to 0, which also led to the ozone decrease to the same mixing ratio level on the ground. With nearly 0 ppb SO_2 mixing ratio from 125 m to 300 m, the ozone mixing ratio increasing rate dropped down to 0.1 ppb/10 m. The SO_2 mixing ratio on June 13 (Figure 3.24) at 11:00 am, June 15 at 12:30 pm and 1:00 pm

(Figure 3.25), June 16 at 5:00 pm (Figure 3.26) are nearly zero, which indicated there were low pollutant levels from the surrounded oil facilities. At these times, ozone mixing ratio increased constantly with smaller gradient (less than 0.2 ppb/10 m) compare to when the SO_2 was detected. The result indicates that oil sands facility combustion can enhance the ozone formation. This may be because with combustion, high SO_2 mixing ratios are related to high NO_x concentrations during the daytime. With photochemical reactions, more ozone is formed. In addition, with combustion, more ozone precursors can form NO_2 and lead to a higher ozone formation rate.

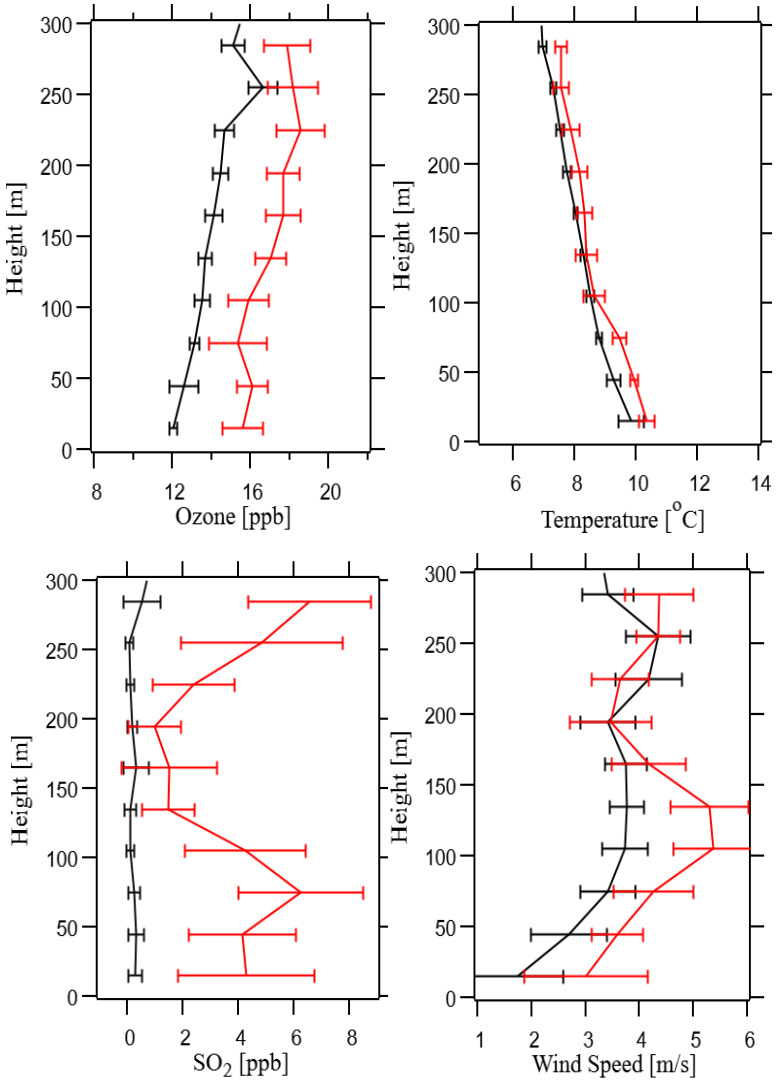

Figure 3.24 The comparison among Ozone mixing ratio, temperature, SO_2 mixing ratio and wind speed vertical variation up to 300 meters. The measurement was taken on June 13, 2018. The black line represents the measurement around 11:00 am and the red line represents the measurement around 1:00 pm.

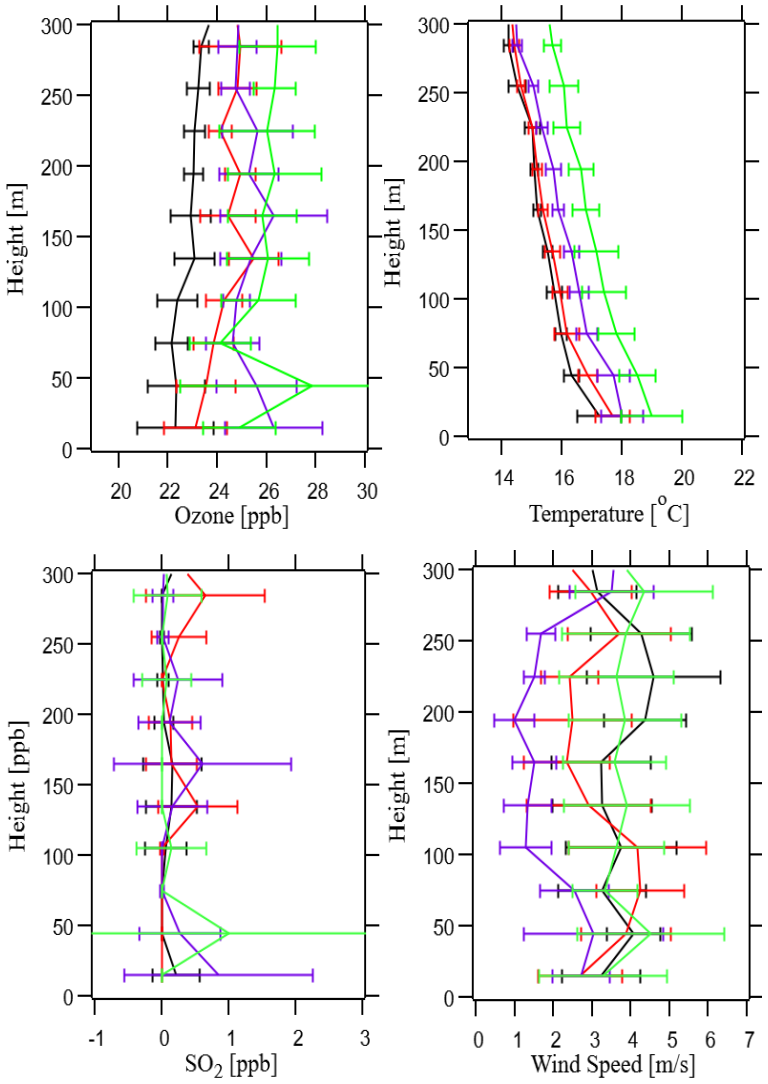

Figure 3.25 As Figure 3.24, the measurement was taken on June 15, 2018. The black line represents the measurement around 12:30 pm; the red line represents the measurement around 1:00 pm; the purple line represents the measurement around 1:30 pm and the green line represents the measurement around 2:30 pm.

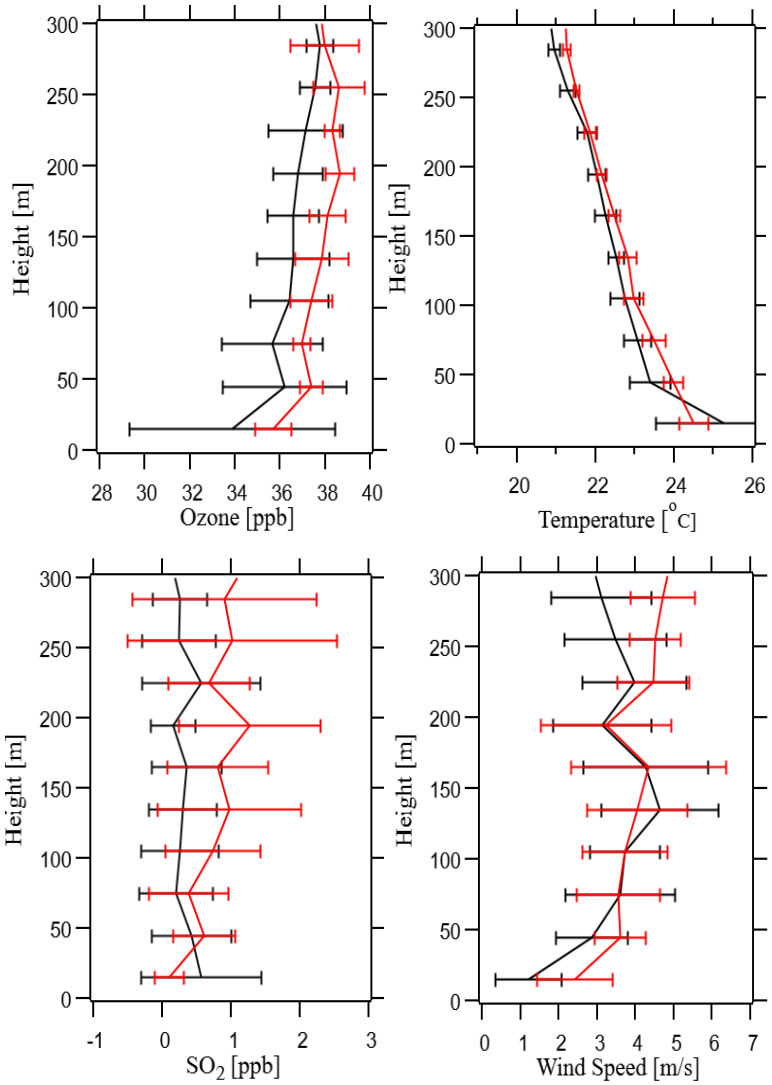

Figure 3.26 As Figure 3.24, the measurement was taken on June 16, 2018. The black line represents the measurement around 5:00 pm and the red line represents the measurement around 6:00 pm.

3.6 1-D canopy model

The simulated ozone mixing ratio from the 1-D canopy model is compared with ozone measurements to find out how accurate the 1-D canopy model is and if it can be used for future ozone prediction in the YAJP forest. With correct prediction, the 1-D canopy model can also provide the processes information, such as the amount of ozone formation due to chemical reaction and diffusion, and the ozone deposition rate. Based on the NO_x sensitivity test, the Buffalo viewpoint NO measurement results in the closest modelled ozone concentration to the YAJP ozone measurement. Therefore, the Buffalo viewpoint NO mixing ratio was used as the input for the 1-D canopy. However, there were several days negative points of NO mixing ratio. from June 15 to June 27, the average NO mixing ratio was about -1.3 ppb and the NO mixing ratio ranges from 0 to -2 ppb. Therefore, we have estimated there was about 2 ppb offset from the NO mixing ratio measurement. Because there was no NO mixing ratio measurement equipment correction shown in the WBEA website, and to avoid constant ozone mixing ratio output from 1-D canopy model, a 2 ppb correction has added to the Buffalo viewpoint measured NO mixing ratio. After the correction, all the NO mixing ratio less than 0 ppb were set as 0 for 1-D canopy model operation.

There were several runs of the 1-D canopy model. The Run 1 (Table 3.1) using constant 1 ppb NO mixing ratio input to output ozone mixing ratio as a reference shown in Figure 3.27. A 0 ppb NO mixing ratio was also used as input for the 1-D canopy model as the reference, and the result shown the output ozone mixing ratio from 1-D canopy model has no change from day and night. The Run 2 (Table 3.1) output of ozone chemical reaction

rate (f_{mn}) and diffusion rate ($\frac{\partial}{\partial z}\left(k(z_n)\frac{\partial C_{mn}}{\partial z}\right)$, from Eq. 2.11) at a height of 22 m (just above the canopy) are shown in Figure 3.28.

Table 3.1The comparison of four runs of 1-D canopy model with different NO, temperature, and pressure input, the GEM-MACH model ozone simulation and YAJP tower 2B measurement. The correlations of ozone mixing ratio were taken at a height of 22 m.

	NO input from	Temperature and pressure input from	*K* value input from	Other input from	correlation coefficient (r) between Run and 2B measurement ozone mixing ratio	correlation coefficient (r) between Run and GEM-MACH simulated ozone mixing ratio
Run 1	constant 1 ppb	YAJP measurement	GEM-MACH model	YAJP measurement	57.80%	N/A
Run 2	Buffalo viewpoint station with 2 ppb offset	YAJP measurement	GEM-MACH model	YAJP measurement	66.90%	N/A
Run 3	Fort McKay South station	YAJP measurement	GEM-MACH model	YAJP measurement	59.70%	N/A
Run 4	GEM-MACH model	GEM-MACH model	GEM-MACH model	YAJP measurement	49.30%	51.30%
GEM-MACH simulation	N/A	N/A	N/A	N/A	53.10%	N/A

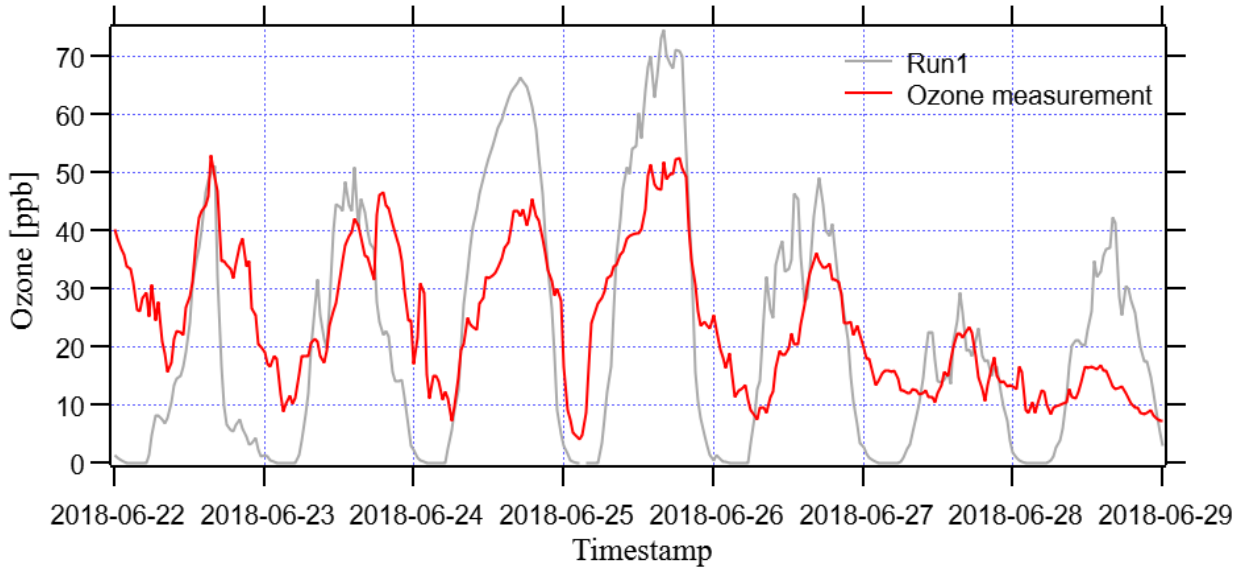

Figure 3.27 The comparison of Run 1 output at height 22 m and YAJP tower measured ozone mixing ratio

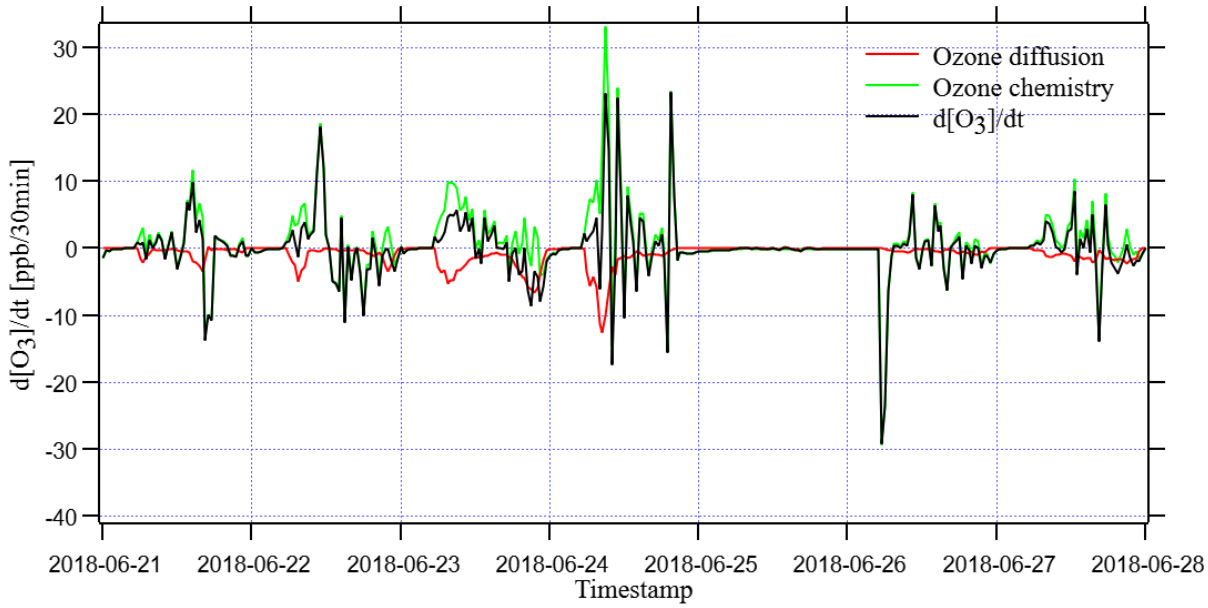

Figure 3.28 The comparison of the ozone diffusion rate (red), chemical reactions rate (green) and the rate of change of ozone (black) from Run 2 output with every 30 minutes at the height of 22 m.

The sum of the diffusion rate and chemical reaction rate represents the rate of change of ozone mixing ratio (dC/dt from Eq. 2.11). The results showed that the highest positive rate of change of ozone mixing ratio was near noon and the highest negative rate of change of ozone mixing ratio was in the evening. From June 25 around 9:00 pm to July 27 around 5:00 am, a technical issue led to an erroneous NO mixing ratio in the WBEA measurement instrumentation (such as the processes loading error, or the low battery mode happened). With zero NO mixing ratio input for the 1-D canopy model , the simulated NO_2 mixing ratio was close to zero, and there was neither ozone chemical reaction nor diffusion rate from 1-D canopy model simulation, which leads to a constant ozone mixing ratio. The ozone mixing ratio simulated by the 1-D canopy model was highly dependant on the input NO mixing ratio based on reaction R 1.1 and R 1.3. With zero NO mixing ratio, there is not any NO_2 in the atmosphere, which causes zero rate of change of ozone mixing ratio (ozone cannot be formed by NO_2 or removed by NO). With increased NO mixing ratio input, simulated NO_2 mixing ratio also increased, which decreased ozone mixing ratio (Figure 3.29). From Figure 3.29, the simulated ozone concentration shows a diurnal trend which is similar to the measurement. In addition, the 1-D canopy model simulated ozone was much lower than the ozone mixing ratio from measurement during the nighttime. With low k-value and low ozone precursors concentration during the nighttime, more ozone can be removed from the simulation and lead to the nighttime ozone near to zero.

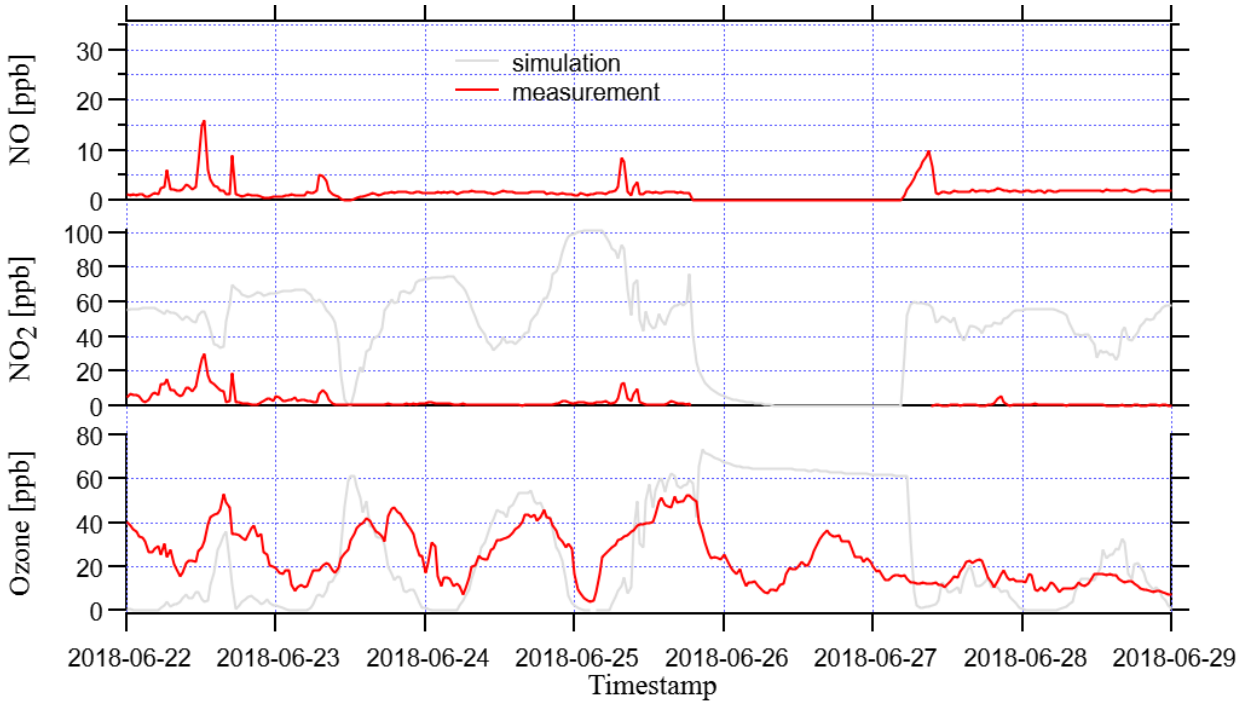

Figure 3.29 The comparison between the 1-D canopy model simulation and in situ measurement at the height of 22 m. red line represents the input used for Run 2 (WBEA, 2020). The grey line represents Run 2.

Ozone vertical variation from the 1-D canopy model simulation on June 24 is shown in Figure 3.30. During the daytime, there were only about 0.5% increase of ozone mixing ratio from the ground up to 50 m high. The ozone variation rate from the evening to the midnight has increased from the surface up to 25 m, such as at 11:00 pm, the ozone mixing ratio increased about 4 ppb from the surface to 25 m, and at 8:00 pm, the ozone mixing ratio only increased 2 ppb. Above 25 m, the ozone mixing ratio stays almost constant from the estimated measurement. The YAJP forest has a canopy height around 19 m. The results indicated that with 1-D canopy model simulation, ozone mixing ratio increased with height within the canopy, but there were not much gradient differences above the canopy (see details in section 3.9).

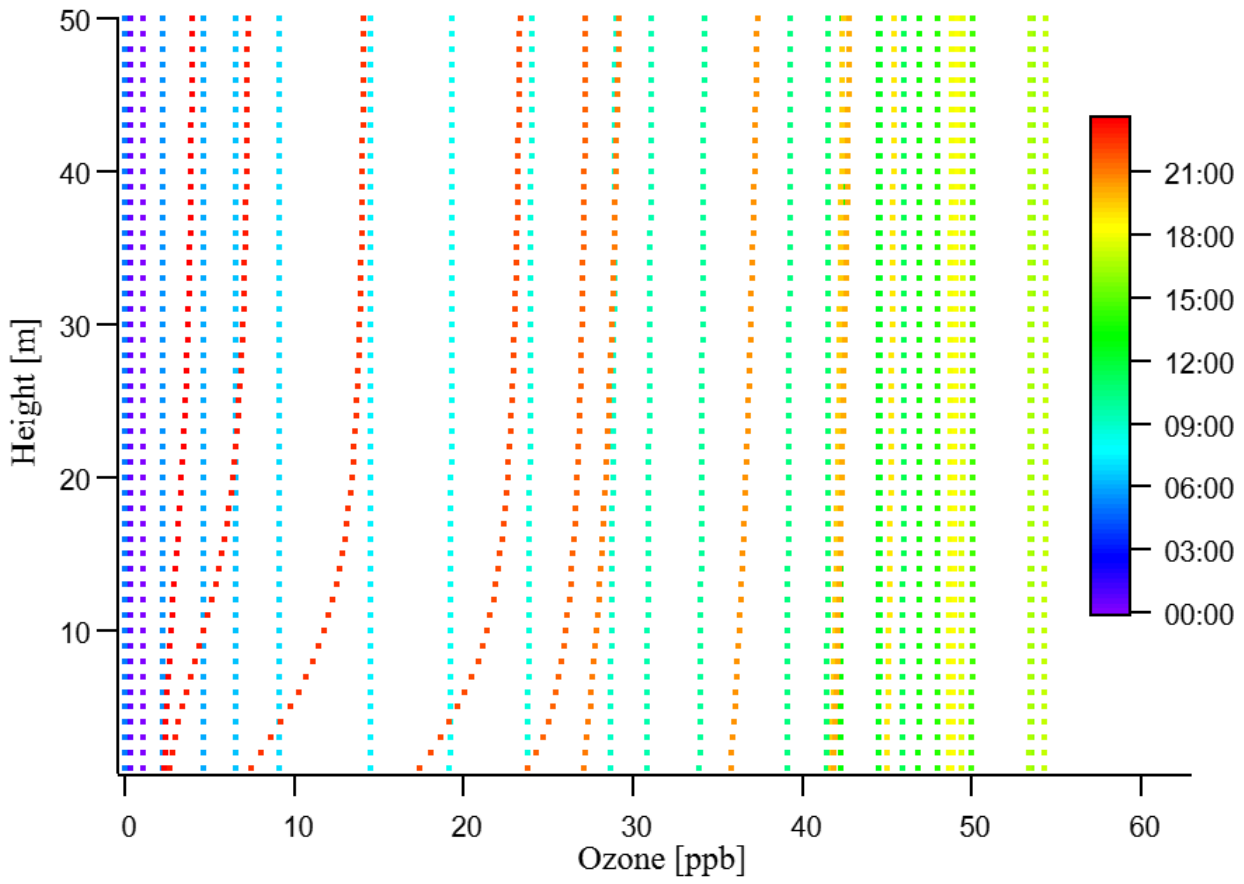

Figure 3.30 Ozone vertical variation on June 24 based on the 1-D canopy model simulation. The color scale represents every 30 min simulation from 12:00 am to 11:30 pm.

3.7 GEM-MACH model

The ozone vertical variations simulated by the GEM-MACH model from the ground up to 300 meters on June 13, 15, and 16 were used to compare with the tethered-Balloon system measurement (Figure 3.24-3.26). The result showed that in the GEM-MACH model simulation, there was no ozone variation from the ground to near 20 m. The general trend of ozone mixing ratio is increasing with height, which is similar to the measurement. Both the simulation and measurement have a rapid increase with altitude on June 13 and a gentle

increase with altitude on June 15. On June 13, the measurement ozone variation was about 0.1 ppb/10 m, and the simulation was about 0.05 ppb/10 m. However, On June 15, the measurement ozone vertical variation was about 0.03 ppb/10 m, and the simulation was about 0.017 ppb/10 m. On June 13, the difference between ozone measurement at 11:00 am and 1:00 pm was about 2 ppb, which is the same as the simulation. This also happened on June 16. On June 15, the difference between ozone measurement at 12:30 pm and 1:00 pm was about 1.5 ppb, which is the same as the simulation. The difference from measurement at 1:00 pm, 1:30 pm, and 2:30 pm on June 15 was different from the simulation, and the measurement was less. The simulated NO mixing ratio seems to have no effect on ozone vertical variation which had no change from the near surface (20 m) up to 300 m. On June 16, the decreasing NO_2 mixing ratio from the near surface up to 300 m may be the reason that ozone mixing ratio has no variation from 70 m up to 300 m. This is because ozone can be formed by the photochemical reactions (R 1.1 & R 1.2), and the UV radiation comes from aloft.

The temperature had a rapid decrease from the ground up to near 20 m (about 0.75 ^{o}C/10 m), and then the decrease was smaller from near 20 m up to 300 m (about 0.08 ^{o}C/ 10 m). By comparing the GEM-MACH simulated temperature to the measured temperature, there is an about 2 ^{o}C underestimation of approximately 2 ^{o}C in the GEM-MACH model.

By comparing the simulated ozone from the GEM-MACH model with measured ozone mixing ratio (Figure 3.31-3.32), there was an overprediction of around 10 ppb of ozone mixing ratio from GEM-MACH, but the variation trend of ozone simulation from the GEM-MACH model and the ozone measurements were similar.

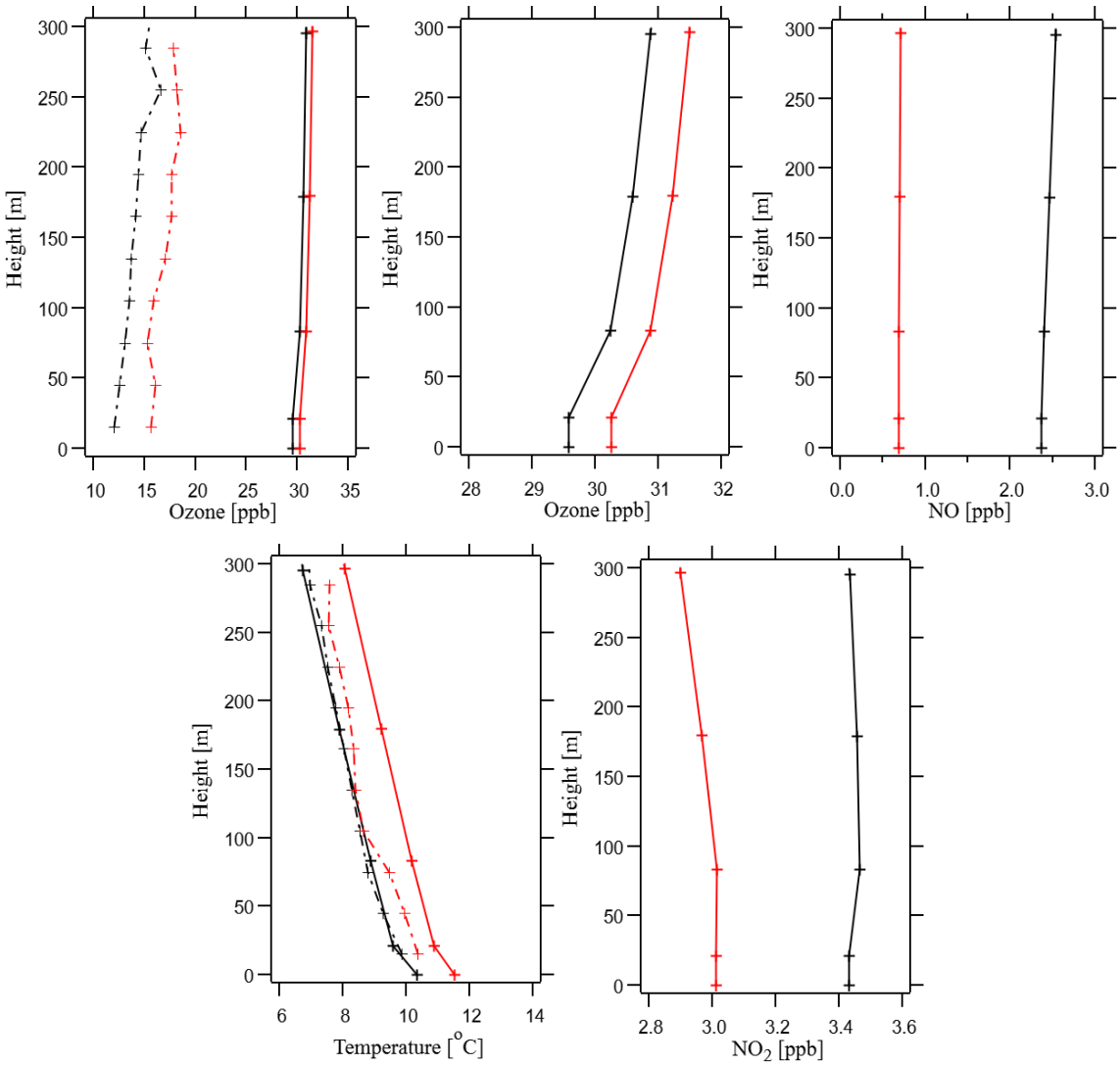

Figure 3.31 Vertical variation from GEM-MACH model simulation (solid lines). The dash line represents the measurement from Tether-Balloon system on June 13. The black line is from 11:30 am and the red line is at 1:00 pm.

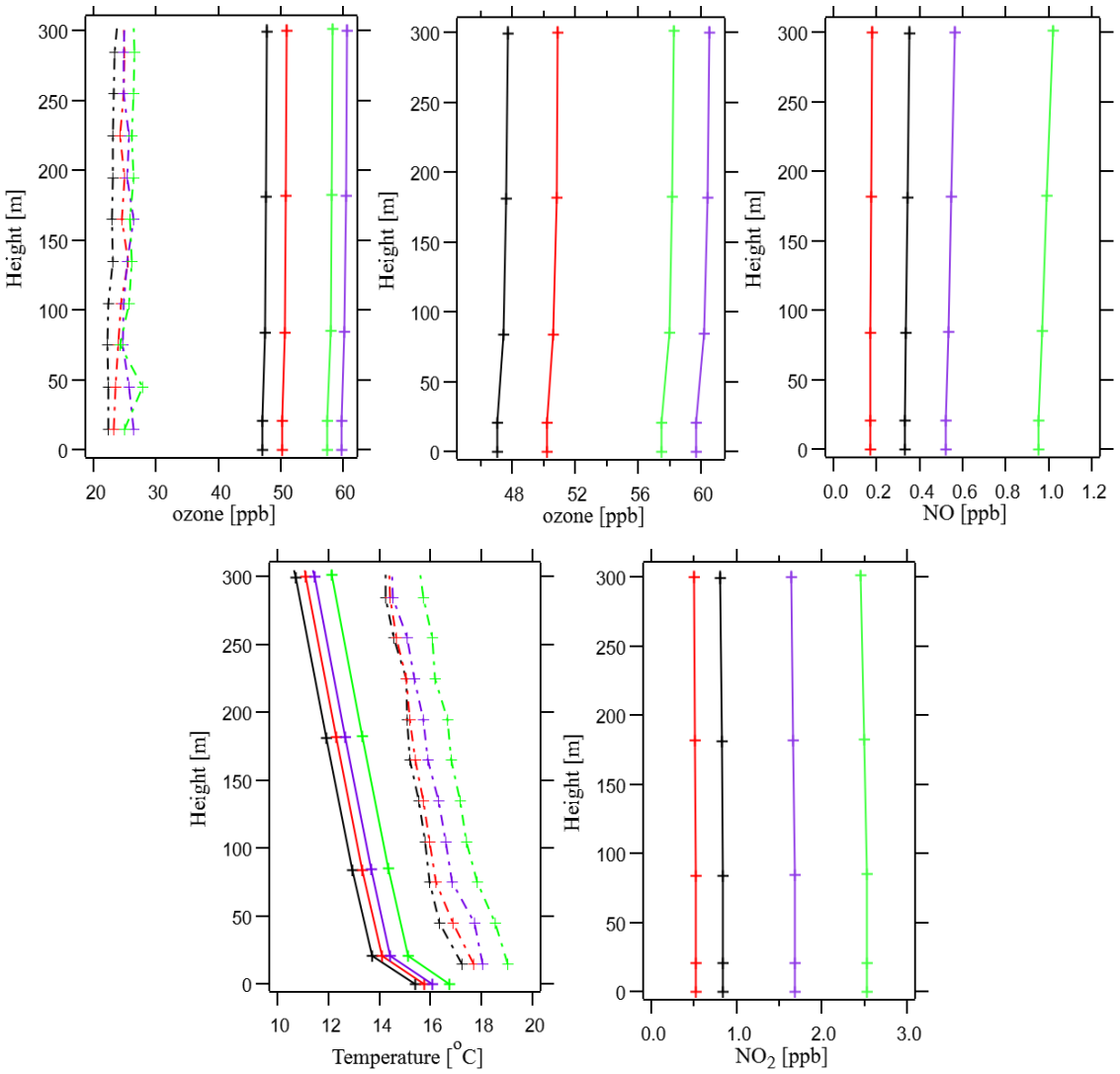

Figure 3.32 As Figure 3.31. The dash line represents the measurement from Tether-Balloon system on June 15. The black line is at 12:30 pm, red line is at 1:00 pm, the purple line is at 1:30 pm and the green line is at 2:30 pm.

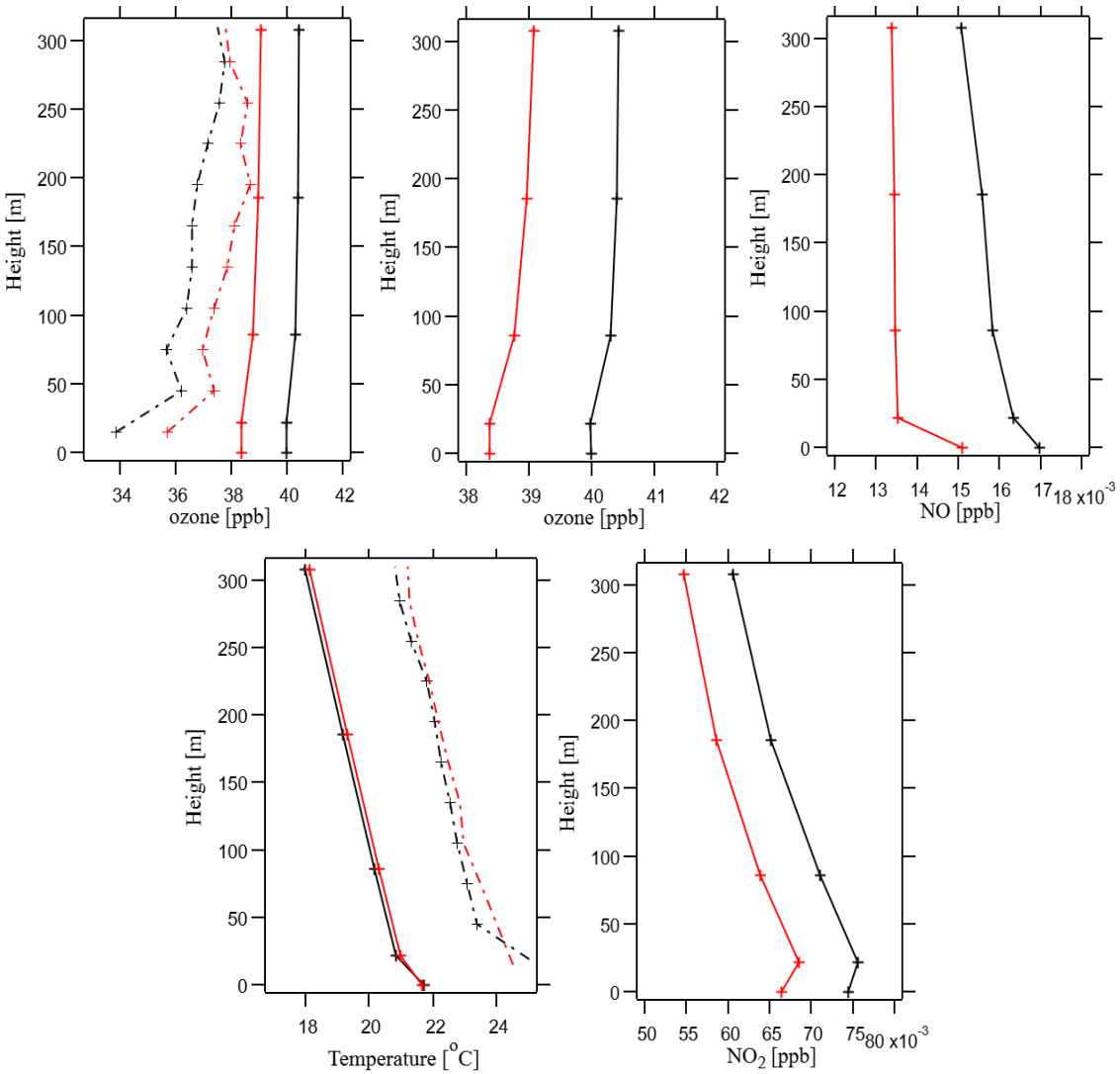

Figure 3.33 As Figure 3.31. The dash line represents the measurement from Tether-Balloon system on June 16. The black line is at 5:30 pm, red line at 6:00 pm.

3.8 Modelling comparison

The NO and temperature from GEM-MACH model simulations were used as the 1-D canopy model input to find how the 1-D canopy ozone simulation compares to the GEM-MACH model. The result of 1-D canopy model output and GEM-MACH model simulation are shown in Figure 3.34. The result indicated that the 1-D canopy model simulated ozone was lower than the GEM-MACH modeled ozone, and closer to the *in situ* measurement at the YAJP tower. In addition, using the GEM-MACH model simulated NO mixing ratio, the 1-D canopy model overpredicted the NO_2 mixing ratio. Our results suggest that by using the GEM-MACH model simulated NO mixing ratio and temperature as input (Run 4), the 1-D canopy model gives a better result for the ozone mixing ratio compare to the GEM-MACH model. The correlation of ozone mixing ratio between four runs and YAJP ozone mixing ratio are shown in Table 3.1. The data from June 25 to June 26 has been removed for Run 2 (see details in section 3.6). The difference between these measured or simulated ozone mixing ratios are shown in Figure 3.35. The result indicated that the 1-D canopy model better simulated ozone mixing ratio than the GEM- MACH model (either using the Buffalo viewpoint NO mixing ratio (Run 2) or using the GEM-MACH simulated NO mixing ratio (Run 4)). The bias (relative to the 2B measured ozone mixing ratio) of the 1-D canopy model is lower than the bias of the GEM-MACH model simulated ozone to the 2B measured ozone mixing ratio. The average difference between the Run 2 and 2B measurement is about -3.6 ppb; about 6.3 ppb between Run 4 and 2B measurement. However, the average difference is about 11.5 ppb between the GEM-MACH simulation and 2B measurement.

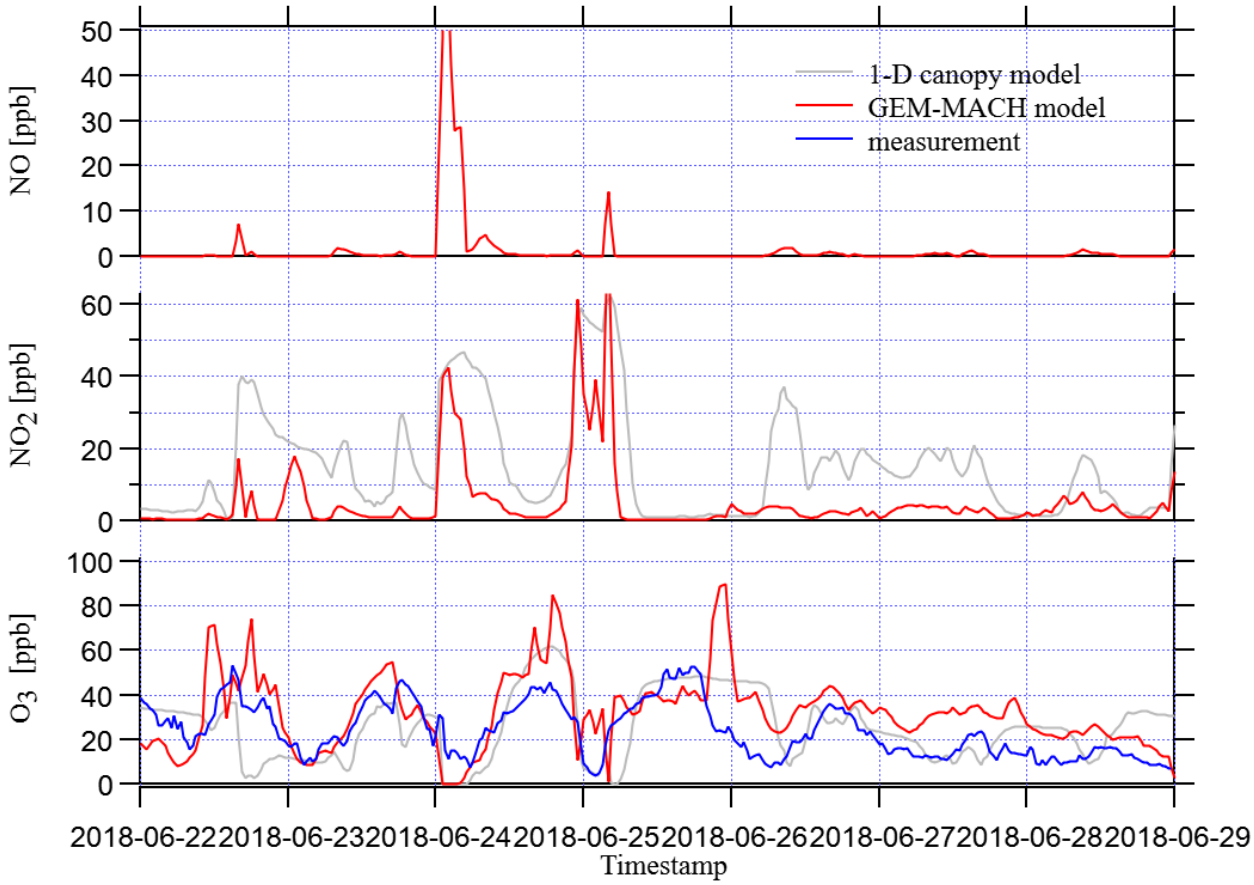

Figure 3.34 The comparison among the 1-D canopy model simulation, the GEM-MACH model simulation and ozone measurement from 2B ozone analyzer at the height of 22. red line represents ozone simulation from GEM-MACH model at YAJP tower; the grey line represents the simulation from 1-D canopy model with using NO mixing ratio and temperature from GEM-MACH model simulation; the purple line represents the 2B measurement at YAJP tower.

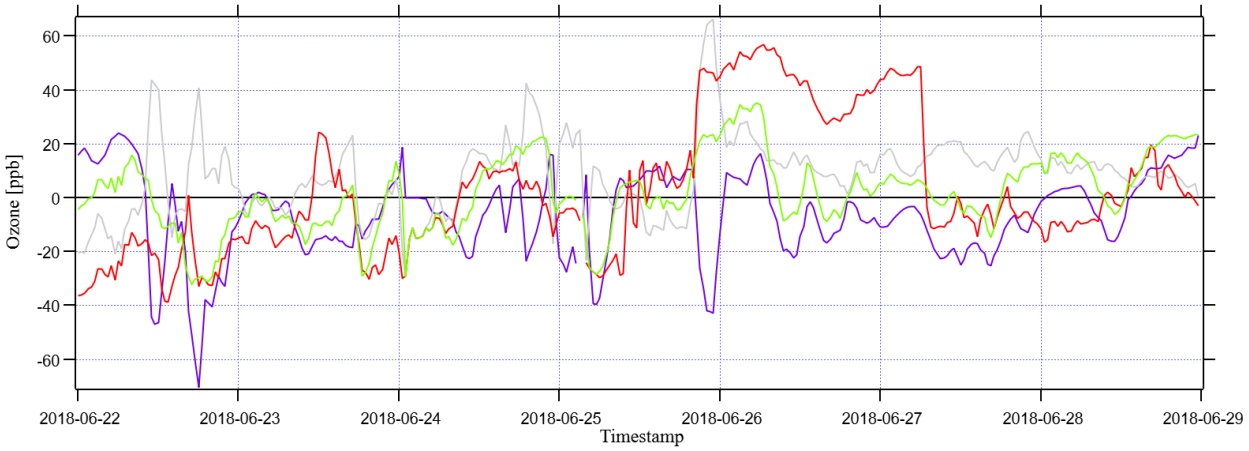

Figure 3.35 The difference between Run 4 and 2B ozone analyzer measured ozone mixing ratio (green line); Run 4 and GEM-MACH model simulated ozone mixing ratio (purple line); Run 2 and 2B ozone analyzer measured ozone mixing ratio (gray line); the GEM-MACH model simulated ozone mixing ratio and 2B ozone analyzer measured ozone mixing ratio (red line).

3.9 Ozone deposition from modelling

Based on Figure 3.30, the 1-D canopy model seems does not have a strong ozone deposition gradient with height. In order to investigate the gradient differences between the measurements, the GEM-MACH model, and the 1-D canopy model, the ozone deposition analysis within the canopy was required. Making the assumption to ignore the chemistry, the ozone deposition flux (F) can be calculated as

$$F = -K\frac{dC}{dz}, \qquad 3.1$$

where C is the ozone concentration, which was converted from ppb to μmol/m^3 for the calculation.

The deposition velocity can be calculated as

$$v_d = -\frac{F}{C}. \qquad 3.2$$

The diurnal cycle of median ozone deposition flux from the GEM-MACH model is shown in Figure 3.36. The result indicates that ozone deposition flux was almost always negative, and the high ozone deposition occurred during the daytime. The GEM-MACH model simulation of ozone deposition flux agreed with Finco et al. (2018) that ozone deposition flux increased with the height from 6 m to 22 m.

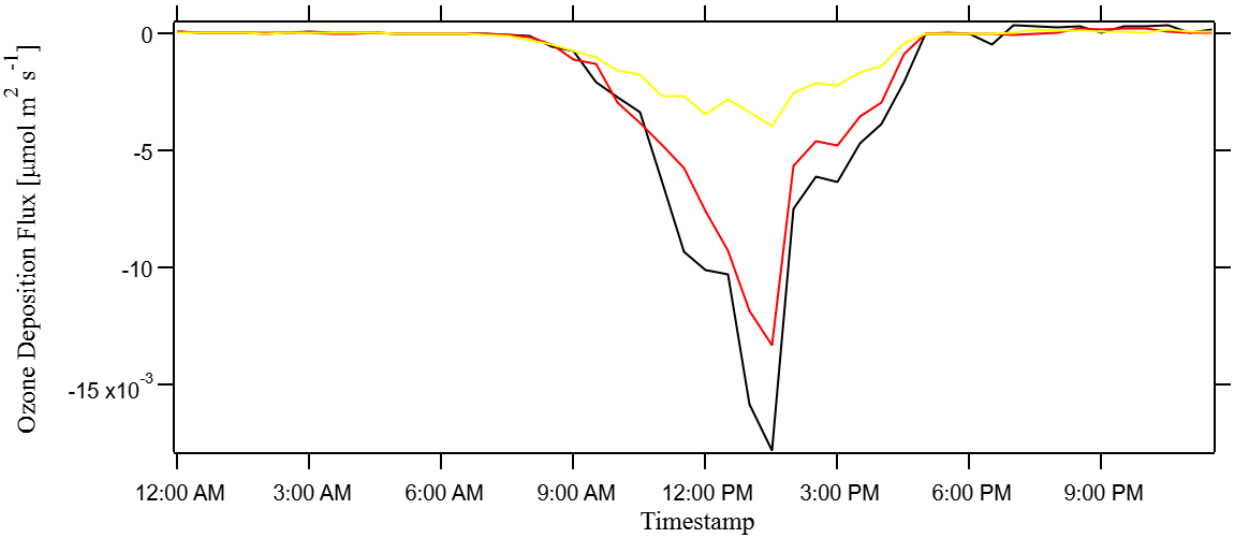

Figure 3.36 The diurnal cycle of ozone deposition flux from GEM-MACH model. The black color indicated deposition flux at 22 m, red color is at 16 m and yellow color is at 6 m.

The deposition rate from Run 4 and the GEM-MACH model are shown in Figure 3.37. The results show that the deposition rate was the same at all levels from the simulation. Because the Run 2 and Run 3 used constant temperature and NO mixing ratio with height, there was no ozone gradient or the deposition flux. Therefore, to calculate the ozone gradient from the 1-D canopy model and find out how much of the gradient is due to the chemistry process and deposition, Run 4 was used to do the analysis. Table 3.2 shows the

comparison of ozone gradient at 5 m, 10 m, and 14 m from Run 4 and ozone profile measurement in 2017. The ozone gradient measured in 2017 was much higher than the ozone profile simulated from Run 4. Due to the 1-D canopy model simulation equation (eq. 2.11), the ozone variation was simulated based on the emission, chemical reaction and deposition. There aren't any ozone emissions in the forest, which indicated that the simulated ozone variation in the 1-D canopy model was only affected by the chemical reaction and deposition. Without including the deposition in the 1-D canopy model simulation, the ozone vertical variation only depends on chemical reactions and becomes much smaller from the ground up to 50 m (Run 4). The measurement of ozone variation includes both chemical reactions and deposition. Therefore, by comparing the Run 4 and ozone gradient measurement (table 3.2), we can find the gradient percentage due to deposition and chemistry. The results indicate the gradient due to deposition ($\frac{\frac{dC_{real}}{dz}-\frac{dC_{R4}}{dz}}{\frac{dC_{R4}}{dz}}$) was about 100 times higher than the gradient due to chemistry ($\frac{dC_{R4}}{dz}$). Because the gradient due to chemistry was much smaller than the gradient due to deposition, when calculating ozone deposition flux and deposition velocity, the chemistry effect can be ignored.

By comparing the ozone gradient from the Tethered Balloon system and the GEM-MACH model (Figure 3.31-3.33), the average ozone gradient from the ground up to 300 m due to the Tethered-Balloon system measurement (7.22E-3 ppb/m) was a little higher than the ozone gradient from GEM-MACH (2.45E-3 ppb/m). One possible reason is that the GEM-MACH model didn't include the surrounding oil facilities' plume effect. Figure 3.31-3.33 shows that the ozone mixing ratio variation and SO_2 mixing ratio variation were similar (see details in section 3.5), which may cause the Tethered-Balloon system ozone gradient

to be higher than the GEM-MACH model. Another possible reason is the canopy effect wasn't included in the GEM-MACH model simulation. Without the canopy effect, the GEM-MACH can overestimate the ozone mixing ratio (Makar et al., 2016). Without UV attenuation from above the canopy down to the surface, the ozone mixing ratio at the ground level was more overpredict than the upper level, and this can cause the ozone gradient from the GEM-MACH model was less than the measurement

The ozone mixing ratio measured from 2017 field study had the ozone profile measurement, which will be used to calculate the ozone gradient (table 3.2). The eddy diffusivity from the 2017 field study can be calculated as

$$K = \kappa u_* (z + z_{02}), \tag{3.3}$$

Where k is Von Karman constant and κ = 0.4, u_* is the friction velocity and can be calculated as

$$u_* = \sqrt[4]{(\overline{u'w'})^2 + (\overline{v'w'})^2}, \tag{3.4}$$

and equation 3.1 to 3.4 are used to calculate ozone deposition rate.

Table 3.2 The ozone gradient comparison between the measurement in 2017 and Run 4 simulation

time	ozone gradient from Run 4 $\frac{dC_{R4}}{dz}$ at 5 m (ppb/m)	ozone gradient from measurement $\frac{dC_{real}}{dz}$ at 5 m (ppb/m)	ozone gradient from Run 4 $\frac{dC_{R4}}{dz}$ at 10 m (ppb/m)	ozone gradient from measurement $\frac{dC_{real}}{dz}$ at 10 m (ppb/m)	ozone gradient from Run 4 $\frac{dC_{R4}}{dz}$ at 14 m (ppb/m)	ozone gradient from measurement $\frac{dC_{real}}{dz}$ at 14 m (ppb/m)
12:30:00	3.83E-03	6.35E-01	3.84E-03		3.86E-03	
13:00:00	5.64E-03		3.51E-03	1.04E+00	6.54E-03	
14:00:00	3.77E-03	1.01E-01	3.77E-03		5.06E-03	
14:30:00	3.70E-03		3.71E-03	1.56E+00	4.78E-03	3.74E-02
15:30:00	2.33E-03	1.32E-02	2.33E-03		3.57E-03	
18:00:00	0.00E+00	4.20E-01	0.00E+00		3.65E-04	
18:30:00	1.55E-04		1.55E-04	5.60E-01	2.10E-04	4.52E-02

Comparing the ozone deposition velocity calculated from GEM-MACH model and 2017 pulley 2B measurement, the highest deposition rate happened in the noon around 12:00 pm. Both measured 2017 pulley ozone deposition rate and simulated ozone have peaked at around 2 pm, then dropped down at around 3 pm. At 4 pm, the ozone deposition rate reached a peak again. After 5 pm, the ozone deposition rate calculated from both simulation and measurement dropped down. However, the overall ozone deposition rate calculated from the measurement was higher than the simulation. This is maybe because the ozone deposition rate was calculated based on the *K* value, ozone gradient and ozone mixing ratio. The ozone gradient from measurements was much higher than from the simulation, but the simulation overestimated the ozone mixing ratio. Based on equation 3.1-3.2, the high ozone gradient and low ozone mixing ratio lead to the ozone deposition rate from measurement was higher than the simulation. The measured maximum ozone deposition rate is around 20 mm/s and the simulated maximum ozone deposition rate is

around 13 mm/s. Compare to previous studies, in the boreal forest, the daily maximum usually within the range between 2.5 mm/s to 20 mm/s (Finkelstein et al., 2000). However, due to the lack of wind data, there is no evidence to show if the high ozone deposition rate from the measurement is due to the oil combustion pollutions.

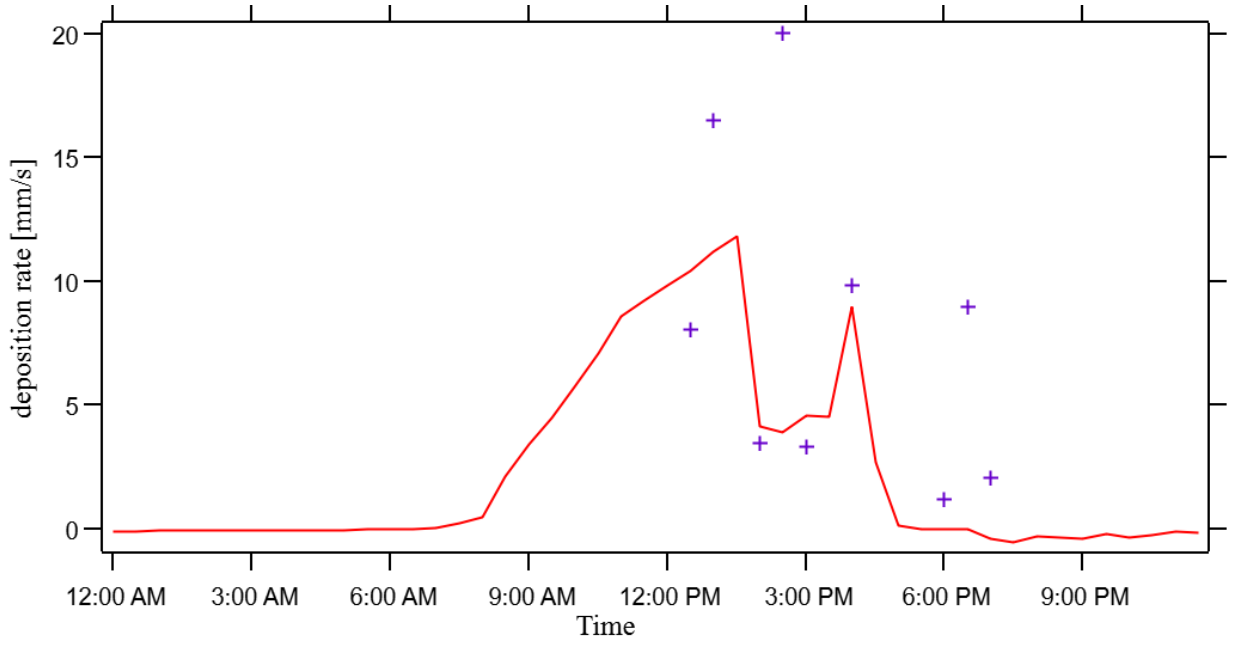

Figure 3.37 The diurnal cycle of ozone deposition rate from GEM-MACH model (red line). The purple marker is the average ozone deposition rate from 2017 pulley 2B measurement at each time spot.

4. Conclusion

The Gaussian plume model indicated the measured pollution in the YAJP forest was mainly from the Suncor oil facility. Our measurements suggested that the plume can enhance the ozone mixing ratio in the downwind area mainly in the afternoon. The enhancement happened when the temperature was over 20 ^{o}C and wind speed was lower than 3 m/s. The average daily enhancement was about 15% (about 4 ppb) and from 4 pm to 4 am, the enhancement was about 20% (6 ppb) in the downwind area. However, the enhancement is quite small and can be considered negligible relative to the daily variation. In Aggarwal et al. (2018) there were no evidence to show that the plume from oil sand facilities can enhance the ozone mixing ratio in the forest. Cho et al. (2017) also mentioned that in the oil sands region, the high NO_x mixing ratio produced by the plume can't enhance the ozone mixing ratio in the long-term monitoring due to the NO titration.

The ozone mixing ratio measured by the pulley system from YAJP tower in 2017 indicated that the overall trend of ozone mixing ratio increased with height within the forest canopy, and UV radiation also played an important role in the ozone vertical variation due to the ozone photochemical reaction. In 2018, the ozone vertical variation was measured by the Tethered – Balloon system from the surface up to a height of 300 m. Deposition is an important ozone removal process, which causes the ozone mixing ratio to increase with height.

The low wind speed (less than 3 m/s) can enhance the ozone mixing ratio, due to ozone accumulation. The high wind speed (more than 3 m/s) can dilute the ozone to decrease the ozone mixing ratio. However, the result is different from Chen et al. (2018) in that they

found the low wind speed causes low ozone mixing ratio. This difference may be because in their study, the pollution was from surrounding cities, which were quite far from the forest (about 50 km). With low wind speed, the pollution won't reach the forest and cause a low ozone mixing ratio.

The ozone vertical variation had a similar tendency as the SO_2 vertical variation. The forest vegetation doesn't produce SO_2 by its own, and the detected SO_2 mixing ratio was mainly from the surrounding oil facilities. The plume can produce VOCs, which react with NO_x to form more ozone. Using the long-term measurements in 2018, we found that the temperature and UV radiation were positively correlated to the ozone mixing ratio, which is the same as previous studies (Stathopoulou et al., 2008; Robert et al. 2017; Kavassalis, S. C., & Murphy, J. G. 2017). From the ozone formation reactions (R1.1&R1.2), with more UV radiation, more NO_2 can be decomposed to form oxygen atoms, which is the reactant to form ozone. The correlation of temperature and ozone can be explained by UV radiation or ozone precursors. High UV radiation is usually associated with high temperature, and the increased temperature may can accelerate some of the ozone precursor formation reactions. Therefore, the temperature demonstrates a positive correlation with ozone mixing ratio. Wind speed is highly correlated to the ozone mixing ratio with either temperature less than 20 ^{o}C or relative humidity lower than 30%. Our results support the Aggarwal et al (2018) argument that the enhancement usually happens with high temperature and air stagnation.

The 1-D canopy model simulated ozone mixing ratio agreed with the 2B measurements and the average difference is -3.5 ppb. However, the GEM-MACH model showed a large bias compared to the measured ozone mixing ratio with an average difference of about 11.4 ppb.

Makar et al (2016) demonstrated that within the forest, the canopy shading accounts for 30% of ozone reduction, Therefore, it is possible that the reaction of ozone mixing overpredicted from GEM-MACH model is because the canopy effect is not included in the version of the GEM-MACH model.

Based on the deposition analysis, the GAM-MACH simulation showed the ozone deposition flux increased with the height from 6 m to 22 m, which is agreed with previous studies (Finco et al., 2018). By comparing the ozone gradient from Run 4 and measurement, we found that within the canopy, only about 0.004 ppb/m gradient was due to the chemistry and about 0.4 ppb/m gradient was due to the deposition. Thus, the chemistry effect to the gradient can be ignored when calculating the ozone deposition.

The ozone deposition velocity measured from 2017 pulley system doesn't demonstrate if there is a clear diurnal cycle because of data deficiencies. The deposition velocity from the measurement was similar to the simulation. For future studies, more ozone profile data and meteorological data can be measured and used for ozone deposition rate analysis. The NO mixing ratio can be measured at the YAJP tower simultaneously with the ozone mixing ratio to optimize the 1-D canopy model simulation for the ozone mixing ratio. NO mixing ratio and temperature measured a multiple heights at the YAJP tower could help us to determine if these two factors can affect 1-D canopy model simulation of the ozone deposition rate within the canopy, and also help us to compare the 1-D canopy model with measured ozone mixing ratio profile.

Reference

2B Technologies, Inc. (2017) Ozone Monitor Dual Beam. *Operation Manual*.

Abdullah, A. M., Ismail, M., Yuen, F. S., Abdullah, S., & Elhadi, R. (2017). The Relationship between Daily MaximumTemperature and Daily Maximum Ground LevelOzone Concentration. *Polish Journal of Environmental Studies, 26*(2), 517-523. doi:10.15244/pjoes/65366

Aggarwal, M., Whiteway, J., Seabrook, J., Gray, L., Strawbridge, K., Liu, P., … Mclaren, R. (2018). Airborne lidar measurements of aerosol and ozone above the Canadian oil sands region. *Atmospheric Measurement Techniques*, *11*(6), 3829–3849. doi: 10.5194/amt-11-3829-2018

Allison, E., & Mandler, B. (2018). Air Quality Impacts of Oil and Gas Emissions from Production, Processing, Refining, and Use. *Petroleum and the Environment*.

Anselmo, D., Moran, M. D., Ménard, S., Bouchet, V. S., Makar, P. A., Gong, W., . . . Talbot, D. (2010). A New Canadian Air Quality Forecast Model: GEM-MACH15. *12th Conference on Atmospheric Chemistry*.

Beecken, J., Mellqvist, J., & Salo, K. (2014) Airborne emission measurements of SO2, NOx and particles from individual ships using a sniffer technique. *Atmospheric Measurement Techniques, 7(7),* 1957-1968. Doi: 10.5194/amt-7-1957-2014

Bilodeau, S. E., Wu, B.-S., Rufyikiri, A.-S., Macpherson, S., & Lefsrud, M. (2019). An Update on Plant Photobiology and Implications for Cannabis Production. *Frontiers in Plant Science, 10*. doi: 10.3389/fpls.2019.00296

Bourque, C., & Hassan, Q. (2010). *Field Verification of Modis-Based Leaf Area Index for the Greater Athabasca Oil Sand Region of Northern Alberta, Canada* (Rep.). Cumulative Environmental Management Association.

Briggs, G. (1973). Diffusion estimation for small emissions. Preliminary report. doi: 10.2172/5118833

Burba, G., & Anderson, D. (2010). *A brief practical guide to Eddy Covariance Flux Measurements: principles and workflow examples for scientific and industrial applications: version 1.0.1*. Lincoln, NE: LI-COR Biosciences.

CAPP (2018). Canada's Oil Sands Report. *Canada's Oil and Natural Gas Producers.*

Chan, E. (2009). Regional ground-level ozone trends in the context of meteorological influences across Canada and the eastern United States from 1997 to 2006. *Journal of Geophysical Research, 114*(D5). doi:10.1029/2008jd010090

Chappelka, A. H., & Samuelson, L. J. (1998). Ambient ozone effects on forest trees of the eastern United States: A review [Abstract]. *New Phytologist, 139*(1), 91-108. doi:10.1046/j.1469-8137.1998.00166.x

Charpentier, A. D., Bergerson, J. A., & Maclean, H. L. (2009). Understanding the Canadian oil sands industry's greenhouse gas emissions. *Environmental Research Letters, 4*(1), 014005. doi: 10.1088/1748-9326/4/1/014005

Chen, X., Quéléver, L. L., Fung, P. L., Kesti, J., Rissanen, M. P., Bäck, J., . . . Kulmala, M. (2018). Observations of ozone depletion events in a Finnish boreal forest. *Atmospheric Chemistry and Physics, 18*(1), 49-63. doi:10.5194/acp-18-49-2018

Cho, S., Vijayaraghavan, K., Spink, D., Cosic, B., Davies, M., & Jung, J. (2017). Assessing the effects of oil sands related ozone precursor emissions on ambient ozone levels in the Alberta oil sands region, Canada. *Atmospheric Environment, 168*, 62-74. doi:10.1016/j.atmosenv.2017.08.062

De Visscher, A. (2014). *Air dispersion modeling: foundations and applications*. Somerset, New Jersey: Wiley. P21

Ducker, J. A., Holmes, C. D., Keenan, T. F., Fares, S., Goldstein, A. H., Mammarella, I., . . . Schnell, J. (2018). Synthetic ozone deposition and stomatal uptake at flux tower sites. *Biogeosciences Discussions,* 1-35. doi:10.5194/bg-2018-172

Environment and Climate Canada [ECCC]. (2018). Ozonesonde User's Manual and

Environment and Climate Change Canada [ECCC]. (2020, February 20). Air Quality Model Forecast. Retrieved March 1, 2020, from https://weather.gc.ca/aqfm/index_e.html

Fathi, S. (2017). *Evaluating the Top-down Emission Rate Retrieval Algorithm (TERRA) using Virtual Aircraft-based Sampling within the GEM-MACH Model* (Master's thesis). Toronto: York University.

Fishman, J., & Crutzen, P. J. (1978). The origin of ozone in the troposphere. *Nature, 274*(5674), 855–858. doi: 10.1038/274855a0

Finco, A., Coyle, M., Nemitz, E., Marzuoli, R., Chiesa, M., Loubet, B., . . . Gerosa, G. (2018). Characterization of ozone deposition to a mixed oak–hornbeam forest – flux measurements at five levels above and inside the canopy and their interactions with nitric oxide. *Atmospheric Chemistry and Physics, 18*(24), 17945-17961. doi:10.5194/acp-18-17945-2018

Finkelstein, P. L., Ellestad, T. G., Clarke, J. F., Meyers, T. P., Schwede, D. B., Hebert, E. O., & Neal, J. A. (2000). Ozone and sulfur dioxide dry deposition to forests: Observations and model evaluation. *Journal of Geophysical Research: Atmospheres, 105*(D12), 15365-15377. doi:10.1029/2000jd900185

Finlayson-Pitts, B., & Pitts, J. (1993). Atmospheric Chemistry of Tropospheric Ozone Formation: Scientific and Regulatory Implications. *Air & Waste*, *43*(8), 1091–1100. doi: 10.1080/1073161x.1993.10467187

Gordon, M. (2013). *Biogenic Emissions, Initial Model Setup and Test Case*. Environment Canada.

Gordon, M. (2013). *Biogenic Emissions, Modeling of the Boreal Forest in Northern Alberta*. Environment Canada.

Gordon, M., Vlasenko, A., Staebler, R. M., Stroud, C., Makar, P. A., Liggio, J., . . . Brown, S. (2014). Uptake and emission of VOCs near ground level below a mixed forest at Borden, Ontario. *Atmospheric Chemistry and Physics, 14*(17), 9087-9097. doi:10.5194/acp-14-9087-2014

Henderson, B. H., Jeffries, H. E., Kim, B., & Vizuete, W. G. (2010). The Influence of Model Resolution on Ozone in Industrial Volatile Organic Compound Plumes. *Journal of the Air & Waste Management Association, 60*(9), 1105-1117. doi:10.3155/1047-3289.60.9.1105

Holloway, A. M., & Wayne, R. P. (2010). *Atmospheric chemistry*. Cambridge, Oxford: RSC Publ.

Jiang, K. (2019). *Mixing and Deposition in a Jack Pine Forest Canopy* (master's thesis). York University, Toronto, Canada.

Kaplan, W. A., Wofsy, S. C., Keller, M., & Costa, J. M. (1988). Emission of NO and deposition of O3 in a tropical forest system. *Journal of Geophysical Research, 93*(D2), 1389. doi:10.1029/jd093id02p01389

Katz, M. (1949). Sulfur Dioxide in Atmosphere and Its Relation to Plant Life. *Industrial & Engineering Chemistry*, *41*(11), 2450–2465. doi: 10.1021/ie50479a025

Kavassalis, S. C., & Murphy, J. G. (2017). Understanding ozone-meteorology correlations: A role for dry deposition. *Geophysical Research Letters*, *44*(6), 2922–2931. doi: 10.1002/2016gl071791

Kim, S., Jeong, D., Sanchez, D., Wang, M., Seco, R., Blake, D., … Park, R. (2018). The Controlling Factors of Photochemical Ozone Production in Seoul, South Korea.

Aerosol and Air Quality Research, *18*(9), 2253–2261. doi: 10.4209/aaqr.2017.11.0452

Knabe, W. (1976). Effects of Sulfur Dioxide on Terrestrial Vegetation. *Ambio, 5*(5/6), 213-218. Retrieved March 29, 2020, from www.jstor.org/stable/4312219

Lamaud, E., Carrara, A., Brunet, Y., Lopez, A., & Druilhet, A. (2002). Ozone fluxes above and within a pine forest canopy in dry and wet conditions. *Atmospheric Environment, 36*(1), 77-88. doi:10.1016/s1352-2310(01)00468-x

Li, S., Leithead, A., Moussa, S. G., Liggio, J., Moran, M. D., Wang, D., . . . Wentzell, J. J. (2017). Differences between measured and reported volatile organic compound emissions from oil sands facilities in Alberta, Canada. *Proceedings of the National Academy of Sciences, 114*(19). doi:10.1073/pnas.1617862114

Logan, J. A. (1985). Tropospheric ozone: Seasonal behavior, trends, and anthropogenic influence. *Journal of Geophysical Research: Atmospheres*, *90*(D6), 10463–10482. doi: 10.1029/jd090id06p10463

Mckenzie, R. (2003). Ozone profile differences between Europe and New Zealand: Effects on surface UV irradiance and its estimation from satellite sensors. *Journal of Geophysical Research, 108*(D6). doi:10.1029/2002jd002770

Makar, P. A., Fuentes, J. D., Wang, D., Staebler, R. M., & Wiebe, H. A. (1999). Chemical processing of biogenic hydrocarbons within and above a temperate deciduous forest. *Atmospheric Chemistry*, *104*(D3), 3581–3603. doi: 10.1029/1998JD100065

Makar, P. A., Staebler, R. M., Akingunola, A., Zhang, J., Mclinden, C., Kharol, S. K., . . . Zheng, Q. (2016). The effects of forest canopy shading and turbulence on boundary layer ozone. *Nature Communications, 8*(1). doi:10.1038/ncomms15243

Manning, W. J., & Tiedemann, A. V. (1995). Climate change: Potential effects of increased atmospheric Carbon dioxide (CO2), ozone (O3), and ultraviolet-B (UV-B) radiation

on plant diseases. *Environmental Pollution*, *88*(2), 219–245. doi: 10.1016/0269-7491(95)91446-r

Moroni, B., Becagli, S., Bolzacchini, E., Busetto, M., Cappelletti, D., Crocchianti, S., . . . Vitale, V. (2015). Vertical Profiles and Chemical Properties of Aerosol Particles upon Ny-Ålesund (Svalbard Islands). *Advances in Meteorology, 2015*, 1-11. doi:10.1155/2015/292081

Morris, G. A., Komhyr, W. D., Hirokawa, J., Flynn, J., Lefer, B., Krotkov, N., & Ngan, F. (2010). A Balloon Sounding Technique for Measuring SO2 Plumes. *Journal of Atmospheric and Oceanic Technology*, *27*, 1318–1330. doi: 10.1175/2010JTECHA1436.1

Natural Resource Canada. (2016, February 19). Oil Sands Extraction and Processing. Retrieved February 03, 2020, from https://www.nrcan.gc.ca/energy/energy-sources-distribution/crude-oil/oil-sands-extraction-and-processing/18094

National Research Council. (1991). VOCs and Nox: Relationship to Ozone and Associated Pollutants. In *Rethinking the Ozone Problem in Urban and Regional Air Pollution* (pp. 163–186). Washington, DC: The National Academies Press.

NCAR. (n.d.). QUICK TUV CALCULATOR. Retrieved March 24, 2020, from http://cprm.acom.ucar.edu/Models/TUV/Interactive_TUV/

Newell, R. E. (1963). Transfer through the tropopause and within the stratosphere. *Quarterly Journal of the Royal Meteorological Society*, *89*(380), 167–204. doi: 10.1002/qj.49708938002

Olltmans, S. J., Lefohn, A. S., Harris, J. M., Galbally, I., Scheel, H. E., Bodeker, G., … Cuevas, E. (2006). Long-term changes in tropospheric ozone. *Long-Term Changes in Tropospheric Ozone*, *14*(17), 3156–3173. doi: 10.1016/j.atmosenv.2006.01.029

Pancholi, P., Kumar, A., Bikundia, D. S., & Chourasiya, S. (2018). An observation of seasonal and diurnal behavior of O_3 –NO_x relationships and local/regional oxidant (O_X = O_3 + NO_2) levels at a semi-arid urban site of western India. *Sustainable Environment Research*, *28*(2), 79–89. doi: 10.1016/j.serj.2017.11.001

Raupach, M. R. (1989). A practical Lagrangian method for relating scalar concentrations to source distributions in vegetation canopies. *Royal Meteorological Society*, *115*(487), 609–632. doi: 10.1002/qj.49711548710

Robert, S., Keresztesl, R., Tonk,Z., Korodil, A., & Craciun, M.E. (2017) The Examination of the Effects of Relative Humidity on the of Tropospheric Ozone Concentrations in the Ciuc Basin, Romania, *REV.CHIM,* 68(4).

Roberts, T. (2018). Ozone Depletion in Tropospheric Volcanic Plumes: From Halogen-Poor to Halogen-Rich Emissions. *Geosciences, 8*(2), 68. doi:10.3390/geosciences8020068

Seinfeld, J.H. and Pandis, S.N. (2006) *Atmospheric Chemistry and Physics: From Air Pollution to Climate Change.* 2nd Edition, John Wiley & Sons, New York.

Stathopoulou, E., Mihalakakou, G., Santamouris, M., & Bagiorgas, H. S. (2008). On the impact of temperature on tropospheric ozone concentration levels in urban environments. *Journal of Earth System Science, 117*(3), 227-236. doi:10.1007/s12040-008-0027-9

Stringham, G., (2011) Energy Developments in Canada's Oil Sands. *Alberta Oil Sands* PP.19-34

Stroud, C. (2005). Role of canopy-scale photochemistry in modifying biogenic-atmosphere exchange of reactive terpene species: Results from the CELTIC field study. *Journal of Geophysical Research*, *110*(D17). doi: 10.1029/2005jd005775

Thermo Fisher Scientific Inc (2011) Model 49i Instruction Manual

Wilson, W. E., Levy, A., & Wimmer, D. (1972). A Study of Sulfur Dioxide in Photochemical Smog. *Journal of the Air Pollution Control Association*, *22*(1), 27-32. doi:10.1080/00022470.1972.10469605

Wood Buffalo Environmental Association [WBEA]. (2020). Fort Mckay South: Monitoring Stations. Retrieved March 3, 2020, from https://wbea.org/stations/fort-mckay-south/

Wood Buffalo Environmental Association [WBEA]. (2020). Buffalo Viewpoint: Monitoring stations. Retrieved March 3, 2020, from https://wbea.org/stations/buffalo-viewpoint/

Wood Buffalo Environmental Association [WBEA]. (2019). JP104: Monitoring Stations. Retrieved from https://wbea.org/towers/jp104/.

Xu, X., Lin, W., Xu, W., Jin, J., Wang, Y., Zhang, G., . . . Zhao, H. (2020). Long-term changes of regional ozone in China: Implications for human health and ecosystem impacts. *Elem Sci Anth, 8*(1), 13. doi:10.1525/elementa.409

Appendix A

Pasquill-Gifford stability classes (De Visscher, 2014)

Surface wind speed (m/s)	In coming solar radiation (daytime)			Cloud fraction (nighttime)	
	strong	moderate	low	>50%	<50%
<2	A	A-B	B	E	F
2-3	A-B	B	C	E	F
3-5	B	B-C	C	D	E
5-6	C	C-D	D	D	D
>6	C	D	D	D	D

Briggs' equation (x represents the distance from the plume to the site, Briggs, 1973)

Stability class	σ_y (m)
A (very unstable)	$0.22x(1+0.0001x)^{-\frac{1}{2}}$
B (unstable)	$0.16x(1+0.0001x)^{-\frac{1}{2}}$
C (slightly unstable)	$0.11x(1+0.0001x)^{-\frac{1}{2}}$
D (neutral)	$0.08x(1+0.0001x)^{-\frac{1}{2}}$
E (slightly stable)	$0.06x(1+0.0001x)^{-\frac{1}{2}}$
F (stable)	$0.04x(1+0.0001x)^{-\frac{1}{2}}$

Appendix B

The flow rated of two ozonesondes on each measurement day, one with filter tube and without filter tube

	June 13 2018		June 15 2018		June 15 2018	
	without filter	with filter	without filter	with filter	without filter	with filter
1	212.5	218.6	215.1	218.3	213.4	223
2	212.4	216.4	215.3	219.7	219.7	220.5
3	211.7	217.9	214.4	220.7	215.9	221.9
4	212.6	216.4	215.3	219.7	214.6	220.4
5	212.4	218.2	215.5	219.7	215.4	221.3
6	212.5	215.2	215.3	218.5	216.1	220.6
7	212.2	218.8	214.6	218.9	214.7	220.9
8	210.9	217.4	214.6	217.9	215.1	220.2
9	211.1	219.1	215	218.3	215.1	219.2
10	210.7	219.8	215.1	217	214.9	222.8
Average	211.9	217.8	215.0	218.9	215.5	221.1
standard deviation	0.7	1.4	0.3	1.0	1.6	1.1